POLITECNICO
MILANO 1863

School of Industrial and Information Engineering
Department of Aerospace Science and Technology

Guidance & Navigation algorithm for an inspection mission about a known and uncooperative object

CANDIDATES

Andrea Laddomada
976363

Isha Lad
965615

SUPERVISOR

Pierluigi Di Lizia

CO-SUPERVISOR
Michele Maestrini

Master of Science in Space Engineering

A.Y. 2021-2022

To infinity and beyond
- Buzz Lightyear

Abstract

The design of an autonomous inspection mission performed by a deputy around a target object is motivated by the necessity to earn some advantages, making easy and feasible the motion of satellites, removing any human control from ground, both for LEO and for deep space operations. In this thesis, two different mission scenarios are covered: the first is characterized by an unperturbed environment, with the absence of any perturbation, while in the second the gravitational perturbation (J_2) is included. These different environments are simulated by the Nonlinear Equations of Relative Motion, working on a LVLH reference frame, while the Hill-Clohessy-Wiltshire equations are adopted by the on-board computer of the deputy. Adopting the natural dynamics for the inspection, fuel costs are minimized and it still presents excellent opportunities to inspect and acquire images of the surface of the target object. The navigation is modeled by using a camera, that provides measurements to the Unscented Kalman Filter (UKF), fundamental tool that offers an estimation of the actual position of the deputy with a certain precision. The merging of these aspects generates a preliminary definition of ConOps, baseline mission concept that is shown in different variants through the gradual development of the algorithm. This updating allows to improve the general results, according to the imposed score. In addition, a further improvement has been obtained trying to make a step forward, with a preliminary overview on the inclined relative orbits. Finally, the time performances of the algorithm are tested on a Raspberry Pi 4 platform to demonstrate the actual functioning on a real satellite.

Sommario

Il design di una missione di ispezione di un satellite inseguitore attorno ad un satellite bersaglio è motivato dalla necessità di guadagnare alcuni vantaggi, rendendo più semplice e possibile il moto dei satelliti, rimuovendo qualsiasi controllo umano da terra, sia per le operazioni in orbita terrestre bassa, sia per quelle nello spazio profondo. In questa tesi vengono mostrati due scenari di missione: il primo caratterizzato da un ambiente non perturbato, mentre nel secondo è inclusa la perturbazione gravitazionale (J_2). Questi diversi ambienti sono simulati tramite le equazioni non lineari del moto relativo, usando il sistema di riferimento LVLH, mentre le equazioni di Hill-Clohessy-Wiltshire vengono adottate per il computer a bordo del satellite inseguitore. Adottando dinamiche naturali per l'ispezione, i costi di propellente sono minimizzati e sono ancora presenti opportunità per ispezionare e acquisire immagini della superficie dell'oggetto bersaglio in modo eccellente. La navigazione è modellata utilizzando una camera, che fornisce misurazioni al filtro (UKF), strumento fondamentale che offre una stima della posizione attuale del satellite inseguitore con una certa precisione. L'unione di questi aspetti genera una definizione preliminare di ConOps, pianificazione delle operazioni della missione che è mostrata in differenti varianti attraverso il graduale sviluppo dell'algoritmo. Questo aggiornamento permette di migliorare i risultati generali, in base ai parametri d'analisi imposti. In aggiunta, un ulteriore miglioramento è stato ottenuto cercando di compiere un passo in avanti, con l'introduzione generale alle orbite relative inclinate. Infine, i tempi computazionali dell'algoritmo sono stati testati su una piattaforma Raspberry Pi 4 per dimostrare il funzionamento su un satellite reale.

Acknowledgements

Perhaps the most difficult task in writing a thesis is not the hours of research and study, but finding the best way to fill this page, in order to give the right importance at all the people with who I shared the last years. This treatment is not the result only of a simple research, but also of the experiences and the meetings with new or still known people. To all those, I hope you know your help has been greatly appreciated.

First of all, I would like to tenkalu my colleague Isha ("Issues", for friends) for investing lasts months in working on this thesis, for having a lot of patience to try to understand me during my explanations, and provide me valid reasons to sustain these two years of fights between projects and exams, pushing me to give the maximum. Honestly, if I reached this accomplishment, part of it is thanks to you, not only from a professional point of view, but also as an important friend. I would also like to extend deep gratitude to my supervisor Pierluigi Di Lizia and to my co-advisor Michele Maestrini for guiding me through this thesis, stimulating curiosity and interest in the topics treated.

I have to thank my mum, my dad, my brothers Alex and Pietro and the other part of the family, both near and far. I felt your constant presence, albeit away from my hometown, and your support during these five years.

I would also like to thank my Poli friends, from the first known in the Calculus lecture to those met along the way. Dear Sam, Tommy, Gu, Giusy, Ivana, Shang, Jo, GG and Lova, you have been good colleagues, but above all you have been and still are good partners of many adventures, lived in Milan and on Teams. Together with you, I take this opportunity to thank the various colleagues met in the hallways of BL27 and B12 buildings for gladdening my days at PoliMi, and roommates for the many laughs during dinners.

Among the people who should be credited for helping me get to where I am now, I shall also mention all my friends of Trentino. When either I see an airplane either drink some potable water either I imply a little accent, I ever give you a thought (or a photo, right Giordy and Stizz?).

I would like to thank my old classmates of Liceo: Vale and Erika, the inseparable Ambrogi. Years go by, but the stories of lower Garda lake do not!

I owe a huge thank to the scottish philosopher, Cava, for being my best friend and helping me in the hard times, both with music, with latin and anything else, hoping to return the favor one day.

I cannot forget to thank you too, Elena, for always believing in me, for motivating me also when the batteries were empty and for being able to show me that there is always a solution, looking beyond rational limits.

A final mention goes to two people: Raffaella and Daniel. I hope you consider my achievement as yours.

Andrea Laddomada

Acknowledgements

First of all, I would like to thank my colleague Andrea, who has been not only a colleague, but also one of my best friends, my snack buddy (I will never thank you enough for all the coffee and snacks that you offered me) and a big brother, in the darkest moments. Thank you for always believing in me and in all the makings, and for always encouraged me to give my best, fighting against my stubbornness and mostly my laziness. Starting this journey with you has been a gamble, after your continuous jokes about doing the thesis together, but I could not ask for better. After all the laughs, the tears, and the quarrels, I can finally say that it was worth it because look at what we have done: we succeed! I still not believe it, but I can say that I would do it all over again to live again all the good times we had. Thanks again for making special this last period of study (and thanks to stand me for this 9 months).

Secondly, I would like to thank my supervisor, Pierluigi Di Lizia, for the infinite availability and the constant interest in the treated work, and my co-advisor, Michele Maestrini, for all the help and the time spent (especially thanks for finding that stupid wrong counter in the code).

Thirdly, I would like to thank my parents, who have always supported me and pushed me to follow my dreams, making all of this possible. Thanks for all the support and the encouragement in the most stressful moments. Obviously, I also thank my brother who has always been closed to me: thanks for lighting the way, showing me that "engineering is not that hard in the end". Moreover, I would like to thank my extended family, Giulia, Niccolò, Marina, Alessandro, and Ines, who although they have only known me for a short time, they believed in me right away.

Finally, I would like to thank my awesome friends that have been a part of this path. Jo, thank you for making the return to university after the lockdown much lighter with your pranks (sometimes extreme), your delicious sweets and your kindness (and thanks for always holding me a seat in BL.27). GG and Lova, although the little time spent together, thanks for being my fellow students and thanks for making me your "brosha", I cannot wait to see you graduate, do not give up. Giusy, Iman, and Ivana thank to be my "female" friends in a world of "men", meeting you has been a relief and has made all lighter and funny. Sam, thanks for being always very good for a laugh and for making me feel smart asking for clarifications on the lectures. Shang, thanks for sharing with me your anxiety for the deadlines of the thesis. In the end, Luca, thanks for teaching me so much and for remembering me every time I ask you something: "ma calcolo non ti ha insegnato nulla?".

A special mention goes to Marty, who has always been by my side since middle school, for the infinite bike rides, for the passion for the cinema and unfortunately for skype during the lockdown but mostly thanks for sharing with me the anxiety for the exams and the deadlines.

Isha Lad

Nomenclature

α_h	Orbital acceleration of target satellite
α_r	Steering acceleration of target satellite
$\hat{\boldsymbol{X}}$	First axis of ECI reference frame
$\hat{\boldsymbol{x}}$	First axis of LVLH reference frame
$\hat{\boldsymbol{Y}}$	Second axis of ECI reference frame
$\hat{\boldsymbol{y}}$	Second axis of LVLH reference frame
$\hat{\boldsymbol{Z}}$	Third axis of ECI reference frame
$\hat{\boldsymbol{z}}$	Third axis of LVLH reference frame
$\boldsymbol{\rho_d}$	target-Deputy distance vector
$\boldsymbol{h_t}$	target angular momentum vector
$\boldsymbol{r_t}$	target position vector
$\boldsymbol{v_t}$	target velocity vector
Γ	Rotation matrix
μ	Earth's gravitational constant
ω_j	Angular velocity related to one axis
ρ_i^{ENV}	marker measurement in target body reference frame
θ	True anomaly
ECI	Earth Centered Inertial
GNC	Guidance, Navigation and Control
GUT	General Unscented Transform
h_t	target angular momentum magnitude
HCW	Hill Clohessy Wiltshire
i	Inclination
J_2	second zonal harmonic coefficient of the Earth
k_{J2}	Constant term related to J2 perturbation
LEO	Low Earth Orbit
$LVLH$	Local Vertical Local Horizon
MRP	Modified Rodrigues Parameters
$NERM$	Nonlinear Eqs. Relative Motion
NP	Unperturbed case
OOS	On-Orbit Servicing
P	Perturbed case
R_e	Earth's equatorial radius
r_t	target position magnitude
RSO	Resident Space Object
SBC	Single Board Computer
ToF	Time of Flight
ToF_M	Time of Flight of manoeuvre
UKF	Unscented Kalman Filter
UT	Unscented Transformation
v_t	target velocity magnitude
z_i	marker measurement in LVLH reference frame

Contents

List of Figures

List of Tables

Chapter 1

Introduction

The concept of inspection missions immediately captured the interest of scientists starting from the launch of the Sputnik in the 1950s. Nearly 60 years after, there are still a clear scenario of increasing demand of inspections satellites for different reasons, from military, to commercial and to governmental projects. Furthermore, in the last few years, satellite inspection missions have become more and more important for a safe space environment due to the huge amount of launched space objects. The space around the Earth has gradually become overpopulated by Resident Space Objects (RSO): there are approximately 23000 pieces of debris larger than a softball orbiting the Earth which travel at speeds up to 28000 km/h, fast enough for a relatively small piece of orbital debris to damage a satellite or even the ISS. Moreover, there are half a million pieces of debris the size of a marble or larger, approximately 100 million pieces of debris about 10 cm (or 1 mm) or larger and even more smaller micrometer-sized debris, which can cause serious damages to small satellites or CubeSats. The threat of space debris can no longer be neglected: the huge amount of collisions occurring every year is increasing more and more the number of debris and the probability of future collisions increases consequently[1].

To study these debris and other space objects, which includes both cooperative and uncooperative satellites, inspection missions are essential. In particular, for this specific kind of mission, standard operating methods, which involves humans, are not convenient anymore. Usually, the data transmitted from the space segment are elaborated on ground, and relevant commands are transmitted back on orbit to be executed. The problem with this kind of approach lies in the fact that relative orbits for inspection missions have to be continuously modified based on whether they are still effective or not. In fact, the deputy spacecraft, along its orbit, will be able to observe only certain regions of the target, therefore it will be required to change its relative motion in order to reach the full coverage and gain more data about the RSO. It is clear how this increases a lot the effort of the mission analysts and, therefore, how it constitutes a major limit for the state-of-the-art in inspection missions design. Moreover, the presence of humans in the loop may lead to the selection of suboptimal orbits and it is prone to possible errors. A possible solution comes from the opportunity to introduce a certain degree of autonomy [22] shifting towards autonomous approaches to reduce operational costs, human errors, communication delays or lack of coverage.

---

[1] `https://www.nasa.gov/mission_pages/station/news/orbital_debris.html`

1.1 Historical overview

The first experiments for autonomous mission started in 1997 with NASDA's ETS-VII mission[2], an unmanned satellite able to perform independently docking manoeuvres. The overall objective was to acquire/retrieve materials to/from a satellite in orbit. In particular, three experiments were carried out:

1. demonstration of rendezvous-docking equipment in orbit;
2. evaluation of both automatic and remotely piloted rendezvous-docking in orbit;
3. demonstration of simultaneous operation of two spacecraft.

Through these experiments, the autonomous rendezvous docking technologies from the relative approach to the docking (from 10 km to docking) were verified on orbit.

Then, the Air Force Research Laboratory developed some small satellites (i.e. XSS-10, XSS-11 [3]) which demonstrated the possibility to perform autonomous proximity operations and inspection of a satellite. The specific mission was to demonstrate "the proximity operations with a resident space object (RSO), employing a semi-autonomous, maneuverable space vehicle communicating with command and control sites via a space/ground link".
Later, in 2010, the Swedish Space Corporation's mission PRISMA[4] tried to perform approach, rendezvous and formation flight with a known object (Tango), using autonomous GNC algorithms. The main goals of PRISMA are to perform GNC demonstrations and sensor technology experiments for a family of future missions where rendezvous and formation flying are a necessary prerequisite. In particular, the GNC demonstrations are:

1. autonomous formation flying;
2. homing and rendezvous;
3. proximity operations or rendezvous tests, including final approach and recede operations.

More recently, in September 2019, NASA's Seeker-1 CubeSat performed a single spacecraft remote inspection of the Cygnus spacecraft[5], demonstrating ultra-low cost in-space inspection capability. The navigation architecture consists of three parts: the IMU Preprocessor (IMUPre), the fast propagator (FASTNAV), and the Kalman Filter (NAV). Moreover, the guidance algorithm is integrated with the control algorithm to achieve waypoint seeking, position and attitude holds, target tracking, and to limit relative kinetic energy. Since Seeker will operate in close proximity (approximately 30 m from Cygnus), relative orbital dynamics are assumed to be negligible, which simplified the guidance algorithm.

---

[2] `https://www.eoportal.org/satellite-missions/ets-vii`

[3] `https://www.eoportal.org/satellite-missions/xss`

[4] `https://www.eoportal.org/satellite-missions/prisma-prototype`

[5] `https://www.eoportal.org/other-space-activities/cygnus-ng-11`

1.2 Thesis outline and contributions

In this thesis, a similar inspection mission to Seeker-1 described before, will be developed starting from that baseline.
The navigation system will be still composed of a processor, a propagator and a Kalman filter. In particular, the algorithm will be tested on a Raspberry Pi 4 to guarantee the feasibility of its usage also on a small microprocessor which can be mounted on satellite of different dimension, from CubeSats to big satellite, leading to a robust and versatile GNC system. On the other hand, the guidance algorithm will be reduced to the solution of a simple minimization problem with suitable imposed constraints in which only the relative dynamics between target and deputy will be taken into account. This will lead to a lighter algorithm in terms of computational cost. All these choices comes from the need to simplify the algorithm as much as possible, in order to keep a low-cost mission.

Moreover, the key point of the proposed GNC system is the relation between the navigation and guidance systems. In fact, the guidance system will receive data concerning the state of the satellite directly from the navigation system, which will introduce some errors with respect to the real state due to the fact that the predictor model adopts a linear dynamics. This will lead to a completely autonomous satellite, able to take decision on how and where to go, without any remote control from ground.

Finally, another difference with respect from the Seeker's mission will be the choice of the target: in particular, Envisat has been chosen, as a known target but non-cooperative, in order to foreseen a possible application of this algorithm for inspection of known debris.

Chapter 2

Guidance

This first chapter will present the guidance system, which has the aim to offer the best trajectory for the satellite, according to the initial and imposed conditions. One of the main goals of this thesis is to optimize the inspection of the target and this will require the knowledge of various parameters coming from the choice of the rotational and translational dynamics. In particular, in the next paragraph, an excursus on the planning of the manoeuvres will be presented and then, the adopted dynamics will be shown, highlighting their uses and their differences.

2.1 Literature Review

The development of an optimized algorithm for the guidance system has already debated starting from the first missions of proximity operations around a RSO. The variety of these methodologies is due to the different objectives and opportunities. Shortly, some of the used techniques are:

- Glideslope Guidance [18],[14], that represents the baseline of guidance algorithms, adopted in the past also for rendezvous and proximity operations of the space shuttle with other vehicles with the help of astronauts. The sequence of manoeuvres and its cost depend on the mission phase. Using a proportional law is common in this methodology;

- Artificial Potential Functions [25], where the trajectory is generated by application of a gradient of potential functions, divided into *attractive potentials*, used for goal regions, and *repulsive potentials*, used for obstacle region. A gradient ascent/descent routine is often called to trace a feasible path from any initial state;

- Motion Planning Algorithm, that has the aim to create decision sequences to achieve goals mission, building the optimal solution step by step. Many variants exist, as Fast Marching Tree [17], Rapidly-exploring Random Tree [6], Sampling-Based Model Predictive Optimization [10],[7];

- Model Predictive Control [20], that, starting from initial state, predict future states continuing to solve an Optimal Control Problem, that minimize a cost function. After the computation of the first control segment, the cycle continues until convergence to the goal;

- Artificial Neural Networks & Artificial Intelligence [5], that is the key of the future, where the machine learns abilities and adapts itself to different scenarios in an autonomous way;

The application of such methodologies for inspection missions is grown up to the point that the satellite itself can control autonomously, removing the dependency from ground

controls and opening the possibility to operate missions also at long distances, not easily accessible for ground controls.
To use such methods, dynamics and reference systems must be chosen, according also to the objective and the accuracy of the mission. In fact, the dynamical models can be categorized into 2 main groups, based on the kind of representation [16]:

- using an *Orbital Element State*, considering the set of orbital elements of target and deputy, respectively. An example is the Relative Orbital Elements (ROE);
- using a *Translational State*, adopting an auxiliary Cartesian Reference Frame fixed in the target center of gravity;

All of them can be represented in linear terms or not, according to the selection of eventual dissipative phenomena, like perturbations [12],[2].
In this treatment, the focus is on a LEO mission, starting from an unperturbed case where the dynamics is free from perturbations and going towards a more complicated and "real" model, where the gravitational field will be considered.

2.2 Dynamical Models

The formulation of the kinematics and the dynamics of the two satellites (target and deputy) is the first knot to untie. This enables to visualize the simulation environment, where it will be possible to highlight similarities and differences between the real motion, from which the measurements are taken, and the on-board dynamics of the deputy. In fact, the last one will be represented by a linearized dynamics, built by a set of equations called Hill-Clohessy-Wiltshire (HCW), while the real simulation will be performed by another dynamics, the so called Nonlinear Equations of Relative Motion (NERM). Moreover, natural perturbations present in the space region around the Earth will be considered to get a more accurate simulator environment. In particular, Low Earth Orbits are characterized by two kind of perturbations: atmospheric drag (that is the most relevant term when the body is under 600 km of altitude) and oblateness of the Earth. If the first one could be neglected due to the given altitude of our desired orbit, the last one should be considered in the simulation environment, also to understand how the pertubation can change the motion of the deputy in terms of relative position, velocity and cost of manoeuvre.

2.2.1 Simulation Environment

Considering a simple system composed by two satellites, each of them on a LEO, the easiest way to study them is to express the motion of one relative to the other. This approach has two advantages:

- in an inspection mission, the parameters are expressed explicitly, as the distance between the two satellites;
- this approach is more intuitive with respect to the respectively motions around the Earth.

To proceed in this direction it is necessary to introduce a first reference frame centered in the Earth (ECI), spanned by the unit vectors ($\hat{X}$,$\hat{Y}$,$\hat{Z}$), and then convert into the new reference frame (LVLH or Hill rotating frame), spanned by its unit vectors ($\hat{o}_r$,$\hat{o}_\theta$,$\hat{o}_h$).

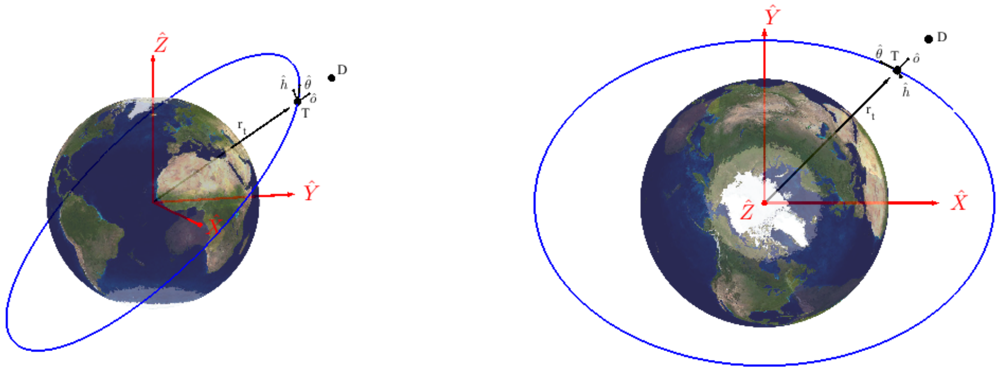

(a) Orbital model (b) X-Y plane of Orbital Model

Figure 2.1: Comparison of the reference frames

Orbital Motion

The first motion is described by the standard Keplerian Two Body Problem:

$$\ddot{\boldsymbol{r}} = -\frac{\mu}{r^3}\boldsymbol{r} + \boldsymbol{a}_p \tag{2.1}$$

where μ is the gravitational parameter of the Earth, $\mathbf{r}$ the spacecraft's position vector in ECI frame, r the norm of the orbital radius of the spacecraft, a_p the term due to perturbations and $\ddot{r}$ the spacecraft acceleration vector in ECI frame.
From this assumption and neglecting the perturbation term [13], the first set of equations of motion for the target (2.2) and the deputy (2.3) are obtained

$$\ddot{\boldsymbol{r}}_t = -\frac{\mu}{r_t^3}\boldsymbol{r_t} \tag{2.2}$$

$$\ddot{\boldsymbol{r}}_d = -\frac{\mu}{r_d^3}\boldsymbol{r_d} \tag{2.3}$$

Coming back to Eqs. (2.2) and (2.3), in order to derive the relative equations of motion using the Cartesian coordinates in LVLH frame, the deputy position vector can be written as the sum of the target position vector and the distance between target and deputy in the rotating Hill frame:

$$\begin{aligned}\boldsymbol{r}_d &= \boldsymbol{r}_t + \boldsymbol{\rho} \\ &= (r_t + x)\hat{o}_r + y\hat{o}_\theta + z\hat{o}_h\end{aligned} \tag{2.4}$$

Substituting Eq. (2.4) in Eq. (2.3), it can be obtained a new relation, based on the LVLH coordinates (where O is the LVLH symbol):

$$\ddot{\boldsymbol{r}}_d = -\frac{\mu}{r_d^3}\begin{bmatrix} r_t + x \\ y \\ z \end{bmatrix}_O \tag{2.5}$$

where

$$r_d = \sqrt{(r_t + x)^2 + y^2 + z^2} \tag{2.6}$$

and the angular velocity vector of the rotating Hill frame with respect to the inertial frame [N] is:

$$\boldsymbol{\omega}_{O/N} = \dot{\boldsymbol{f}}\hat{o}_h \tag{2.7}$$

where the vector triad, necessary to describe the Hill frame attached to the deputy, is defined as:

$$\hat{o}_r = \frac{\boldsymbol{r}_t}{r_t} \qquad \hat{o}_\theta = \hat{o}_h \times \hat{o}_r \qquad \hat{o}_h = \frac{\boldsymbol{h}_t}{h_t} \tag{2.8}$$

$$\boldsymbol{h}_t = \boldsymbol{r}_t \times \dot{\boldsymbol{r}}_t \qquad h_t = |\boldsymbol{h}_t| \tag{2.9}$$

where $\hat{o}_r$ is the axis in the direction of the orbit radius, $\hat{o}_h$ the axis normal to the orbit radius, $\hat{o}_\theta$ the third axis that completes the right-hand coordinates system, $\boldsymbol{h_t}$ the angular momentum vector and h_t its magnitude. Taking the derivative with respect to the inertial frame twice, the deputy satellite acceleration vector is given by:

$$\ddot{\boldsymbol{r}}_d = (\ddot{\boldsymbol{r}}_t+\ddot{\boldsymbol{x}}-2\dot{\boldsymbol{y}}\dot{\boldsymbol{f}}-\ddot{f}y-\dot{\boldsymbol{f}}^2(r_t+x))\hat{\boldsymbol{o}}_r+(\ddot{\boldsymbol{y}}+2\dot{\boldsymbol{f}}(\dot{\boldsymbol{r}}_t+\dot{\boldsymbol{x}})+\ddot{\boldsymbol{f}}(\dot{\boldsymbol{r}}_t+\dot{\boldsymbol{x}})-\dot{\boldsymbol{f}}^2y)\hat{\boldsymbol{o}}_\theta+\ddot{\boldsymbol{z}}\hat{\boldsymbol{o}}_h \tag{2.10}$$

Considering that the position of the deputy is $\boldsymbol{r}_d = r_d\hat{\boldsymbol{o}}_r$, the second time derivative will be equal to:

$$\ddot{\boldsymbol{r}}_t = (\ddot{\boldsymbol{r}}_t - r_t\dot{\boldsymbol{f}}^2)\hat{\boldsymbol{o}}_r \tag{2.11}$$

Comparing Eq. (2.11) with Eq. (2.2), the deputy's orbit radius acceleration is expressed by:

$$\ddot{\boldsymbol{r}}_t = r_t\dot{\boldsymbol{f}}^2 - \frac{\mu}{r_t^2} \tag{2.12}$$

From here, the new version of Eq. (2.10) can be retrieved, considering Eq. (2.12):

$$\ddot{\boldsymbol{r}}_d = \left(\ddot{\boldsymbol{x}} - 2\dot{\boldsymbol{f}}\dot{\boldsymbol{y}} + y\ddot{f} - \dot{\boldsymbol{f}}^2x - \frac{\mu}{r_t^2}\right)\hat{\boldsymbol{o}}_r + \left(\ddot{\boldsymbol{y}} + 2\dot{\boldsymbol{f}}\dot{\boldsymbol{x}} - x\ddot{f} - \dot{\boldsymbol{f}}^2y\right)\hat{\boldsymbol{o}}_\theta + \ddot{\boldsymbol{z}}\hat{\boldsymbol{o}}_h \tag{2.13}$$

Comparing Eqs. (2.5) and (2.13), the exact nonlinear relative equations of motion are given by:

$$\begin{cases} \ddot{\boldsymbol{x}} - 2\dot{\boldsymbol{f}}\dot{\boldsymbol{y}} + \ddot{f}y - \dot{\boldsymbol{f}}^2x - \frac{\mu}{r_t^2} = -\frac{\mu}{r_d^3}(r_t + x) \\ \ddot{\boldsymbol{y}} + 2\dot{\boldsymbol{f}}\dot{\boldsymbol{x}} - \ddot{f}x - \dot{\boldsymbol{f}}^2y = -\frac{\mu}{r_d^3}y \\ \ddot{\boldsymbol{z}} = -\frac{\mu}{r_d^3}z \end{cases} \tag{2.14}$$

Introducing Eq. (2.6) and defining the true latitude as $\theta = f+\omega$, where ω is the argument of perigee of the target's orbit, the general relative equations of motion are rewritten in the common form:

$$\begin{cases} \ddot{x} = 2\dot{\theta}\dot{y} - \ddot{\theta}y + \dot{\theta}^2x - \frac{\mu(r_t+x)}{[(r_t+x)^2+y^2+z^2]^{\frac{3}{2}}} + \frac{\mu}{r_t^2} \\ \ddot{y} = -2\dot{\theta}\dot{x} + \ddot{\theta}x + \dot{\theta}^2y - \frac{\mu y}{[(r_t+x)^2+y^2+z^2]^{\frac{3}{2}}} \\ \ddot{z} = -\frac{\mu z}{[(r_t+x)^2+y^2+z^2]^{\frac{3}{2}}} \end{cases} \tag{2.15}$$

To simplify the orbital model, some considerations have been made:

- The target moves around the Earth on a circular orbit ($e = 0$), so the distance from the latter remains constant ($p = r_c$);

- The velocity of the target along the path, remains constant, and it can be considered as the mean motion of the orbit.

$$\begin{cases} \ddot{r}_t = 0 \\ \dot{r}_t = 0 \rightarrow \ddot{\theta} = 0 \\ \dot{\theta} = n = \sqrt{\frac{\mu}{r_t^3}} \end{cases} \tag{2.16}$$

Using these assumptions, the **general relative equations of motion** become:

$$\begin{cases} \ddot{x} = 2n\dot{y} + n^2 x - \frac{\mu(r_t+x)}{[(r_t+x)^2+y^2+z^2]^{\frac{3}{2}}} + \frac{\mu}{r_t^2} \\ \ddot{y} = -2n\dot{x} + n^2 y - \frac{\mu y}{[(r_t+x)^2+y^2+z^2]^{\frac{3}{2}}} \\ \ddot{z} = -\frac{\mu z}{[(r_t+x)^2+y^2+z^2]^{\frac{3}{2}}} \end{cases} \tag{2.17}$$

On the other hand, coming back to the Eq. (2.1) and considering the perturbation term, the corresponding form of the NERM can be retrieve in another way [9], using the Lagrangian Formulation:

$$\frac{d}{dt}\left(\frac{\partial L_d}{\partial \dot{\boldsymbol{q}}_d}\right) - \frac{\partial L_d}{\partial \boldsymbol{q}_d} = 0 \tag{2.18}$$

where $\boldsymbol{q}_d = [x \ y \ z]$ are the configurations of the deputy in the LVLH coordinates and L_d is its Lagragian, that can be described as:

$$L_d(\boldsymbol{q}_t, \dot{\boldsymbol{q}}_t, \boldsymbol{q}_d, \dot{\boldsymbol{q}}_d) = K_d(\boldsymbol{q}_t, \dot{\boldsymbol{q}}_t, \boldsymbol{q}_d, \dot{\boldsymbol{q}}_d) - U_d(\boldsymbol{q}_t, \dot{\boldsymbol{q}}_t) \tag{2.19}$$

where $\boldsymbol{q}_t$ is the configuration vector of the target in the ECI frame, K_d the kinetic energy of the deputy and U_d the potential energy of the deputy. Substituting Eq. (2.19) into Eq. (2.18) yields to:

$$\frac{d}{dt}\left(\frac{\partial K_d}{\partial \dot{\boldsymbol{q}}_d}\right) - \frac{\partial K_d}{\partial \boldsymbol{q}_d} + \frac{\partial U_d}{\partial \boldsymbol{q}_d} = 0 \tag{2.20}$$

Now, computing K_d and U_d, the exact nonlinear J2 relative dynamics can be obtained. Starting from Eq. (2.4) and its first time derivative, that can be computed considering a new form of identity in Eq. (2.7), expressed as:

$$\boldsymbol{\omega}_{O/N} = \omega_r \hat{\boldsymbol{o}}_r + \omega_h \hat{\boldsymbol{o}}_h \tag{2.21}$$

whose component around the θ axis is zero [19], that is, $\omega_\theta = 0$, and ω_r can be referred as steering rate of the orbital plane, while ω_h as the orbital rate, and they are computed by considering also Keplerian Elements (where i is the target's orbit inclination, $\theta = f$):

$$\omega_r = -k_{J2} sin(2i) sin(\theta)/hr^3 \tag{2.22}$$

$$\omega_h = h/r_t^2 \tag{2.23}$$

From these considerations, the velocities of the unit vectors of the LVLH frame are expressed as:

$$\dot{\hat{\boldsymbol{o}}}_r = \boldsymbol{\omega}_{O/N} \times \hat{\boldsymbol{o}}_r = \omega_h \hat{\boldsymbol{o}}_r \qquad \dot{\hat{\boldsymbol{o}}}_\theta = \boldsymbol{\omega}_{O/N} \times \hat{\boldsymbol{o}}_\theta = \omega_r \hat{\boldsymbol{o}}_h - \omega_h \hat{\boldsymbol{o}}_r \qquad \dot{\hat{\boldsymbol{o}}}_h = \boldsymbol{\omega}_{O/N} \times \hat{\boldsymbol{o}}_h = \omega_r \hat{\boldsymbol{o}}_\theta \tag{2.24}$$

Now, considering these identities, the kinetic energy per unit mass of the deputy can be written as:

$$\begin{aligned} K_d = \frac{1}{2}\dot{\boldsymbol{r}}_d \cdot \dot{\boldsymbol{r}}_d = \frac{1}{2}(\dot{x} + v_{t,r} - y\omega_h)^2 + \\ + \frac{1}{2}(\dot{y} + (r_t + x)\omega_h - z\omega_r)^2 + \frac{1}{2}(\dot{z} + y\omega_r)^2 \end{aligned} \tag{2.25}$$

where $v_{t,r}$ is the radial component of the target velocity in LVLH frame. Meanwhile, the potential energy of the deputy is due to J2 perturbation and it can be expressed considering Eq. (2.6) as:

$$U_d = -\frac{\mu}{r_d} - \frac{k_{J2}}{r_d^3}\left(\frac{1}{3} - sin^2(\phi)\right) \tag{2.26}$$

where ϕ is the geocentric latitude of the deputy, while

$$k_{J2} = \frac{3J_2\mu R_e^2}{2} \tag{2.27}$$

is a constant, composed by J_2, which is the second zonal harmonic coefficient of the Earth ($J_2 = 1.0826 \cdot 10^{-3}$), and R_e, the Earth's equatorial radius. In particular, ϕ can be computed through the following identity:

$$sin(\phi) = \frac{r_{d,z}}{r_d} = sin(\theta)sin(i) \tag{2.28}$$

where $r_{d,z}$ is the projection of $\boldsymbol{r}_d$ on the $\hat{Z}$ axis of the ECI frame

$$\begin{aligned} r_{d,z} &= \boldsymbol{r}_d \times \hat{\boldsymbol{Z}} = \\ &= (r_t + x)sin(i)sin(\theta) + ysin(i)cos(\theta) + zcos(i) \end{aligned} \tag{2.29}$$

Substituting Eq. (2.29) into Eq. (2.26) yields to:

$$U_d = -\frac{\mu}{r_d} - \frac{k_{J2}}{3r_d^3} + \frac{k_{J2}r_{d,z}^2}{r_d^5} \tag{2.30}$$

Substituting Eqs. (2.25) and (2.30) into Eq. (2.20), the nonlinear dynamic equations of satellite relative motion can be derived:

$$\begin{cases} \ddot{x}_d = 2\dot{y}_d\omega_h - x_d(\eta_d^2 - \omega_z^2) + y_d\alpha_h - z_d\omega_r\omega_h - (\zeta_d - \zeta)sin(i)sin(\theta) - r_t(\eta_d^2 - \eta^2) \\ \ddot{y}_d = -2\dot{x}_d\omega_h + 2\dot{z}_d\omega_r - x_d\alpha_h - y_d(\eta_d^2 - \omega_h^2 - \omega_r^2) + z_d\alpha_r - (\zeta_d - \zeta)sin(i)cos(\theta) \\ \ddot{z}_d = -2\dot{y}_d\omega_r - x_d\omega_r\omega_h - y_d\alpha_r - z_d(\eta_d^2 - \omega_r^2) - (\zeta_d - \zeta)cos(i) \end{cases} \tag{2.31}$$

while the target's motion around the Earth has been described by followings Eqs:

$$\begin{cases} \dot{r}_t = v_{t,x} \\ \dot{v}_{t,x} = -\frac{mu}{r_t^2} + \frac{h^2}{r_t^3} - k_{J2}\frac{1-3sin^2(i)sin^2(\theta)}{r_t^4} \\ \dot{h} = -k_{J2}\frac{sin^2(i)sin(2\theta)}{r_t^3} \\ \dot{\theta} = \frac{h}{r_t^2} + 2k_{J2}\frac{cos^2(i)sin^2(\theta)}{hr_t^3} \\ \dot{i} = -k_{J2}\frac{sin(2i)sin(2\theta)}{2hr_t^3} \end{cases} \tag{2.32}$$

where ζ and ζ_d represent, respectively, the accelerations of the target and the deputy.

$$\begin{cases} \zeta = \frac{2k_{J2}sin(i)sin(\theta)}{r^4} \\ \zeta_d = \frac{2k_{J2}r_{d,z}}{r_d^5} \end{cases} \tag{2.33}$$

the angular velocities η and η_d can be obtained from

$$\begin{cases} \eta^2 = \frac{\mu}{r^3} + \frac{k_{J2}}{r^5} - \frac{5k_{J2}sin^2(i)sin^2(\theta)}{r^5} \\ \eta_d^2 = \frac{\mu}{r_d^3} + \frac{k_{J2}}{r_d^5} - \frac{5k_{J2}r_{jZ}^2}{r_d^7} \end{cases} \tag{2.34}$$

and, finally, the steering acceleration α_r and the orbital acceleration α_h are computed by

$$\begin{cases} \alpha_r = \dot{\omega}_r = -\frac{k_{J2}sin(2i)cos(\theta)}{r_t^5} + \frac{3v_{t,x}k_{J2}sin(2i)sin(\theta)}{r_t^4 h} - \frac{8k_{J2}^2 sin^3(i)cos(i)sin^2(\theta)cos(\theta)}{r_t^6 h^2} \\ \alpha_h = \dot{\omega}_h = -\frac{2hv_{t,x}}{r_t^3} - \frac{k_{J2}sin^2(i)sin(2\theta)}{r_t^5} \end{cases} \tag{2.35}$$

2.2.2 On-board Dynamics

Contrarily to the simulation dynamics, which is affected by nonlinear terms both in the perturbed and in the unperturbed case, the deputy works adopting an easier dynamical model, characterized by linearized equations of relative motion. To obtain these equations, the following assumption shall be made: the distance between the target and the Earth is much greater than that between the target and the deputy. In this way, when $[(x, y, z) <<< r_t]$, the orbit radius of the deputy r_d can be approximated as:

$$r_d = r_t\sqrt{1 + 2\frac{x}{r_t} + \frac{x^2 + y^2 + z^2}{r_t^2}} \approx r_t\sqrt{1 + 2\frac{x}{r_t}} \tag{2.36}$$

and this will affect the right-hand term of the Eq. (2.13), which is approximated to:

$$\frac{\mu}{r_d^3} \approx \frac{\mu}{r_t^3}\left(1 - 3\frac{x}{r_t}\right) \tag{2.37}$$

So, considering Eqs. (2.17) and neglecting higher order terms, the following approximations can be performed:

$$\frac{\mu(r_t + x)}{[(r_t + x)^2 + y^2 + z^2]^{\frac{3}{2}}} \approx \frac{\mu(r_t + x)}{r_t^3}\left(1 - 3\frac{x}{r_t}\right) \approx \frac{\mu}{r_t^2} - 4n^2 x \tag{2.38}$$

$$\frac{\mu y}{[(r_t + x)^2 + y^2 + z^2]^{\frac{3}{2}}} \approx \frac{\mu y}{r_t^3}\left(1 - 3\frac{x}{r_t}\right) \approx n^2 y \tag{2.39}$$

$$\frac{\mu z}{[(r_t + x)^2 + y^2 + z^2]^{\frac{3}{2}}} \approx \frac{\mu z}{r_t^3}\left(1 - 3\frac{x}{r_t}\right) \approx n^2 z \tag{2.40}$$

Merging together Eqs. (2.38)-(2.40) into Eq. (2.17), the *Hill-Clohessy-Wiltshire equations* [4] can be found:

$$\begin{cases} \ddot{x} = 2n\dot{y} + 3n^2 x \\ \ddot{y} = -2n\dot{x} \\ \ddot{z} = -n^2 z \end{cases} \tag{2.41}$$

In state-space form, Eq. (2.41) can be written as

$$\dot{\boldsymbol{x}} = \begin{bmatrix} 0 & 0 & 0 & 1 & 0 & 0 \\ 0 & 0 & 0 & 0 & 1 & 0 \\ 0 & 0 & 0 & 0 & 0 & 1 \\ 3n^2 & 0 & 0 & 0 & 2n & 0 \\ 0 & 0 & 0 & -2n & 0 & 0 \\ 0 & 0 & -n^2 & 0 & 0 & 0 \end{bmatrix} \boldsymbol{x} = \boldsymbol{A}\boldsymbol{x} \tag{2.42}$$

where $\boldsymbol{x} = [x, y, z]$ is the state vector and $\boldsymbol{A}$ collects the constant term of set of differential equations. Moreover, being Eq. (2.41) ordinary differential equations, the closed solution can be found:

$$\begin{cases} x(t) = (4 - 3cos(nt))x_0 + \frac{sin(nt)}{n}\dot{x}_0 + \frac{2}{n}(1 - cos(nt))\dot{y}_0 \\ y(t) = 6(sin(nt) - nt)x_0 + y_0 - \frac{2}{n}(1 - cos(nt))\dot{x}_0 + \frac{4sin(nt) - 3nt}{n}\dot{y}_0 \\ z(t) = z_0 cos(nt) + \frac{\dot{z}_0}{n} sin(nt) \end{cases} \tag{2.43}$$

where $[x_0, y_0, z_0, \dot{x_0}, \dot{y_0}, \dot{z_0}]$ are the initial conditions on the position and the velocity vector of the deputy in the LVLH frame.

2.3 Football orbit and Stationary condition

2.3.1 Planar Football orbit

The relative motion orbit should be chosen according to the parameters of target, deputy and the aims of the mission. In order to inspect the desired target, to optimize the performances on the trajectory control and to make easier the problem, a **football orbit** has been selected to perform the inspection mission. This kind of motion is one of the choices adopted for the Close Proximity Operations, and it relies on the natural orbital motion to maintain a desired relative location. In other words: the satellite performs a station keeping, requiring minimal fuel consumption. Typically, the relative football orbit assumes a shape of an elliptical orbit, that is employed to keep the deputy in a holding pattern downrange from the target for station keeping, but it is also used to have the deputy circumnavigate or orbit about the target for inspections. Theoretically, the relative orbit shall remain the same along the mission, with the same shape and dimensions, and without any perturbations. So it is necessary for the relative motion to be bounded: after a certain time (it usually fixed as *orbital period* to orbit around Earth), as it can be seen in Eq. (2.43), the out-of-plane component *z(t)* and the radial component *x(t)* already satisfy this requirement for any initial condition. The same is not valid for the along-track component *y(t)*, which includes a secular term:

$$y_{sec} = -3t\dot{y}_0 - 6ntx_0 \tag{2.44}$$

which will grow indefinitely as time passes. To have a bounded relative motion and a repeating relative orbit, the condition shall be imposed as:

$$y_{sec} = 0 \tag{2.45}$$

To do it, a constraint shall be defined as:

$$\dot{y}_0 = -2x_0 n \tag{2.46}$$

allowing also the y coordinate to be bounded.
A relevant detail is the relation between the energy and orbit dimension: fixing the position vector, a simple ΔV variation in any directions becomes a variation of orbit shape, moving the apogee or perigee position based on the velocity magnitude and direction, changing so the eccentricity of the orbit. In fact, going back to ECI frame, the semi-major axis defines the energy of the orbit:

$$\epsilon = -\frac{\mu}{2a} = \frac{v^2}{2} - \frac{\mu}{r} \tag{2.47}$$

If target and deputy have the same orbital energy, they are in a *periodic relative motion* around each other. Then, vis-viva equation can be derived from Eq. (2.47):

$$v^2 = \mu\left(\frac{2}{r} - \frac{1}{a}\right) \tag{2.48}$$

This equation describes the ideal motion performed along the elliptical orbit, where the relative effect is to have the deputy arch upward and then slowly drift back: when the deputy reaches apogee and begins to head towards perigee, its radial distance decreases and its velocity increases. In fact, as it approaches perigee, its radial distance is less then the target, causing it to move at a faster speed underneath the target. Practically, assuming that at the initial time the deputy stays at y_0 with respect to the target and that no ΔV component is provided in the off-track direction ($z_0 = 0$) (it is also found that $z(t) = 0$ for any time, which means that the relative orbit belongs to the same plane of the spacecrafts orbits), means that the other initial relative component is $x_0 = 0$. These initial conditions describe a *in-plane formation* and the development of its trajectory follows the next equations, that derived from the merging of Eqs. (2.43) and (2.46) and fixing initial conditions:

$$\begin{cases} x(t) = \frac{sin(nt)}{n}\dot{x}_0 \\ y(t) = y_0 + \frac{2}{n}(cos(nt) - 1)\dot{x}_0 \end{cases} \tag{2.49}$$

which is, as expected, the sum of a cyclic motion in the radial direction and an oscillatory motion along the tangential direction with an offset equal to the initial condition y_0. It can be demonstrated that the major and minor axis of the relative orbit ellipse are directly related to the magnitude of the velocity change and they are always one twice the other.

2.3.2 Inclined Football orbit

In addition to the football orbit, there are other types of repeating orbits, as oscillating orbits (oscillatory trajectory of the deputy along the direction perpendicular to the orbital plane of the target, that is off-track direction z), V-bar Stationary, V-bar Approach, R-bar Station Keeping, as presented also in [8],[3],[27],[26]. The combination of two or more of them creates further relative motions. Among them, considering the football orbit and the oscillating orbit, the *inclined football orbit* is present. In this case, starting from initial conditions y_0 and z_0 and imposing an impulsive manoeuvre with ΔV components both in the radial and off-track direction ($\dot{x}_0$ and $\dot{z}_0$) in addition to the component in along-track direction to remove secular term Eq. (2.46), the following set of equations can be derived:

$$\begin{cases} x(t) = \frac{sin(nt)}{n}\dot{x}_0 \\ y(t) = y_0 + \frac{2}{n}(cos(nt) - 1)\dot{x}_0 \\ z(t) = \frac{\dot{z}_0}{n}sin(nt) \end{cases} \tag{2.50}$$

which, as it can be seen, exhibits an oscillatory motion in the z direction too. Unfortunately, the motion just described is constrained to have the same projection on xy-plane along the entire time of simulation. For small inclination of the relative orbit along the z-axis, this formula could be also considered for environment where it try to maintain the same size of orbit. As soon as the inclination increases, another model shall be assumed. For previous reasons, this thesis proposes an introduction of a new model concept, where the motion can be modelled by 3 coordinates, expressed as:

- ρ, that represents the radius amplitude of relative orbit.
- α, (or *azimuth*) that represents the inclination of the relative orbit along the z-axis respect to the xy-plane
- β, (or *reduced latitude* or *eccentric anomaly*) that is defined by the radius drawn from the centre of the ellipse to a certain point on the surrounding sphere (that shares with ellipse the same major radius) which is the projection parallel to the major axis of a single point on the ellipse at a defined latitude. In practice, β allows to reduce the size of the orbit, avoiding to change the shape of the orbit and the proportion between major and minor radius.

The following graph shows an application of β. As it can be seen, Fig. 2.2a proves that, at switching of the value of β and fixing one of α and one of ρ, the highest points of these orbits (indicated by the colored points in the plot) maintain the same distance. Moreover, as Fig 2.2b presents, the z-axis component remains the same.

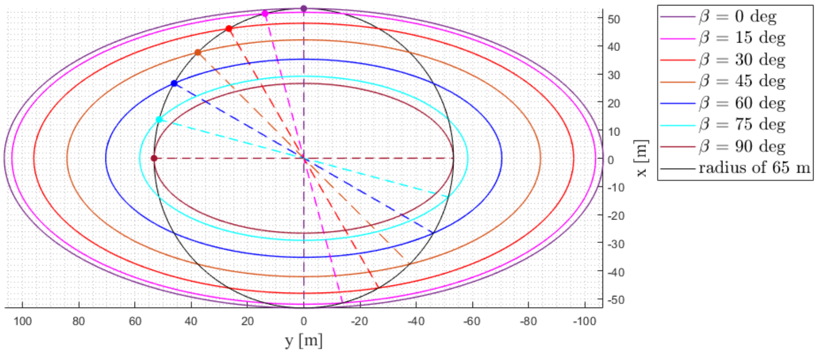

(a) xy-plane

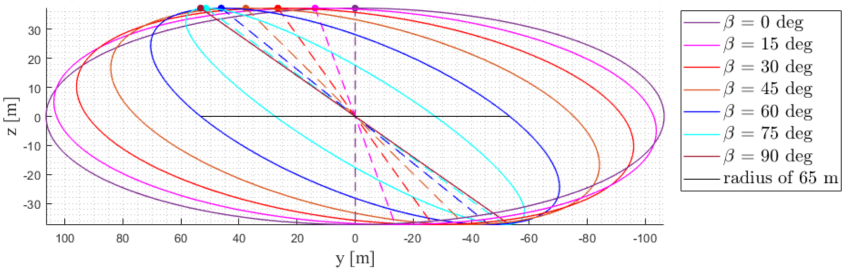

(b) yz-plane

Figure 2.2: Meaning of β, fixing $\alpha = 35$ [deg] and $\rho = 65$ [m]

A relevant advantage of the formalization of these angles is the fact that a desired orbit, characterized by a specific shape and size, can be translated and rotated adopting these angles, improving the classical model proposed by literature. So, using this approach and considering an ellipsoid model and Eq. (2.46), a general initial state vector can be expressed as:

$$x_{hcw} = \begin{bmatrix} \rho cos\alpha cos\beta \\ \rho sin\beta cos\alpha \\ \rho sin\alpha \\ (n\rho/2) sin\beta cos\alpha \\ -2n\rho cos\alpha cos\beta \\ 0 \end{bmatrix} = \rho \begin{bmatrix} 0 & 0 & 1 & 1 & 1 \\ 0 & 1 & 1 & 0 & 1 \\ 1 & 0 & 0 & 0 & 1 \\ 0 & 1 & 1 & 0 & n/2 \\ 0 & 0 & 1 & 1 & -2n \\ 0 & 0 & 0 & 0 & 0 \end{bmatrix} \begin{bmatrix} sin\alpha \\ sin\beta \\ cos\alpha \\ cos\beta \\ 1 \end{bmatrix} \tag{2.51}$$

2.3.3 Application of Stationary Conditions

In order to obtain numerical results and preliminary simulations, 3 configurations, described by initial conditions, can be tested and compared in Fig. 2.3:

1. Stationary orbit, given by Eq. (2.46) and definition of the constant ρ

$$\begin{cases} x_0 = \rho & \dot{x}_0 = 0 \\ y_0 = 0 & \dot{y}_0 = -2n\rho \\ z_0 = 0 & \dot{z}_0 = 0 \end{cases} \tag{2.52}$$

   This set of conditions comes from [3]: four conditions are given by imposing zero along-track drift and offset, providing one of the easiest configuration of football orbit. In particular, as it can be seen in Eq. (2.53), the cross-track oscillation can have the same phase, while the amplitude is function of radial direction oscillation and a constant $\boldsymbol{k}$, that determine the inclination with respect to z-axis in LVLH frame.

$$\begin{cases} y_0 = 2n\dot{x}_0 \\ \dot{y}_0 = -2nx_0 \end{cases} \quad \begin{cases} z_0 = \pm \boldsymbol{k} x_0 \\ \dot{z}_0 = \pm \boldsymbol{k} \dot{x}_0 \end{cases} \tag{2.53}$$

   Some possible solutions of $\boldsymbol{k}$ are 2 and $\sqrt{3}$, which identify a relative inclined orbit, respectively, of 26.56° or 30° with respect to the cross-track direction.

2. Unstationary orbit (y-axis propagating orbit)

$$\begin{cases} x_0 = \frac{\rho}{2} & \dot{x}_0 = 0 \\ y_0 = 0 & \dot{y}_0 = -\frac{34}{29} n\rho \\ z_0 = \frac{\rho}{2} & \dot{z}_0 = -\frac{13}{33} n\rho \end{cases} \tag{2.54}$$

   If the identity Eq. (2.46) has not been applied, the set of conditions, described in Eq. (2.54), shows a typical example of no stationary orbit, where the motion cannot be seen as repeating relative orbit.

3. Stationary orbit, given by Eq. (2.51) and definition of the constant ρ
   Fixing $\alpha = 30$ and $\beta = 60$, the initial conditions are the following:

$$\begin{cases} x_0 = \sqrt{3}\rho/4 & \dot{x}_0 = 3n\rho/8 \\ y_0 = 3\rho/4 & \dot{y}_0 = -n\sqrt{3}\rho/2 \\ z_0 = \rho/2 & \dot{z}_0 = 0 \end{cases} \tag{2.55}$$

As Fig. 2.3 shows, the application of the new model allows to remain within the same orbit independently from the rotation considered.

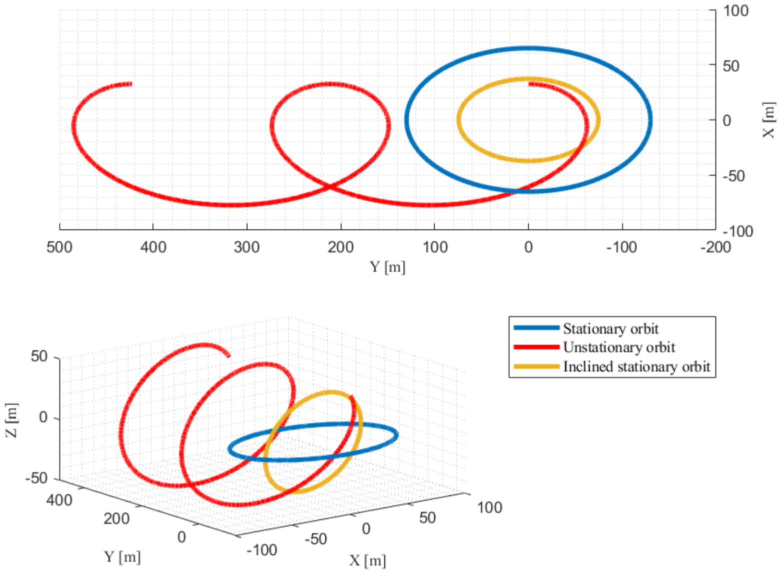

Figure 2.3: Comparison between initial conditions

2.4 Manoeuvre

In this section, the focus is oriented to the correction of the real trajectory in according to the reference trajectory. So, based on the error given by the comparison of these data, the deputy can choose autonomously to perform a correction manoeuvre. In the preliminary analysis, an assigned Time of Flight (called also *ToF*) shall be chosen to understand how much ΔV is necessary, meanwhile the degree of autonomy will increase during the development of the treatment. To do that, two important elements shall be mentioned: the state transition matrix and the minimization problem.

2.4.1 State Transition Matrix

Starting from the first kind of strategies, when the ToF is assigned, the *State Transition Matrix* (or *STM*) has been considered. It consists into converting the closed form of Eq. (2.43) into matrix notation.

$$\vec{x}(t) = \vec{\Phi}(t)(\vec{x}_0 + [\vec{0}_{3x1}; \Delta\vec{V}]^T) \tag{2.56}$$

with the STM expressed as:

$$\vec{\Phi}(t) = \begin{bmatrix} 4 - 3cos(nt) & 0 & 0 & \frac{1}{n}sin(nt) & \frac{2}{n}(1 - cos(nt)) & 0 \\ 6(sin(nt) - nt) & 1 & 0 & -\frac{2}{n}(1 - cos(nt) & \frac{4sin(nt) - 3nt}{n} & 0 \\ 0 & 0 & cos(nt) & 0 & 0 & \frac{sin(nt)}{n} \\ 3nsin(nt) & 0 & 0 & cos(nt) & 2nsin(nt) & 0 \\ -6n(1 - cos(nt)) & 0 & 0 & -2sin(nt) & 4cos(nt) - 3 & 0 \\ 0 & 0 & -nsin(nt) & 0 & 0 & cos(nt) \end{bmatrix} \tag{2.57}$$

In practice, the advantage of using the STM is based on the recovering of the relative position at each time, avoiding the propagation from t_0 to the desired time. Passing from a set of ordinary differential equations to a set of algebraic equations, the algorithm reduces the computational cost of the entire mission.
From that, the 2^{nd} element can be introduced.

2.4.2 Minimization problem and conditions

To develop a guidance algorithm, this thesis proposes to build a *two points boundary value problem.* In fact, the first goal of that part of the algorithm will be to minimize the fuel consumption in order to return onto the nominal orbit and perform the inspection phase. This will be done passing through two steps:

1. Fixing the time duration of the manoeuvre;
2. Selecting a time interval from which an adequate ToF can be obtained.

In the first case, the problem has been defined in the following way:

- Considering an initial conditions, as state vector x;
- Assuming an initial guess;
- Fixing the constraints.

If the 2^{nd} point is characterized by choosing of velocity vector guess and ToF guess, the 3^{rd} can be represented in the objective function of the minimization problem. In that case, fixing a ToF, the nominal orbit will be propagated starting from initial time until final time manoeuvre and it will be necessary to recover the state vector in the last instant, which shall match the final point of manoeuvre arc.

$$\min_{\vec{x}_1} \ \Delta v \quad \text{s.t.} \begin{cases} \boldsymbol{r}_1 = \boldsymbol{r}_i(t_1) \\ \boldsymbol{r}(ToF) = \boldsymbol{r}_f(t_2) \\ t_i \leq t_1 \leq t_f \\ t_2 = t_1 + ToF \end{cases} \tag{2.58}$$

where $\Delta v = \Delta v_1 + \Delta v_2$, $\boldsymbol{\Delta v}_1 = \boldsymbol{v}_1 - \boldsymbol{v}_E(t_1)$, $\boldsymbol{\Delta v}_2 = \boldsymbol{v}(t_2) - \boldsymbol{v}_M(t_2)$. $\boldsymbol{x}_1 = (\boldsymbol{r}_1, \boldsymbol{v}_1)^\top$, and $(\boldsymbol{r}(t), \boldsymbol{v}(t))^\top = \vec{\Phi}(\boldsymbol{x}_1, t_1; t_2)$. Defining lower and upper bounds, the problem stated in Eq. (2.58) will be ready to compute solution.
Instead, in the second case, it will not be necessary to give an exact time value, but just selecting a desired time interval, where the algorithm can perform and choose the best value in terms of time to reduce the Δv. Apart from this time constrain, in general, this kind of problem can be characterized by 2 classes of constraints:

- Equality, where the value, generated by initial guess, shall be equal to boundary constraint value;
- Inequality, where the value shall be necessarily lower or higher than boundary constraint value.

If the time constraints enter in the 2^{nd} category, other constraints (related to Δv, for example) could stay in the 1^{st}.

$$\min_{\vec{x}_1, ToF} \ \Delta v \quad \text{s.t.} \begin{cases} \boldsymbol{r}_1 = \boldsymbol{r}_i(t_1) \\ \boldsymbol{r}(ToF) = \boldsymbol{r}_f(t_2) \\ t_i \leq t_1 \leq t_f \\ ToF_L \leq ToF \leq ToF_U \\ t_2 = t_1 + ToF \\ \boldsymbol{dv}_{1,j} \leq \boldsymbol{v}_{u,j} \\ \boldsymbol{dv}_{2,j} \leq \boldsymbol{v}_{u,j} \end{cases} \tag{2.59}$$

where $\Delta v = \Delta v_1 + \Delta v_2$, $\boldsymbol{\Delta v}_1 = \boldsymbol{v}_1 - \boldsymbol{v}_E(t_1)$, $\boldsymbol{\Delta v}_2 = \boldsymbol{v}(t_2) - \boldsymbol{v}_M(t_2)$. $\boldsymbol{x}_1 = (\boldsymbol{r}_1, \boldsymbol{v}_1)^\top$, and $(\boldsymbol{r}(t), \boldsymbol{v}(t))^\top = \vec{\Phi}(\boldsymbol{x}_1, t_1; t_2)$.. Also here, defining lower and upper bounds, the problem stated in Eq. (2.59) can be formalized.

2.5 Validation of sets of equations

In order to use the sets of equations already exposed, a validation shall be done. To understand the reliability of these, *Two-Body Problem* (*2BP*) (with or without J2 perturbation term) has been implemented, defining the state of target and deputy, as [12] shows. Define the inertial equations of motion for both satellites.

$$\ddot{\boldsymbol{r}}_{\boldsymbol{t}} = -\frac{\mu}{r_t^3}\boldsymbol{r}_{\boldsymbol{t}} + \boldsymbol{F}_{\boldsymbol{J2,t}} \tag{2.60}$$

$$\ddot{\boldsymbol{r}}_{\boldsymbol{d}} = -\frac{\mu}{r_d^3}\boldsymbol{r}_{\boldsymbol{d}} + \boldsymbol{F}_{\boldsymbol{J2,d}} \tag{2.61}$$

where, in the perturbed case

$$\boldsymbol{F}_{\boldsymbol{J2,t}} = -\frac{3\mu J_2 R_e^2}{r_t^4}\begin{bmatrix} \frac{1}{2} - \frac{3sin^2(i_t)sin^2(\theta_t)}{2} \\ sin^2(i_t)sin(\theta_t)cos(\theta_t) \\ sin(i_t)cos(i_t)sin(\theta_t) \end{bmatrix} ; \boldsymbol{F}_{\boldsymbol{J2,d}} = -\frac{3\mu J_2 R_e^2}{r_d^4}\begin{bmatrix} \frac{1}{2} - \frac{3sin^2(i_d)sin^2(\theta_d)}{2} \\ sin^2(i_d)sin(\theta_d)cos(\theta_d) \\ sin(i_d)cos(i_d)sin(\theta_d) \end{bmatrix} \tag{2.62}$$

The *inertial relative* position and velocity are defined as the position and velocity of the deputy relative to the target.

$$[\boldsymbol{\rho}]_N = \boldsymbol{r}_{\boldsymbol{d}} - \boldsymbol{r}_{\boldsymbol{t}} \tag{2.63}$$

$$[\dot{\boldsymbol{\rho}}]_N = \dot{\boldsymbol{r}}_{\boldsymbol{d}} - \dot{\boldsymbol{r}}_{\boldsymbol{t}} \tag{2.64}$$

$$\tag{2.65}$$

The relative position in the LVLH is calculated using the rotation matrix $[C_{O/N}]$ as

$$[\boldsymbol{\rho}]_O = [C_{O/N}][\boldsymbol{\rho}]_N \tag{2.66}$$

$$[C_{O/N}] = \begin{bmatrix} \hat{o}_r & \hat{o}_\theta & \hat{o}_h \end{bmatrix} \tag{2.67}$$

The terms of $[C_{O/N}]$ are summarized in Eq. (2.8) while the relative velocity in the LVLH frame is defined using the *transport theorem* as

$$[\dot{\boldsymbol{\rho}}]_O = [\dot{\boldsymbol{\rho}}]_N - \boldsymbol{\omega}_{O/N} \times [\boldsymbol{\rho}]_O \tag{2.68}$$

where $\boldsymbol{\omega}_{O/N}$ is the rotation rate of the LVLH frame, and is defined as

$$\boldsymbol{\omega}_{O/N} = \frac{\boldsymbol{r}_t \times \dot{\boldsymbol{\rho}}_t}{r_t^2} \tag{2.69}$$

Then, Eqs. (2.66) and (2.68) are compared, respectively, to sets of Eqs. (2.17) and (2.31). As Fig. 2.4 shows, the nonlinear dynamical models respect faithfully the behaviour of *Two Body Problem*, with an error lower than the order of millimeters.

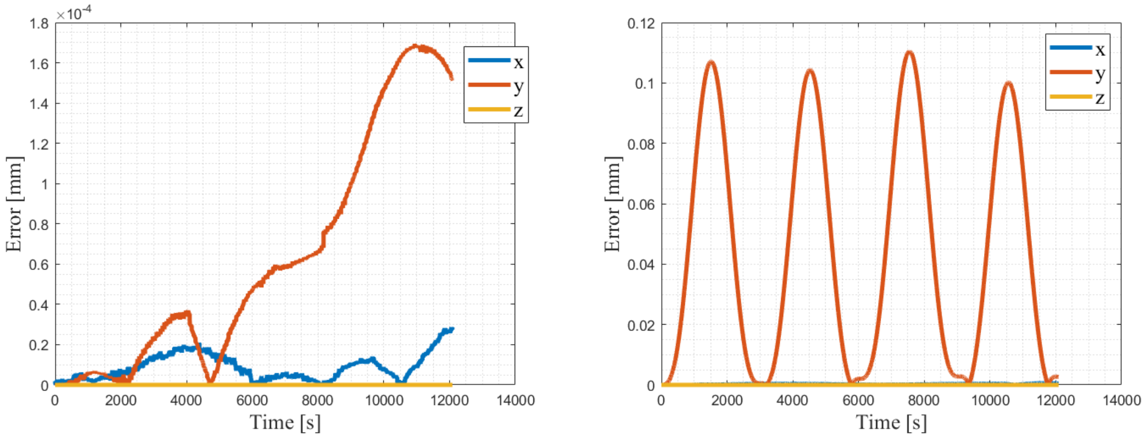

(a) Unperturbed case

(b) Perturbed case

Figure 2.4: Comparison between 2BP - NERM

After these comparisons, Eqs. (2.17) and (2.31) will be compared to Eq. (2.41).
As expected, the adding of the perturbation term contributes to increase the error between linear and nonlinear dynamical models. As it can be noticed in Fig. 2.5, the y-component turns out to be the most affected term.

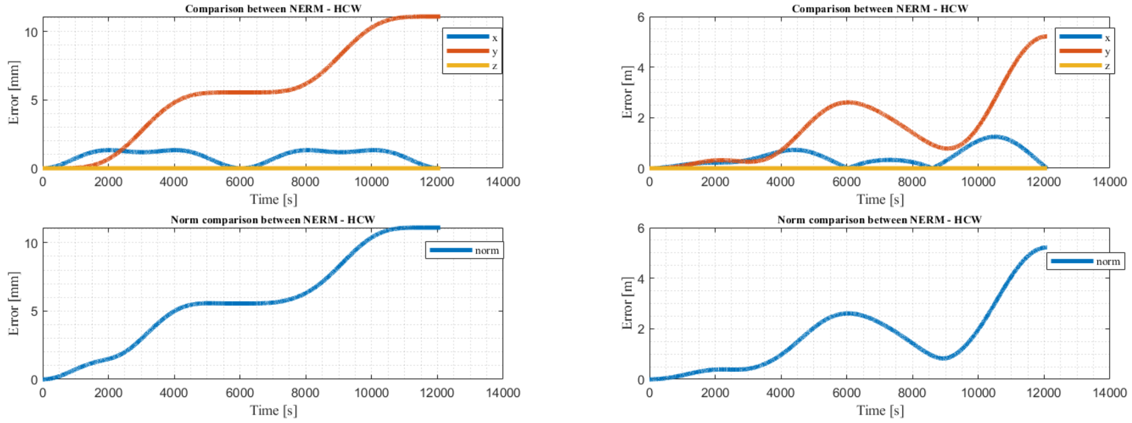

(a) Unperturbed case

(b) Perturbed case

Figure 2.5: Comparison between HCW - NERM

Finally, Fig. 2.6 shows the behaviour of the relative orbits propagated with the different dynamical models. While the Fig. 2.6a proves a similarity between dynamical models also after a certain simulation time (in this case, 10 orbital periods), the Fig. 2.6b shows that the z-component of the NERM diverges significantly with respect to the HCW, distorting the nature of the original orbit.

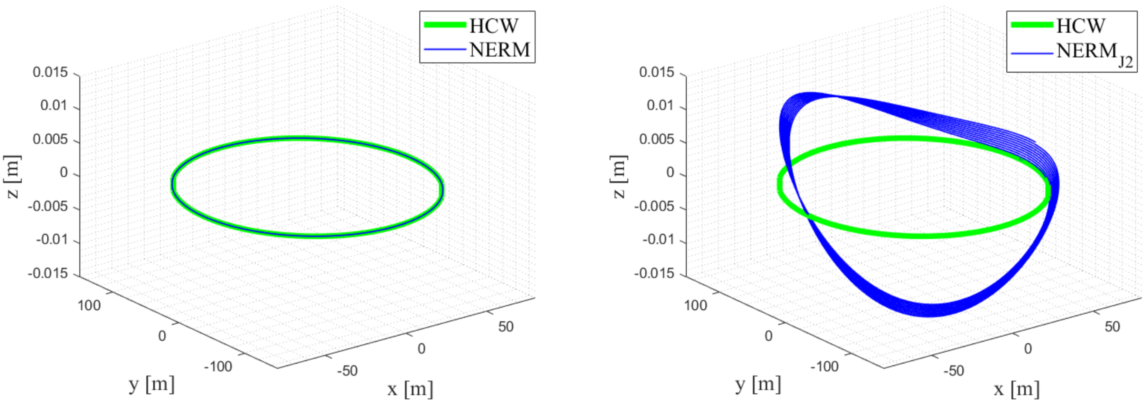

(a) Unperturbed case

(b) Perturbed case

Figure 2.6: Comparison between HCW - NERM orbits, propagated for 10 orbital periods

Chapter 3

Navigation

This second part will be focused on the navigation system. First of all, the choice of the filter used will be discussed along with the theory behind it. Then, the attitude of the chosen target will be studied and finally, the measurement model adopted will be presented.

3.1 Introduction

In general, the estimation of the relative position of the deputy and the prediction of the target's attitude require complex computations, but on-board, space processors have only a limited computational power. So, the main goal is to implement efficient algorithms with limited computational cost, guaranteeing a sufficient accuracy and the necessary performance.

Nowadays, the Extended Kalman Filter is the preferred filter for estimation algorithms. It uses the first-order Taylor expansion to linearize the equations of motion and the measurements equation, leading to inaccuracy in case of complex dynamics or poor number of available measurements. Therefore, the Unscented Kalman Filter is preferred, to account for non linearities. It is based on the Unscented Transform which directly propagates sample points through the nonlinear system. Removing the linearization process, the UKF gives better performance with respect to the EKF in highly nonlinear cases.

3.2 Unscented Kalman Filter

The core of every Kalman Filter is based on two steps:

- prediction, during which the mean and the covariance of the next time step are propagated using the equations of motion;
- update, during which the residual between the predicted and the real measurements is used to correct the predicted state.

Due to the complex dynamics of external dynamics given by the NERM, a nonlinear Kalman Filter has been implemented, in particular, the Unscented Kalman Filter. In this kind of filter, the prediction step is based on the Unscented Transform.

3.2.1 Unscented Transform

This transformation is based on the concept that ”it is easier to approximate a Gaussian (probability) distribution than to approximate an arbitrary non linear function or transformation” [23]. In other words, this transformation finds a parameterization which can accurately describes the mean and the covariance of the initial variable and which can be used to directly propagate the information through the nonlinear equations.

The procedure of the UT is the following. First of all, the mean $\boldsymbol{m}$ and the covariance $\boldsymbol{P}$ of the m-dimensional state vector $\boldsymbol{x}$ are approximated using a set of carefully chosen $2m+1$ sigma points, which are collected in a structure χ:

$$\chi^{[1]} = \boldsymbol{m} \tag{3.1}$$

$$\chi^{[i]} = \begin{cases} \boldsymbol{m} + (\sqrt{(m+\lambda)\boldsymbol{P}})_{i-1}, & i = 2, ..., m+1 \\ \boldsymbol{m} - (\sqrt{(m+\lambda)\boldsymbol{P}})_{i-m-1}, & i = m+2, ..., 2m+1 \end{cases} \tag{3.2}$$

whereas $(\sqrt{(m+\lambda)\boldsymbol{P}})_i$ is the ith row or column of the matrix square root of $(m+\lambda)\boldsymbol{P}$ and λ is a scaling parameter defined as:

$$\lambda = \alpha^2(m+k) - m \tag{3.3}$$

where $k \geq 0$ and $\alpha \in (0,1]$ define how far from the mean the sigma points are located, and $\beta = 2$ (optimal choice for Gaussian distributions).
Then, two weights are associated to each of the sigma points, defined as:

$$w_{m,1} = \frac{\lambda}{m+\lambda} \tag{3.4}$$

$$w_{P,1} = w_{m,1} + (1 - \alpha^2 + \beta) \tag{3.5}$$

$$w_{m,i} = w_{P,i} = \frac{1}{2(m+\lambda)}, \qquad i = 2, ..., 2m+1 \tag{3.6}$$

where $w_{m,i}$ is the weight associated to sigma points correlated to the mean, while $w_{P,i}$ is the weight associated to sigma points correlated to the covariance. The selection of the sigma points must be such that the following equations are respected:

$$\sum_{i=1}^{2m+1} w_{m,i} = 1 \tag{3.7}$$

$$\boldsymbol{m} = \sum_{i=1}^{2m+1} w_{m,i}\chi^{[i]} \tag{3.8}$$

$$\boldsymbol{P} = \sum_{i=1}^{2m+1} w_{P,i}[\chi^{[i]} - \boldsymbol{m}][\chi^{[i]} - \boldsymbol{m}]^T \tag{3.9}$$

Prediction step

The prediction step consists in a set of sigma points around the initial conditions along with their relative weights. Then, the set is propagated through the process model, in this case the closed solution of the HCW:

$$\chi_{k+1}^{[i]} = \boldsymbol{\Phi}(t_{k+1}; \chi_k^{[i]}, t_k) \tag{3.10}$$

where $\boldsymbol{\Phi}$ indicates the HCW.
Finally, the mean and the covariance are evaluated by weighting each propagated sigma point:

$$\boldsymbol{m}_{k+1}^{-} = \sum_{i=1}^{2m+1} w_{m,i} \mathcal{X}_{k+1}^{[i]} \tag{3.11}$$

$$\boldsymbol{P}_{k+1}^{-} = \sum_{i=1}^{2m+1} w_{P,i} [\mathcal{X}_{k+1}^{[i]} - \boldsymbol{m}_{k+1}^{-}][\mathcal{X}_{k+1}^{[i]} - \boldsymbol{m}_{k+1}^{-}]^T \tag{3.12}$$

The same approach is repeated for the measurement vector, for which each sigma point is propagated through the observation model, in this case using the NERM:

$$Z_{k+1}^{[i]} = \boldsymbol{h}(\mathcal{X}_{k+1}^{[i]}, t_k) \tag{3.13}$$

where $\boldsymbol{h}$ indicates the NERM.
Then, the predicted measurements are computed:

$$\boldsymbol{n}_{k+1}^{-} = \sum_{i=1}^{2m+1} w_{m,i} Z_{k+1}^{[i]} \tag{3.14}$$

Considering an independent and additive observation noise, the covariance matrix for the measurement and the cross-covariance matrix for the state are computed as:

$$\boldsymbol{P}_{k+1}^{zz} = \sum_{i=1}^{2m+1} w_{P,i} [Z_{k+1}^{[i]} - \boldsymbol{n}_{k+1}^{-}][Z_{k+1}^{[i]} - \boldsymbol{n}_{k+1}^{-}]^T + \boldsymbol{R}_{k+1} \tag{3.15}$$

$$\boldsymbol{P}_{k+1}^{xz} = \sum_{i=1}^{2m+1} w_{P,i} [\mathcal{X}_{k+1}^{[i]} - \boldsymbol{m}_{k+1}^{-}][Z_{k+1}^{[i]} - \boldsymbol{n}_{k+1}^{-}]^T \tag{3.16}$$

where $\boldsymbol{R}$ is the measurement noise matrix.
Now, the prediction step is completed and the filtering can continue with the update step.

Update step

The update step consists in the correction of the predicted mean and covariance using the acquired and predicted measurement. The Kalman gain matrix is computed as:

$$\boldsymbol{K}_{k+1} = \boldsymbol{P}_{k+1}^{xz} (\boldsymbol{P}_{k+1}^{zz})^{-1} \tag{3.17}$$

and the mean and covariance are:

$$\boldsymbol{m}_{k+1}^{+} = \boldsymbol{m}_{k+1}^{-} + \boldsymbol{K}_{k+1} (\boldsymbol{z}_{k+1} - \boldsymbol{n}_{k+1}^{-}) \tag{3.18}$$

$$\boldsymbol{P}_{k+1}^{+} = \boldsymbol{P}_{k+1}^{-} - \boldsymbol{K}_{k+1} \boldsymbol{P}_{k+1}^{zz} \boldsymbol{K}_{k+1}^{T} \tag{3.19}$$

In this case, the measurements are simulated by the NERM propagation. In fact, the NERM are propagated in the simulator environment and then the position of the markers is computed. Finally, noises are added and the measurement is passed to the filter.

3.3 Target's attitude

In this thesis, two cases will be considered:

- fixed target: the target will be considered fixed in space and the principal axes of it will be rotated of some random angle with respect to the LVLH reference frame, leading to a constant rotation matrix;
- tumbling target: the target will be tumbling with a fixed angular velocity and the rotation matrix will be obtained by the MRP.

In the second case, the target's attitude is built using the Modified Rodrigues Parameters. First of all, the initial condition for the Euler Angles is transformed using the conversion to quaternions, described in [15]:

$$\boldsymbol{q} = \begin{bmatrix} cos(\psi/2) \\ 0 \\ 0 \\ sin(\psi/2) \end{bmatrix} \begin{bmatrix} cos(\theta/2) \\ 0 \\ sin(\theta/2) \\ 0 \end{bmatrix} \begin{bmatrix} cos(\phi/2) \\ sin(\phi/2) \\ 0 \\ 0 \end{bmatrix} \tag{3.20}$$

$$= \begin{bmatrix} cos(\phi/2)cos(\theta/2)cos(\psi/2) + sin(\phi/2)sin(\theta/2)sin(\psi/2) \\ sin(\phi/2)cos(\theta/2)cos(\psi/2) - cos(\phi/2)sin(\theta/2)sin(\psi/2) \\ cos(\phi/2)sin(\theta/2)cos(\psi/2) + sin(\phi/2)cos(\theta/2)sin(\psi/2) \\ cos(\phi/2)cos(\theta/2)sin(\psi/2) - sin(\phi/2)sin(\theta/2)cos(\psi/2) \end{bmatrix} \tag{3.21}$$

where ψ, θ and ϕ are the rotation angles.
Then, the quaternions are converted in the MRP, described in [24]:

$$\boldsymbol{\zeta} = \frac{\tilde{\boldsymbol{q}}}{1 + q_0} \tag{3.22}$$

where the $\tilde{\boldsymbol{q}}$ is the vector part of the quaternion and q_0 is the scalar part. Now, the rotation matrix can be computed as:

$$\boldsymbol{\Gamma}(\boldsymbol{\zeta}) = \boldsymbol{I}_3 - \alpha_1^A[\boldsymbol{\zeta}\times] + \alpha_2^A[\boldsymbol{\zeta}\times]^2 \tag{3.23}$$

$$\begin{cases} \alpha_1^A = 4\frac{1-\boldsymbol{\zeta}^{\boldsymbol{T}}\boldsymbol{\zeta}}{(1+\boldsymbol{\zeta}^{\boldsymbol{T}}\boldsymbol{\zeta})^2} \\ \alpha_2^A = 8\frac{1}{(1+\boldsymbol{\zeta}^{\boldsymbol{T}}\boldsymbol{\zeta})^2} \end{cases} \tag{3.24}$$

where $\boldsymbol{I}_3$ is the identity matrix and $[\boldsymbol{\zeta}\times]$ is the skew symmetric matrix for the MRP, computed as:

$$[\boldsymbol{\zeta}\times] = \begin{bmatrix} 0 & -\zeta(3) & \zeta(2) \\ \zeta(3) & 0 & -\zeta(1) \\ -\zeta(2) & \zeta(1) & 0 \end{bmatrix} \tag{3.25}$$

where $\zeta(1)$, $\zeta(2)$ and $\zeta(3)$ are the three components of the vector $\boldsymbol{\zeta}$.
The time evolution of the MRP is governed by Eq. (3.26)

$$\dot{\boldsymbol{\zeta}} = \frac{1}{4}\boldsymbol{\Sigma}(\boldsymbol{\zeta})\boldsymbol{\omega_r} \tag{3.26}$$

$$\boldsymbol{\Sigma}(\boldsymbol{\zeta}) = (1 - \boldsymbol{\zeta}^{\boldsymbol{T}}\boldsymbol{\zeta})\boldsymbol{I}_3 + 2\boldsymbol{\zeta}\boldsymbol{\zeta}^{\boldsymbol{T}} + 2[\boldsymbol{\zeta}\times] \tag{3.27}$$

To find the MRP, Eq. (3.26) is integrated at each time step.

3.4 Measurement model

Assuming to have a known target, information about Envisat's mass, dimensions, center of mass location, moments of inertia, geometrical center and volume will be available. These information are enough to reconstruct the spacecraft position and attitude using some target points, called markers. Therefore, the measurement model is developed considering the marker positions.

Envisat can be modeled as a slender body, a parallelepiped with six surfaces and eight corners of dimensions 10.02 m x 2.75 m x 3.2 m (without solar arrays) [1]. The center of mass tends to shift on one side due to the geometry of the satellite when the solar arrays are opened. The markers are assumed to be positioned on the corners, highlighted in red in Fig. 3.1, for a total of 8 markers, listed in Tab. 3.1.

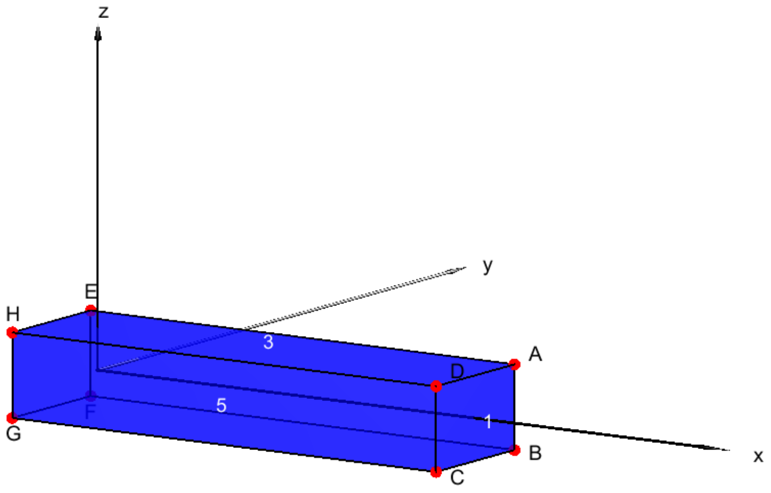

Figure 3.1: Envisat's model.

Marker	ρ_i^{ENV} [m]		
A	+8.9150	-1.3840	-1.5970
B	+8.9150	+1.3840	-1.6030
C	+8.9150	-1.3660	-1.6030
D	+8.9150	-1.3660	+1.5970
E	-1.1050	+1.3840	+1.5970
F	-1.1050	+1.3840	-1.6030
G	-1.1050	-1.3660	-1.6030
H	-1.1050	-1.3660	+1.5970

Table 3.1: Assumed Envisat markers position vectors with respect to its center of mass [23]

The faces are enumerated from 1 to 6 and associated with the normal unit vectors and the 4 visible markers:

Face	$\hat{\eta}_i$	Markers seen
1	$\begin{bmatrix} +1 \\ 0 \\ 0 \end{bmatrix}$	A,B,C,D
2	$\begin{bmatrix} 0 \\ +1 \\ 0 \end{bmatrix}$	A,B,E,F
3	$\begin{bmatrix} 0 \\ 0 \\ +1 \end{bmatrix}$	A,D,E,H
4	$\begin{bmatrix} -1 \\ 0 \\ 0 \end{bmatrix}$	E,F,G,H
5	$\begin{bmatrix} 0 \\ -1 \\ 0 \end{bmatrix}$	C,D,G,H
6	$\begin{bmatrix} 0 \\ 0 \\ -1 \end{bmatrix}$	B,C,F,G

Table 3.2: Envisat main body faces and visible markers relations

Due to the fact that the deputy is turning around the target, not all its faces are visible at the same time, but in the best case a maximum of three faces are visible. Instead, in the worst case, i.e. the camera is normal to the face, only one face is visible. To define which faces are visible, a unit vector defining the face is associated to it and the scalar product between it (in the LVLH frame) and the distance deputy-target is computed. If the following condition is satisfied, the face is visible:

$$\boldsymbol{\rho_d} \cdot \boldsymbol{\Gamma}^T \boldsymbol{\hat{\eta}_i} < 0 \tag{3.28}$$

If the face is visible, the camera is pointed towards it and the associated markers can be exploited.

For the number of visible faces, there are 3 possibilities:

- only one visible face;
- 2 visible faces;
- 3 visible faces.

In the first case, Tab. 3.3 shows the markers associated to the face that will be used as measurements. The number of markers considered is only three because it is the minimum number of points needed to define a plane.

Face	Markers configuration
1	ABC
2	ABE
3	ADE
4	EFH
5	CDG
6	BCF

Table 3.3: 1 face configurations

In the second case, Tab. 3.3 lists all the possible combination of faces and the associated markers. In particular, again a total of three markers is chosen, two from one face and one from the other. In this way, the three markers identify the imaginary plane that passes through the center of mass of the target.

Faces	Markers configuration	Faces	Markers configuration
1-2	ACE	4-5	EDG
1-3	ACE	4-6	HCF
1-5	BDG	2-3	BDE
1-6	BDF	2-6	ACF
4-2	AGE	3-5	EDG
4-3	AGE	5-6	HCF

Table 3.4: 2 faces configurations

Finally, in the last case, the choice of the markers follows the indication given in [23], selecting the three markers creating the triangle with the largest area on the plane of sight, defined by the relative position deputy-target vector and passing through the target center of mass. To find this triangle, the following procedure has been implemented:

1. each marker is projected on the plane of sight:

$$b_i = \frac{\boldsymbol{\rho_d}}{\rho_d} \cdot \boldsymbol{\Gamma^T} \boldsymbol{\rho}_i^{ENV} \tag{3.29}$$

$$\tilde{\boldsymbol{\rho}}_i^{ENV} = \boldsymbol{\Gamma^T} \boldsymbol{\rho}_i^{ENV} - b_i \frac{\boldsymbol{\rho_d}}{\rho_d} \tag{3.30}$$

   where $\tilde{\boldsymbol{\rho}}_i^{ENV}$ is the vector projection of the marker i on the plane of sight, and b_i is the scalar projection of the marker vector $\rho_i^{\widetilde{ENV}}$ on the direction $\boldsymbol{\rho_d}/\rho_d$. Each projection represents the vertex of a number of triangles depending on the number of visible markers;

2. Envisat is modeled as a slender parallelepiped with one predominant principal inertia axis $\hat{v}$ which divides the markers into two groups: the master group, more visible referred to the main face, and the slave group. Then, the inertia axis is projected on the plane of sight too:

$$\tilde{v} = \hat{v} - \left(\frac{\boldsymbol{\rho_d}}{\rho_d} \cdot \hat{v} \right) \frac{\boldsymbol{\rho_d}}{\rho_d} \tag{3.31}$$

$$\tag{3.32}$$

3. Defining a line l through the versor $\tilde{v}$, the triangle with the largest area can be directly found by selecting the two furthest marker projections from the line in the master group and the nearest marker projection in the slave group, where the distance is computed as:

$$d_i = ||\tilde{\boldsymbol{\rho}}_i \times \tilde{v}|| \tag{3.33}$$

$$\tag{3.34}$$

Finally, the measurements are computed separately for each single marker as:

$$\boldsymbol{z_i} = \boldsymbol{\Gamma}^T \boldsymbol{\rho}_i^{ENV} + \boldsymbol{\rho_d} \qquad \text{where i = A,...,H} \tag{3.35}$$

where $\boldsymbol{z_i}$ is the position of the marker i with respect to the deputy center of mass and $\boldsymbol{\Gamma}^T$ the rotation matrix coming from the MRP, described in Eq. (3.23).

3.5 GUT

One of the main purpose of this thesis is to link together the navigation and the guidance systems. In order to do that, during the manoeuvre and the inspection phases, the deputy will estimate its position only through the Unscented Transform. This will result in an estimated state with a larger associated covariance, due to the higher uncertainty.
Moreover, some errors on the covariance are introduced, to reflect reality as much as possible during the manoeuvring of the deputy.

3.5.1 Manoeuvre execution errors

In order to be closer as possible to reality, manoeuvre execution errors must be taken into account during the burning. A simplified way of accounting for them is given by the Gates model [11], which consists of changing the covariance matrix by adding magnitude and pointing error terms. If we denote with t_m the instant of time at which the manoeuvre is executed, as [7] shows, the P matrix is corrected as follows:

$$P(t_m^+) = P(t_m^-) + \begin{bmatrix} 0_{3x3} & 0_{3x3} \\ 0_{3x3} & \sigma_m^2 \boldsymbol{\Delta v} \boldsymbol{\Delta v}^T + \sigma_p^2 [\boldsymbol{\Delta v} \times][\boldsymbol{\Delta v} \times]^T \end{bmatrix} \tag{3.36}$$

where σ_m is a constant depending on Δv, σ_p is a constant parameter and $[\boldsymbol{\Delta v} \times]$ is the skew symmetric matrix for the Δv, computed as:

$$[\boldsymbol{\Delta v} \times] = \begin{bmatrix} 0 & -\Delta v(3) & \Delta v(2) \\ \Delta v(3) & 0 & -\Delta v(1) \\ -\Delta v(2) & \Delta v(1) & 0 \end{bmatrix} \tag{3.37}$$

where $\Delta v(1)$, $\Delta v(2)$ and $\Delta v(3)$ are the three components of the vector $\boldsymbol{\Delta v}$.
The P matrix is corrected considering both the 1^{st} and the 2^{nd} burn of the manoeuvre. The first one is needed to move the satellite on the transfer orbit and the second one is needed to return on the nominal orbit.

Chapter 4

ConOps

4.1 Introduction

The previous theoretical digression about the guidance and navigation, respectively, is based on studies which focuses on each of them separately. Therefore, the increase in the degree of autonomy of a satellite is related to the link between the two disciplines, and this can be represented through an appropriate "Concept of Operations" (ConOps).
The objective of the ConOps is to capture the results of the conceptual analysis process, during which, the characteristics of the proposed system (from the user's perspective) and the operational environment in which it needs to work are identified. Both of these aspects, the system's functionality and its operational environment, are equally important.
The proposed mission is an inspection mission around a known target, Envisat, located on a circular polar low Earth orbit and, first of all, considered as a no tumbling object, while in a second analysis a fixed angular velocity will be assumed. The main goal of this mission is to maximize the inspection time, during which acquisition of images and other operations take place. The mission is composed by three main phases:

- *filter phase*, during which the satellite will acquire measurements about its position with respect to the target and process the information filtering with UKF, described in Sect. 3.2, to recover the exact state position;
- *manoeuvre phase*, during which the on-board computer will compute the optimal trajectory, described in Sect. 2.4.2, to re-position the satellite on the nominal orbit, after its drifting due to nonlinear effects and/or perturbations;
- *inspection phase*, during which the satellite acquires images of target and does other scientific tasks.

Figure 4.1: ConOps

Therefore, the time of the mission will be divided correspondingly as follow:

- Δt_{fil}: time dedicated to the estimation of the satellite state position with respect to the target;
- Δt_{man}: time dedicated to perform the optimal manoeuvre computed by the on-board processor;
- Δt_{insp}: time dedicated to the acquisition of images and other operations.

During the manoeuvre and the inspection, the acquisition of measurements is not possible and the estimation of the real state of the deputy is given simply using the GUT, described in Sect. 3.5, assuming that this is the only information about its position with respect to the target. In this way, the satellite is completely autonomous from the point of view of the knowledge of its state, leading to an algorithm which is completely free from the communications with ground. The total time of the mission has been fixed to one day (just over 14 orbits) of mission around the target, easy to compare with other missions also in terms of fuel consumption and inspection quality. In fact, from the measurements given by one day of simulation, estimated values related to longer time simulation, as weeks, months or years, may be proposed. Since the main goal of this treatment is to maximize the inspection phase, different strategy have been analyzed, also to guarantee a good quality of inspection, with a favourable position to acquire images.

Strategy A

First of all, the simplest case (A1), in which all the three phases are fixed, is shown. The time for each of the phases has been chosen arbitrarily, dividing the period of two orbits in three parts: one orbit for the filter, half orbit for the manoeuvre and half orbit for the inspection. This strategy will be used as a baseline for the next considerations. Then, the filter phase is analyzed, in order to reduce its time, optimizing the conditions for which it is sufficient to retrieve the real state of the satellite. This will lead to the definition of the minimum time for the UKF to converge to the acquired measurements for the first cycle, and this value has been adopted to update the initial strategy (A2).

Strategy B

Some further conditions will be imposed to reduce the successive filter phases, in order to reduce the fixed time found, and leading to the second strategy, in which the filter phase will have a variable time (B1), accordingly to the imposed conditions. Now, the time for the filtering will be minimum and the analysis can go on with the manoeuvre phase. In particular, starting from the dynamical models validation, an investigation of the best ToF_M has been performed, and then this results has been inserted into the algorithm, generating a further strategy (B2).

Strategy C

In this third strategy (C1), the introduction of a new minimization problem will lead to the optimization of both the cost of the manoeuvre and the ToF_M needed (introduced also in the Sect. 2.4.2), guaranteeing, once again, the reduction of the manoeuvring time.

Strategy D

Now, the inspection phase is analyzed. New conditions will be introduced to increase or reduce the time for the inspection based on the position of the satellite along the orbit and with respect to the target. This will lead to a completely autonomous algorithm (D1) that will vary the time of the phases according to the position of the deputy with respect to the target.

Strategy E

In conclusion, in this final strategy, the constraint due to an unique nominal orbit is removed, and the treatment will go towards a new inspection strategy concept, aimed at linking the algorithm with the quality and the improvement of the inspection phase assuming a set of inclined football orbits, which will be the "instrument" adopted to optimize this aspect and try to assure that all the faces of the target will be seen by the camera of the deputy for the necessary time.

4.2 Score

The chosen development of the thesis lead to the need of the description of the main purposes: if in the guidance part the goal is to minimize the fuel consumption and the ToF_M, on the other hand, in the navigation part, the goal is to correctly estimate the position of the deputy with respect to the target, as close as possible to the real trajectory. According to this differentiation, various aspects of the mission will be analyzed, in order to defined the best strategy in terms of a trade off of them.
The parameters taken into account are listed below.

- *Inspection time*: both the absolute and relative time in terms of percentage with respect to the total simulation time, that has been assumed as one day (about 14 orbits) will be considered. From these values, the aim is to understand how important is the inspection phase during the mission and how varies with the different strategies.

- *Manoeuvre cost*: it is represented by two terms. The first one is given by the total Δv used for each strategy and, along the improvements of the strategies themselves, this parameter should be decreased. The second is due to the satisfaction of the boundary constraints related to each component of each manoeuvre burn of each strategy. In other words, the analysis is focused on the value of the Δv component, comparing between them and, in addition, the limits of actual technology on propulsion systems suitable for Cubesats and small satellites must be taken into account;

- *Inspection quality*: it is supplied by the visibility time for each faces of the target during the inspection phase. A relevant detail concerns the choice of the sensor adopted, because each device is affected by different parameters and each of them can be suitable for different mission cases. For this mission case, a camera has been selected and it is characterized by a certain Field of View (FoV), necessary to guarantee the acquisition of high resolution images in a determined time interval.

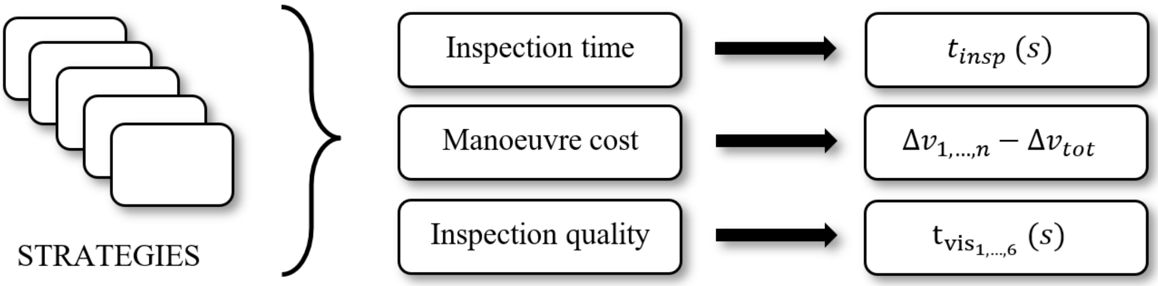

Figure 4.2: Score methodology

4.3 Initial conditions

4.3.1 Target's orbit parameters

As it has already been said, Envisat has been chosen as the target of this inspection mission analysis. Its mission, starting in 2002, ended in 2012, after the unexpected loss of contact with the satellite. It means that, knowing its position and its structure (so, it can be defined as *known object*), it is no longer controllable and every mission around this satellite shall be performed considering it as *uncooperative object*. Moreover, there is no information about its attitude. Following this contextualization, this thesis provides a set of initial conditions, both for fixed attitude (no angular velocity acts on the body) and for tumbling case.
Envisat is in a LEO, so from [1], its initial position can be defined adopting a set of Keplerian Elements, that are listed in Tab. 4.1:

Parameter	Value
a [km]	7142
e [-]	0.001272
i [deg]	98.2009
Ω [deg]	278.7771
ω [deg]	89.4215

Table 4.1: Target's orbital elements

The eccentricity of the orbit will be neglected due to the fact that the dynamical models are more suitable for a circular orbit (e = 0). From these, some parameters can be computed, as:

$$T = \sqrt{\frac{\mu}{r_c^3}} = 6006\,[s] \qquad\qquad n = \frac{2\pi}{T} = 0.001\left[\frac{1}{s}\right] \tag{4.1}$$

where T is the period of the orbit and n is the mean motion.
Moreover, the initial conditions of the relative states for the fixed and tumbling configurations are reported, respectively, in Tabs. 4.2 and 4.3.

---

[1] `https://www.n2yo.com/satellite/?s=27386`

Rotational Dynamics	
ϕ (rad)	0.26
θ (rad)	0.37
ψ (rad)	0.58
$\omega_{r,x}$ (rad/s)	0
$\omega_{r,y}$ (rad/s)	0
$\omega_{r,z}$ (rad/s)	0

Table 4.2: Target's initial dynamics in fixed configuration

In the tumbling case, the attitude is initialized randomly, whereas the angular velocity is selected in order to have an absolute value of about 2.5 deg/s, as in [23].

Rotational Dynamics	
ϕ (rad)	1.66
θ (rad)	2.27
ψ (rad)	-0.38
$\omega_{r,x}$ (rad/s)	0.02
$\omega_{r,y}$ (rad/s)	0.02
$\omega_{r,z}$ (rad/s)	0.04

Table 4.3: Target's initial dynamics in tumbling configuration

4.3.2 Deputy's orbit parameters

The initial state has been chosen in according to the size and shape of Envisat. In fact, in order to avoid to collide with the target, the deputy shall stay at a certain distance. Fixing a *Keep Out Zone* (KOZ) of radius equal to 30 m, the relative orbit has been selected in such a way to have at least a minimum distance from target's center of gravity equal to the double of the KOZ radius itself.

Translational Dynamics	
x (m)	65
y (m)	0
z (m)	0
$\dot{x}$ (m/s)	0
$\dot{y}$ (m/s)	-0.13
$\dot{z}$ (m/s)	0

Table 4.4: Deputy's initial state on the relative orbit

4.3.3 Deputy's satellite parameters

Unlike before, the attitude of the deputy and its control is not the main topic in this treatment and it has been neglected, focusing more on the guidance and navigation part. For this reason, the description of the entire satellite structure is not relevant, skipping directly on the propulsion system, that gives the information about the range of thrust, so how much Δv the propulsion system can offer. Due to the choice of adopting impulsive manoeuvres, a limiting maximum value have been assumed, listed in Tab. 4.5:

Parameter	Value
Δv_{max}	100 mm/s

Table 4.5: Values of deputy's properties applied in the simulation

4.3.4 Filter initialization

The initial parameters for the UKF are selected as follows:

$$\boldsymbol{P}_0 = \begin{bmatrix} 10^{-3} \cdot \boldsymbol{I}_3 & \mathbf{0}_{3x3} \\ \mathbf{0}_{3x3} & 10^{-6} \cdot \boldsymbol{I}_3 \end{bmatrix} \tag{4.2}$$

$$\boldsymbol{R} = \begin{bmatrix} 10^{-3} \cdot \boldsymbol{I}_6 \end{bmatrix} \tag{4.3}$$

where $\boldsymbol{P_0}$ is the initial covariance matrix for the state, $\boldsymbol{R}$ is the measurements noise matrix and $\boldsymbol{Q}$ is the process noise matrix, which will be neglected in this treatment.
As the measurements are taken from the simulator environment, some noises are added, to simulate the sensibility of the camera, which is characterized by a field of view.

Error Noises & FOV					
σ_{pos}^{f} (m)	10^{-1}	σ_{vel}^{f} (m/s)	10^{-3}	FOV (deg)	15

Table 4.6: Error noises and FOV of the camera

4.4 Dynamical models validation

Starting from Sect. 2.5, the models validation is needed to know how they vary in time, in order to ease the transition to a more autonomous configuration. This idea allows also to understand the behaviour of the different dynamical models in such a way to identify the best operative time frame and avoid reaching some critical conditions. The following analysis has been anticipated in the previous paragraph, where filter conditions have been set to optimize the closed loop algorithm, and it will be relevant to other parts that will be exposed in the next chapters. Excluding the 2BP model due to its inactivity in these thesis sections, the comparison will show the differences between linear and nonlinear relative dynamics, highlighting in particular the behaviours among:

- HCW - NERM
- HCW - perturbed NERM

Let's assume the initial conditions of Tab. 4.4 and introduce two covariance matrices to vary the initial conditions. In fact, unlike the Sect. 2.5, this analysis has been focused on the behaviour of these dynamical models outside the stationary conditions, to emulate situations verifiable also in the simulations.

$$\boldsymbol{P}_0 = \begin{bmatrix} 10^{-3} \cdot \boldsymbol{I}_3 & \mathbf{0}_{3x3} \\ \mathbf{0}_{3x3} & 10^{-6} \cdot \boldsymbol{I}_3 \end{bmatrix} \tag{4.4}$$

$$\boldsymbol{P}_{dirty} = \begin{bmatrix} 10^{-5} \cdot \boldsymbol{I}_3 & \boldsymbol{0}_{3x3} \\ \boldsymbol{0}_{3x3} & 10^{-7} \cdot \boldsymbol{I}_3 \end{bmatrix} \tag{4.5}$$

The first one is the initial covariance matrix fixed also in all the strategies, meanwhile P_{dirty} has the purpose of varying the P_0, that will vary the initial state vector. This idea has been developed in such a way to obtain 50 different initial states, associated with 50 different initial covariance matrices, obtaining 2500 different combinations of mean, that will be used in the following step. In fact, considering each combination, the aim is always the same: to understand how much the error between the dynamical models diverges. In order to perform that, a value has been assumed as limit error to analyze how much time is necessary to reach it. In this case, the threshold is equal to 5 m. So, the following results show the time spent to achieve this limit value for each combination, characterized by its mean and covariance.
For the unperturbed case, shown in Fig. 4.3, the average value is 985 s and only 944 over 2500 values exceed it (about 37.76 % of the total data), meanwhile the minimum value computed is equal to 380 s and the maximum is 10626 s. In addition to the data previous written, Fig. 4.3 shows how the results of each combination assume a determined trend remaining in a low time range in the most of the cases, except for some outliers.

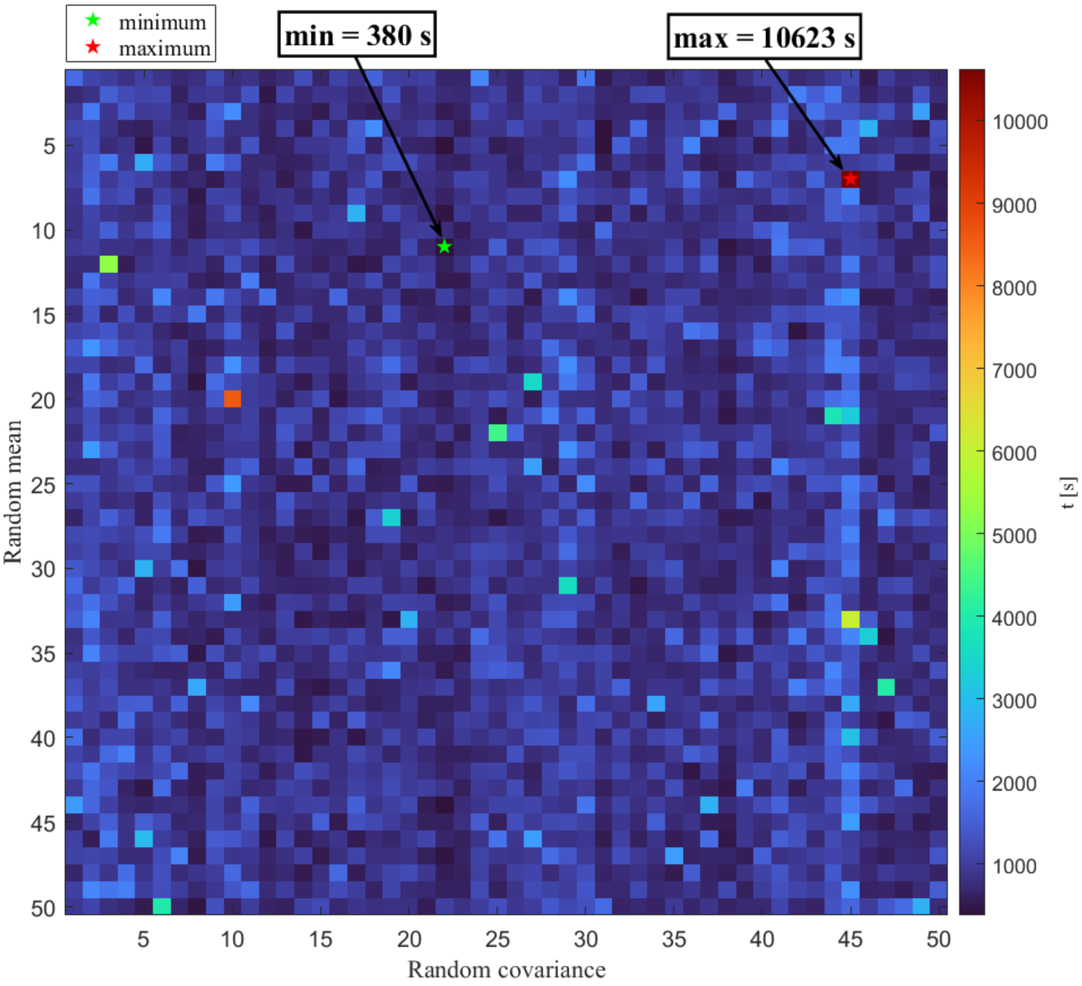

Figure 4.3: NP - time needed to arrive at the desired error for each sample

For the perturbed case, the average value is 785 s and only 1021 over 2500 values exceed it (about 40.84 % of total data), meanwhile the minimum value computed is equal to 338 s and the maximum is 2697 s. Unlike Fig. 4.3, the results seem more homogeneous than the previous case, laying always in the low time range. Some high peaks are present but, obviously, they are not comparable to the value produced in the previous analysis.

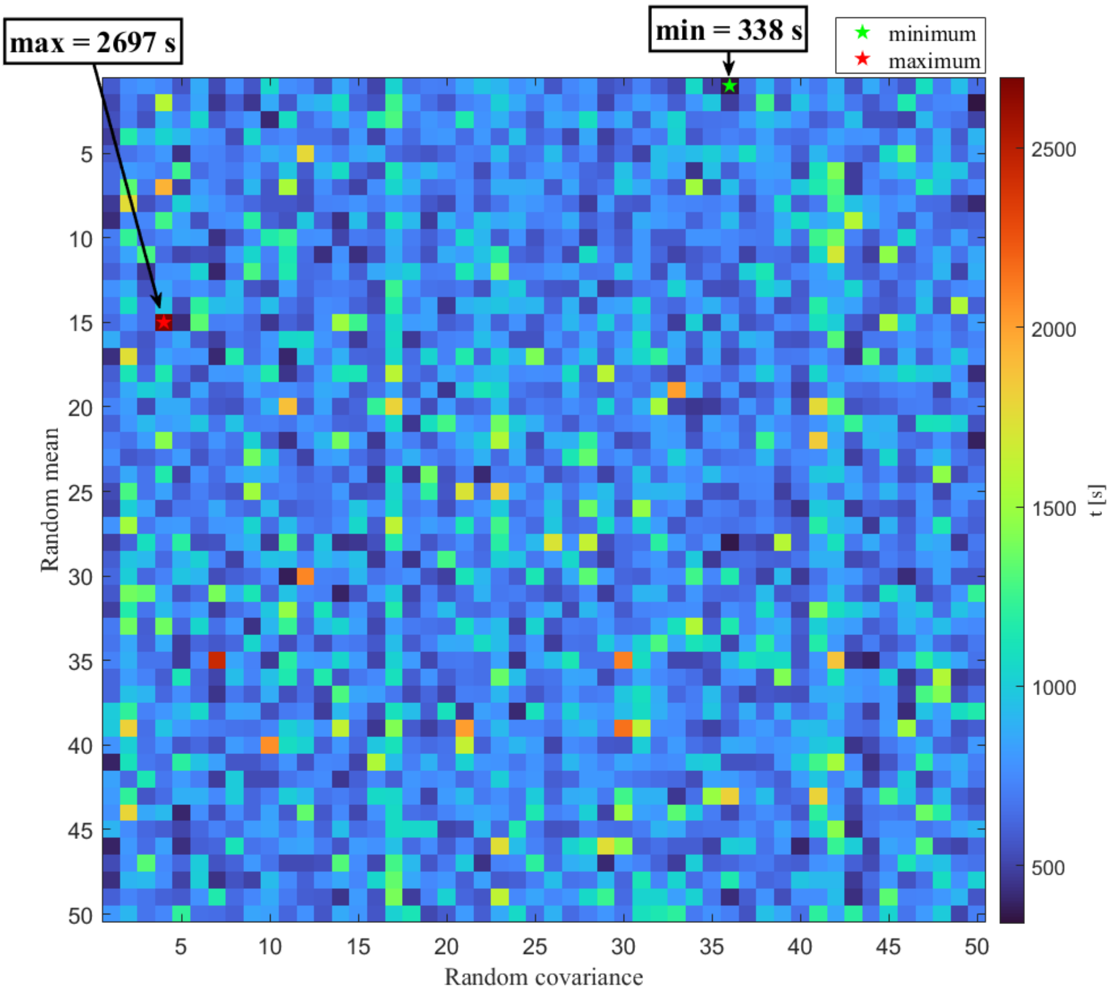

Figure 4.4: P - time needed to arrive at the desired error for each sample

Chapter 5

Results

5.1 Unperturbed case

In this chapter, the results of the simulation with the external dynamics represented by the unperturbed NERM and the on-board dynamics represented by the HCW are exposed.

5.1.1 Strategy A1

This first strategy considers all the phases with a fixed time. In particular, the filter phase has been fixed to one orbit period time in order to wait for the convergence of the UKF. Then, the manoeuvre and the inspection phases have been fixed to half orbit period time, arbitrarily. This strategy will be used as a baseline for every next strategy. Moreover, this will help to simplify the algorithm and to understand better the behaviour of the covariance and the error during the mission.
The specific time for each phases are listed in Tab. 5.1.

Parameter	Value
Δt_{fil} (s)	6007
Δt_{man} (s)	3003
Δt_{insp} (s)	3003

Table 5.1: NP - Strategy A1: values of time intervals

The behaviour of the covariance is shown in Figs. 5.1 and 5.2. The color of the region indicates the different phases: blue for the filter phase, red for the manoeuvre phase and green for the inspection phase.
As it can be noticed, in the first cycle, the covariance tends to grow more than in the others cycles. This is due to the corrective term exposed in Sect. 3.5.1: in fact, the more expensive the manoeuvre is, the more important this addictive term is. In this case, the first impulse is too high, leading to an extremely high increase of the covariance during the manoeuvre. This will result in a further growing of the covariance in the inspection phase, which is given by the second impulse of the manoeuvre.

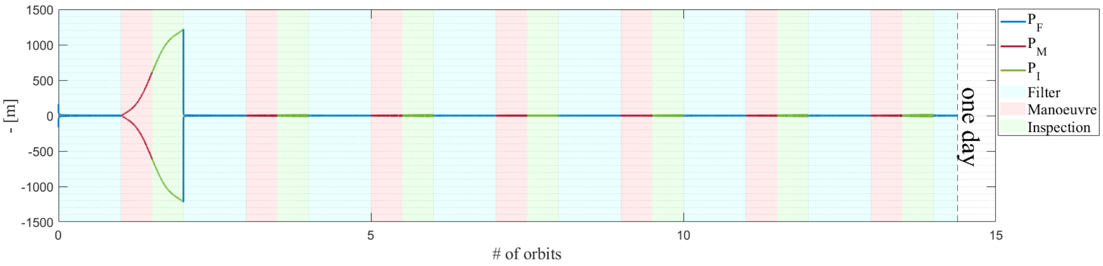

Figure 5.1: NP - Strategy A1: behaviour of the covariance

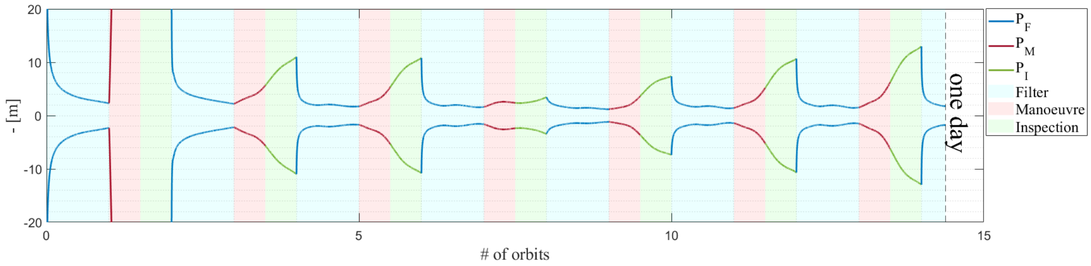

Figure 5.2: NP - Strategy A1: behaviour of the covariance (zoom)

Moreover, the behaviour of the error is shown in Fig. 5.3. Specifically, the error is defined as the difference between the "real" state given by the NERM propagation and the "estimated" state, given by the UKF in the filter phase and the GUT in the manoeuvre and the inspection phases. In the filter phase, the error correctly remains in the limits for most of the cases, except for the fifth cycle. This divergence can be due to the fact that the initial covariance, coming from the GUT of the previous inspection phase, is already not mapping correctly the state. In fact, as it can be seen, the error along the y-axis is already out of the covariance limits starting from the manoeuvre.

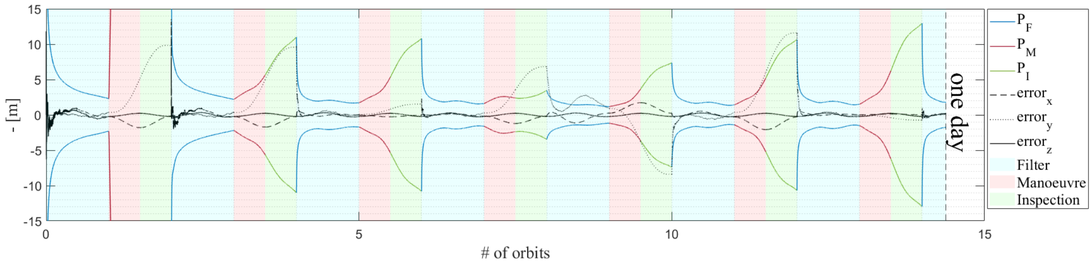

Figure 5.3: NP - Strategy A1: behaviour of the error (zoom)

The cost for each of the manoeuvre is reported in Tab. 5.2, considering the sum of the two impulses. Again, the first manoeuvre is clearly too high, in the order of m/s, while the other ones are in the order of cm/s or mm/s.

Manoeuvre (#)	Δv_x (cm/s)	Δv_y (cm/s)	Δv_z (cm/s)	$\lvert\Delta v\rvert$ (cm/s)
1	$5.3 \cdot 10^{-2}$	$1 \cdot 10^{-2}$	$1.2 \cdot 10^{2}$	$1.2 \cdot 10^{2}$
2	$9.6 \cdot 10^{-1}$	$5.3 \cdot 10^{-2}$	$8.1 \cdot 10^{-2}$	$9.7 \cdot 10^{-1}$
3	$1 \cdot 10^{0}$	$5.2 \cdot 10^{-2}$	$3.1 \cdot 10^{-2}$	$1 \cdot 10^{0}$
4	$1.2 \cdot 10^{-1}$	$1.4 \cdot 10^{-2}$	$2.2 \cdot 10^{-2}$	$1.3 \cdot 10^{-1}$
5	$7 \cdot 10^{-1}$	$3 \cdot 10^{-2}$	$1.5 \cdot 10^{-2}$	$7 \cdot 10^{-1}$
6	$1 \cdot 10^{0}$	$5.4 \cdot 10^{-2}$	$1.3 \cdot 10^{-2}$	$1 \cdot 10^{0}$
7	$1.2 \cdot 10^{0}$	$6.5 \cdot 10^{-2}$	$1.9 \cdot 10^{-2}$	$1.2 \cdot 10^{0}$

Table 5.2: NP - Strategy A1: Δv values

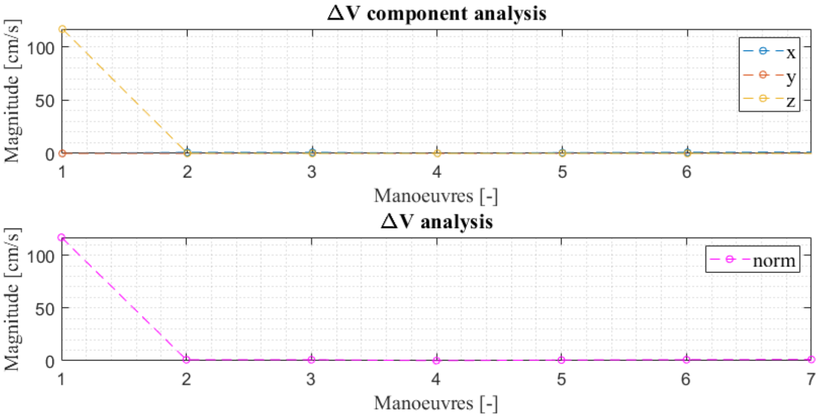

Figure 5.4: NP - Strategy A1: behaviour of Δv

Finally, the percentage of time spent for each of the phases for a mission of exactly one day has been computed. For this strategy, as shown in Fig. 5.5, the percentage of the inspection will be 24%, as expected from the fixed time imposed.

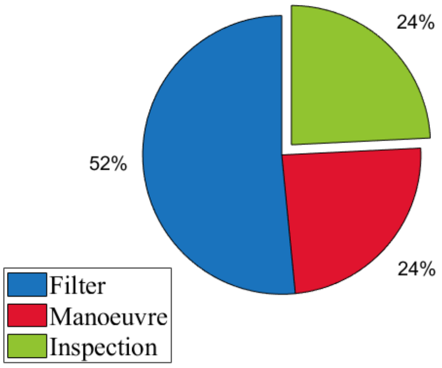

Figure 5.5: NP - Strategy A1: percentage of phases

5.1.2 Filter analysis 1/2

In order to optimize the phase time of the filter, a first analysis has been carried out. In fact, as it can be noticed, the UKF reaches the convergence long before one period orbit, so the time of this phase can be reduced. First of all, the conditions for the convergence must be defined in according to the final values computed at the end of one period orbit. Then, a Monte Carlo analysis has been performed on 1000 random samples lying inside the initial covariance and the resulting delay times is shown in Fig. 5.6. In the graph, it can be noticed that:

- the error between the position state vector of the NERM and the one coming from the UKF tends to stabilize before one orbit (6007 s). Since the error behaviour is not smooth, the final value of it has been used as mean to build a convergence band (green region);
- the size of the covariance matrix coming from the UKF decreases during the time, reaching an area where the trend starts to stabilize;

Vertical red lines indicate the time delay for each samples, in this case always the same, for different size of the covariance. As it can be seen, to reach a size of 3 m of covariance, 3970 s are needed, and the corresponding error stays in the convergence band. This value is the minimum time for which the error in contained in the band, and, since the aim of this analysis is to reduce the filter time to the minimum, this will be selected. Other values have been excluded either for the dissatisfaction of the error condition (out of the band) either for the value of time which is higher than the minimum considered and closer to the one fixed before.

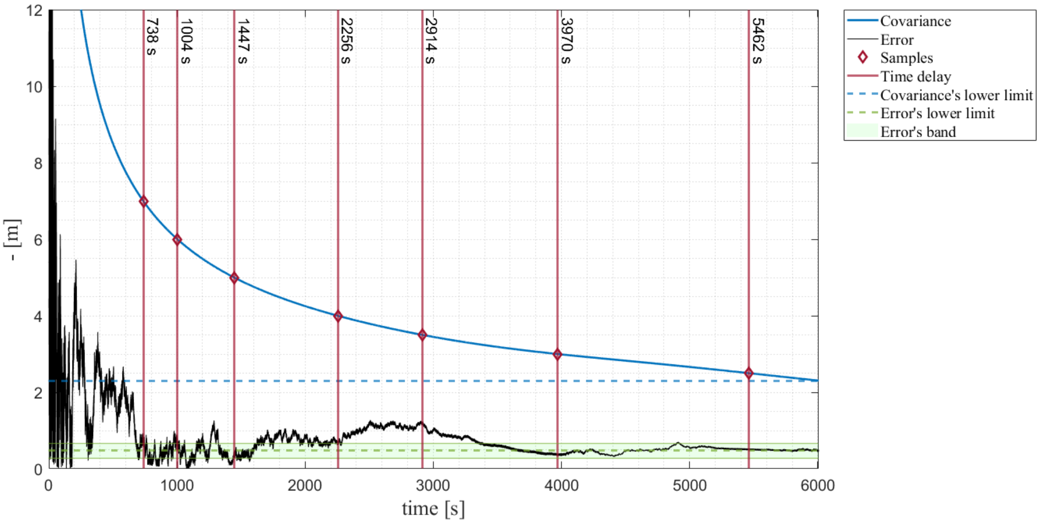

Figure 5.6: NP - Delay time for each sample

The value of time selected has been set for the filter phase in the strategy A2, in such a way to reduce the overall filter time, earning about 33% of time.

5.1.3 Strategy A2

In this strategy, the time of the phases used are reported in Tab. 5.3:

Parameter	Value
Δt_{fil} (s)	3970
Δt_{man} (s)	3003
Δt_{insp} (s)	3003

Table 5.3: NP - Strategy A2: values of time intervals

The behaviour of the covariance is shown in Fig. 5.7. Also in this case, the covariance reaches a size which is too high, leading to an higher uncertainties of the state of the satellite. Moreover, the high increase of the covariance in the first cycle is still there, confirming the previous statement for which that increasing is due to the high manoeuvre.

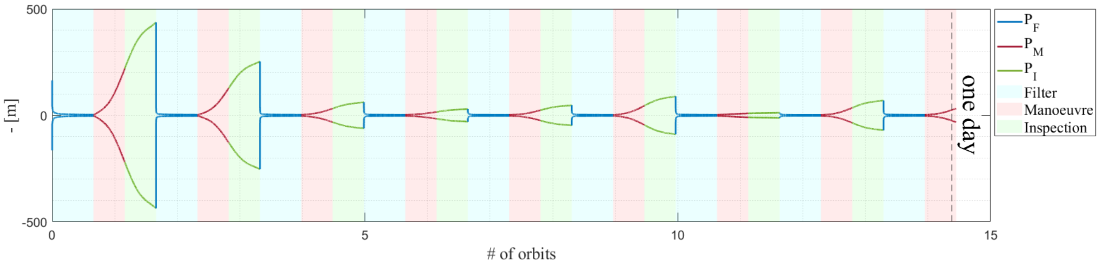

Figure 5.7: NP - Strategy A2: behaviour of the covariance

On the other hand, the behaviour of the error is shown in Fig. 5.8. Now, all the components of the error between the "real" state and the "estimated" one remains in the limits. Also, the filter always converges, demonstrating the previous analysis.

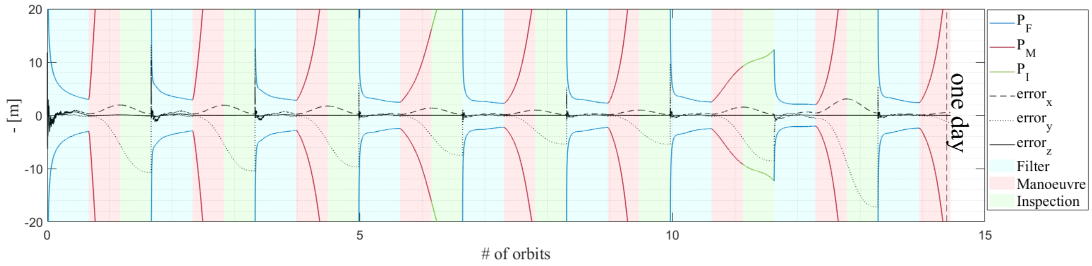

Figure 5.8: NP - Strategy A2: behaviour of the error (zoom)

The cost in terms of Δv for each of the manoeuvre is listed in Tab. 5.4. Again, the first manoeuvre is too expensive even if the order of magnitude is one lower with respect to the previous one, as Tab. 5.2 shows. In addition, also the second manoeuvre is too high and this will lead to a greater covariance.

Observing the values of the single components, another detail to highlight is the fact that the order of magnitude of the norm of the Δv is affected mostly by the contribution of the z-axis component. This can be explained considering that the nominal orbit is constrained to lay on xy-plane and then, the z-component of the position state must be null: any noise or disturbance due to the filter or measurements leads a displacement from the xy-plane, causing an inevitably high impulse on the z-axis.

Manoeuvre (#)	Δv_x (cm/s)	Δv_y (cm/s)	Δv_z (cm/s)	$\lvert\Delta v\rvert$ (cm/s)
1	$3.6 \cdot 10^{-2}$	$1.4 \cdot 10^{-2}$	$4.2 \cdot 10^{1}$	$4.2 \cdot 10^{1}$
2	$1.1 \cdot 10^{0}$	$5.8 \cdot 10^{-2}$	$2.4 \cdot 10^{1}$	$2.4 \cdot 10^{1}$
3	$1.1 \cdot 10^{0}$	$5.7 \cdot 10^{-2}$	$5.7 \cdot 10^{0}$	$5.8 \cdot 10^{0}$
4	$9.9 \cdot 10^{-1}$	$5.5 \cdot 10^{-2}$	$2.6 \cdot 10^{0}$	$2.8 \cdot 10^{0}$
5	$7.7 \cdot 10^{-1}$	$4.4 \cdot 10^{-2}$	$4.4 \cdot 10^{0}$	$4.5 \cdot 10^{0}$
6	$5.5 \cdot 10^{-1}$	$3.2 \cdot 10^{-2}$	$8.5 \cdot 10^{0}$	$8.5 \cdot 10^{0}$
7	$5.4 \cdot 10^{-1}$	$3 \cdot 10^{-2}$	$6.3 \cdot 10^{-1}$	$8.3 \cdot 10^{-1}$
8	$8.2 \cdot 10^{-1}$	$4.4 \cdot 10^{-2}$	$6.7 \cdot 10^{0}$	$6.7 \cdot 10^{0}$
9	$1.8 \cdot 10^{0}$	$9.8 \cdot 10^{-2}$	$5.8 \cdot 10^{0}$	$6.1 \cdot 10^{0}$

Table 5.4: NP - Strategy A2: Δv values

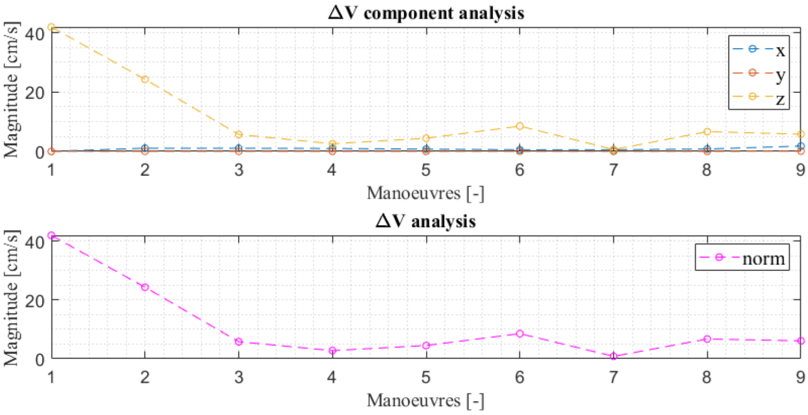

Figure 5.9: NP - Strategy A2: behaviour of Δv

The percentage of inspection is increased to 28%, due to the reduction of the filter phase.

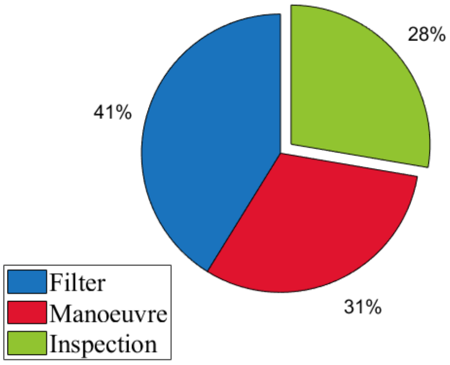

Figure 5.10: NP - Strategy A2: percentage of the phases

5.1.4 Filter analysis 2/2

Assuming that the filter needs some time to set only in the first cycle, so at the beginning of the mission, the filter phase time can be further reduced. In particular, the fixed time found in the previous analysis will be maintained for the first cycle and for the next cycles, some other conditions are introduced, in order to make more flexible the filter phase, such that the time spent will be the minimum time needed to estimate the state position vector of the deputy:

- *minimum phase time*: for the first cycle, the minimum value of time for the convergence of the filter found in the previous analysis has been kept;
- *error between UKF and nominal orbit*: when the deputy's estimated state from the UKF is way too far from the nominal trajectory given by the HCW, the filter phase will be stopped and a station keeping manoeuvre will be performed to re-position the deputy on the nominal orbit. In this case, an error of 5 m has been chosen to keep the cost of the manoeuvre under the limits of a real propulsion system and as a consequence of the validation of the models, described in Sect. 4.4;
- *maximum size of the covariance*: the covariance size has been limited to 3 m, which is the condition for the convergence of the filter considered in the previous filter analysis, in Sect. 5.1.2;
- *divergence control*: the mean coming from the UKF must be contained inside the associated covariance. In this way, any diverging behaviour of the filter can be suppressed.

5.1.5 Strategy B1

This new strategy will use a variable filter, which will stop according to the conditions imposed in Sect. 5.1.4, while the manoeuvre and inspection phase time will remain fixed, as listed in Tab. 5.5:

Parameter	Value
$\Delta t_{fil,1}$ (s)	3970
Δt_{fil} (s)	*variable*
Δt_{man} (s)	3003
Δt_{insp} (s)	3003

Table 5.5: NP - Strategy B1: values of time intervals

The behaviour of the covariance is shown in Fig. 5.11. Also in this case, the covariance increases too much in all the cases, due to the manoeuvre phase, suggesting that an analysis on it is necessary.

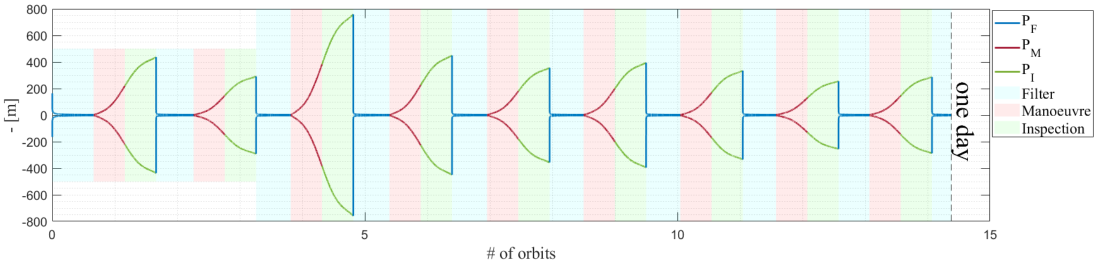

Figure 5.11: NP - Strategy B1: behaviour of the covariance

The behaviour of the error is shown in Fig. 5.12. As it can be seen, the error is always included in the limits, and the filter always correctly converges.

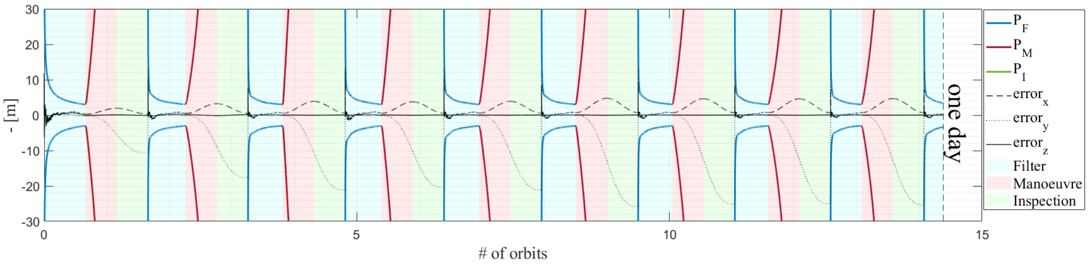

Figure 5.12: NP - Strategy B1: behaviour of the error (zoom)

The filter phase time is now variable, but the values changes only by few seconds, as shows Tab. 5.6.

Cycle	1	2	3	4	5	6	7	8	9
Δt_{fil} (s)	3970	3600	3330	3483	3370	3266	3284	3194	1879

Table 5.6: NP - Strategy B1: filter phase times

As it can be seen from Fig. 5.13, a little improvement on the inspection time has been obtained overall with a 31% against the 28% of before.

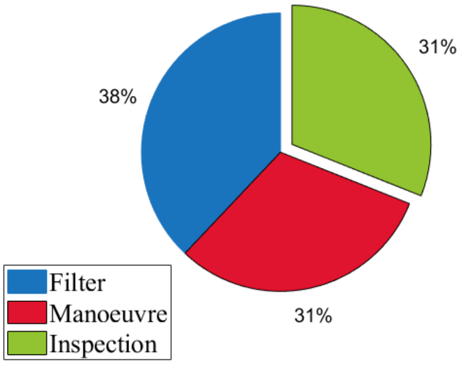

Figure 5.13: NP - Strategy B1: percentage of the phases

The values of the Δv for the manoeuvre are listed in Tab. 5.7. Again, the z-component influences the most the total impulse. In fact, all the manoeuvres exceed the value of 10 cm/s, which is too high, and will cause a great increase in the covariance's sizes, leading to a further increase during the inspection phase.

Manoeuvre (#)	Δv_x (cm/s)	Δv_y (cm/s)	Δv_z (cm/s)	$\lvert\Delta v\rvert$ (cm/s)
1	$3.6 \cdot 10^{-2}$	$1.4 \cdot 10^{-2}$	$4.2 \cdot 10^{1}$	$4.2 \cdot 10^{1}$
2	$1 \cdot 10^{0}$	$5.2 \cdot 10^{-2}$	$2.8 \cdot 10^{1}$	$2.8 \cdot 10^{1}$
3	$1.7 \cdot 10^{0}$	$8.7 \cdot 10^{-2}$	$7.3 \cdot 10^{1}$	$7.3 \cdot 10^{1}$
4	$2.1 \cdot 10^{0}$	$1.1 \cdot 10^{-1}$	$4.3 \cdot 10^{1}$	$4.3 \cdot 10^{1}$
5	$2 \cdot 10^{0}$	$1 \cdot 10^{-1}$	$3.4 \cdot 10^{1}$	$3.4 \cdot 10^{1}$
6	$2 \cdot 10^{0}$	$1 \cdot 10^{-1}$	$3.8 \cdot 10^{1}$	$3.8 \cdot 10^{1}$
7	$2.5 \cdot 10^{0}$	$1.3 \cdot 10^{-1}$	$3.2 \cdot 10^{1}$	$3.2 \cdot 10^{1}$
8	$2.5 \cdot 10^{0}$	$1.2 \cdot 10^{-1}$	$2.4 \cdot 10^{1}$	$2.4 \cdot 10^{1}$
9	$2.4 \cdot 10^{0}$	$1.2 \cdot 10^{-1}$	$2.7 \cdot 10^{1}$	$2.7 \cdot 10^{1}$

Table 5.7: NP - Strategy B1: Δv values

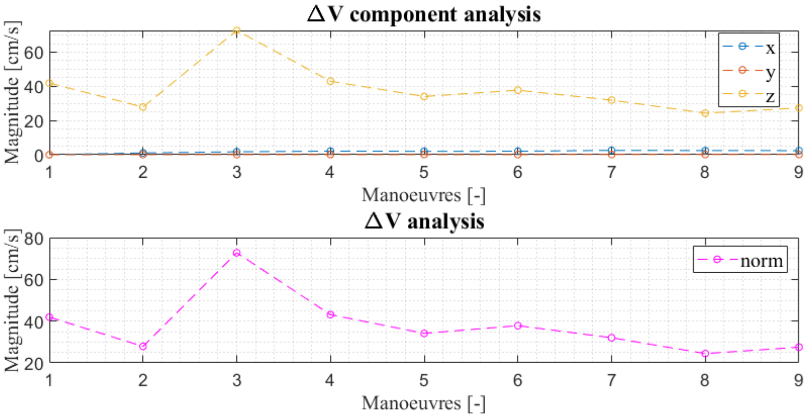

Figure 5.14: NP - Strategy B1: behaviour of Δv

5.1.6 ΔV analysis

Starting from the results of Sect. 4.4, another analysis has been performed. In this case, the aim is to find a suitable manoeuvring time that allows to have:

- good behavior of the covariance;
- low Δv cost.

These parameters should give the opportunity of reducing the fuel consumption, and through the reduction of the manoeuvring time, maximizing the inspection time holding in consideration the same simulation time of one day mission.

To do it, an initial approach consists in collecting the data of Sect. 4.4 and compute the density of each time sample in terms of percentage. The choice of considering this data set for the manoeuvre path is supported by the difference in the propagation itself, between the HCW and the NERM in time. In fact, the dynamical models and their comparison affect also the manoeuvre: usually the "real" initial point of the manoeuvre (given by the NERM) usually does not correspond to the stationary conditions, and unfortunately the "real" final point (again given by the NERM) proves that the deputy does not reach the exact point computed by the on-board software. The error between the dynamics models is a function of:

1. Time of Flight of the manoeuvre;
2. Initial error;
3. Conditions of the final reference orbit, as relative orbit size and shape.

Due to the fact that the second parameter is fixed by the filter condition and the third one is equal to the initial nominal orbit, the only parameter to work with is related to the ToF_M. For these reasons, the previous data set of Fig. 4.3, where the error has been set to 5 m, are still valid.

Moreover, to have a better insight of the density of the data in Fig. 5.15, an interpolating function (20^{th} order) has been extrapolated from them. Then, the median has been evaluated and this value is considered to be the center value of the interval that will be analyzed afterwards. In particular, the size of the interval is chosen in such a way to include the 99% of the data closed to the median. This allows to eliminate some outliers, which are very rare, since the distribution is not uniform, but present a peak around 1000 s. In addition, the interval has been also enlarged to the 99.9%, but as it can be seen from Fig. 5.15, the interval comprehends ToF_M till 6086 s, which is higher than the previous time of half orbit period. To be consistent with the previous fixed time of flight, which was 3003 s, the interval of 99% has been chosen, in order to not go beyond the former one, considering the fact that one of the purpose of this analysis is to reduce the ToF_M.

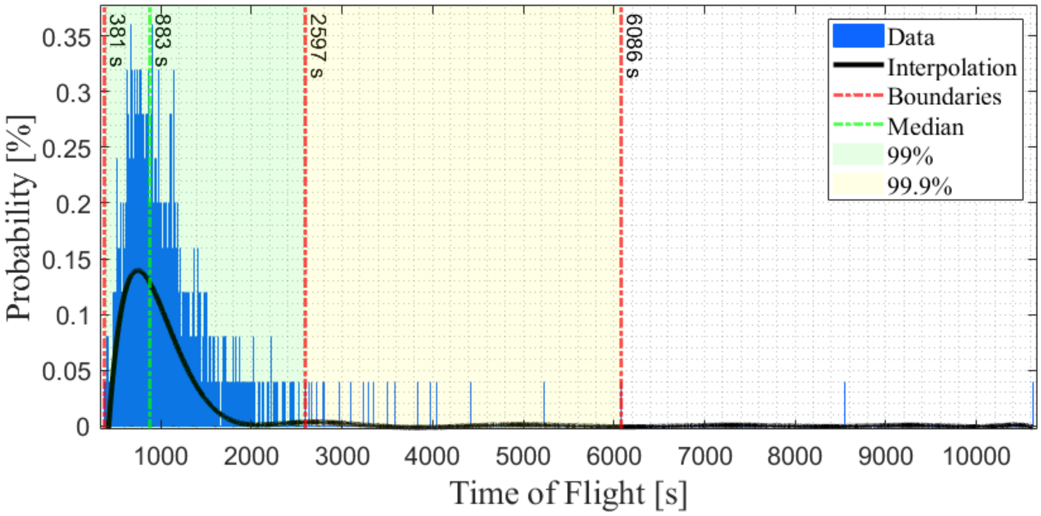

Figure 5.15: NP - Density probability of ToF_M extracted from Sect. 4.4

Consequently, for the case of 99%, the median is 883 s and the lower and upper boundary values are 381 s and 2597 s, respectively. This will reduce the initial interval of time of a nearly 75%.

Now, this interval has been divided into 10 values of ToF_M (boundary values included) and these are used in the simulation algorithm. Using the different times, the corresponding total Δv of the mission (over one day) obtained is shown in Fig. 5.16. Each of the cases has been analyzed to guarantee the satisfaction of the maximum Δv_{tot} and the maximum Δv for every single manoeuvre. As the graph shows, the trend tends to stabilize going towards increasing ToF$_M$. Starting from this consideration, some upper limits have been imposed. The red region indicates the values of Δv_{tot} which are too high compared with the others ($> 35\ cm/s$, where also the behaviour of covariance is not good), while the green region indicates a second interval that will be further analyzed.

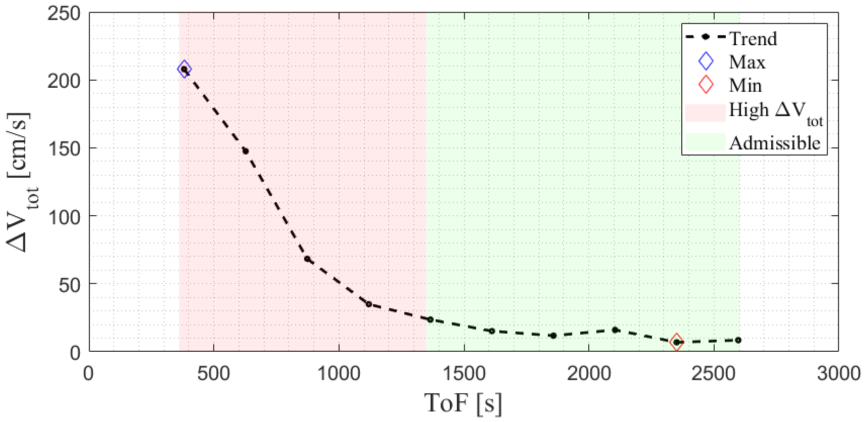

Figure 5.16: NP - Δv_{tot} for the 10 values of ToF$_M$ studied

In particular, the interval from 1350 s to 2600 s has been again divided into 20 values to insert in the simulation and the total cost is shown is Fig. 5.17. Once again, the upper values has been excluded to highlight the minimum values. In the next paragraph, two simulations will be presented among the values of the green region, the one with the minimum Δv_{tot} (1941 s) and the one with the best covariance's behaviour (1744 s).

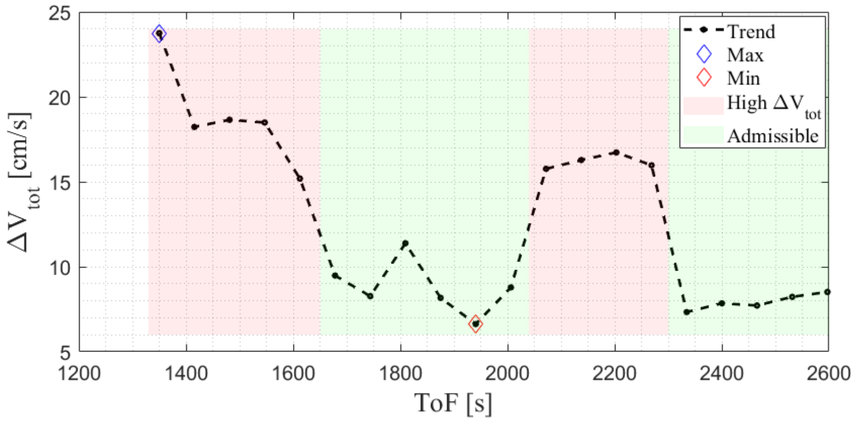

Figure 5.17: NP - Δv_{tot} for the 20 values of ToF$_M$ studied

Figure 5.18: NP - Δv analysis approach

5.1.7 Strategy B2

Minimum Δv_{tot}

Next, the strategy with the minimum Δv_{tot} is presented, and the phase time are listed in Tab. 5.8:

Parameter	Value
$\Delta t_{fil,1}$ (s)	3970
Δt_{fil} (s)	*variable*
Δt_{man} (s)	1941
Δt_{insp} (s)	3003

Table 5.8: NP - Strategy B2: values of time intervals

The behaviour of the covariance is shown in Fig. 5.19. The limit of the size of the covariance remains under 20 m, which is quite a good result if compared with the size of the nominal orbit. In this way, the satellite's estimated position will never reach the target, avoiding a possible collision.

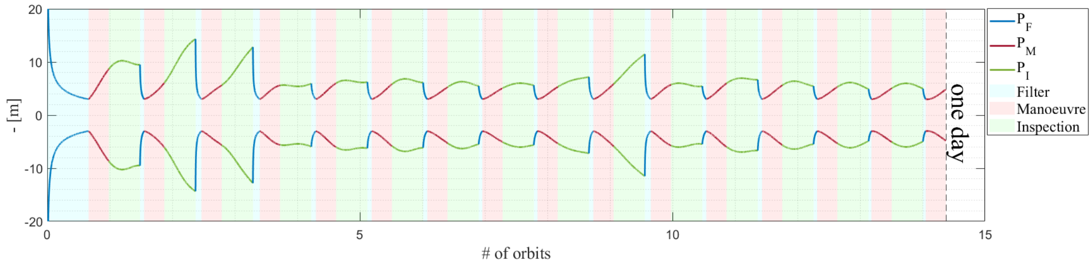

Figure 5.19: NP - Strategy B2: behaviour of the covariance (zoom)

On the other hand, the behaviour of the error is shown in Fig. 5.20, and it can be noticed that all the components of the error are included in the covariance limits, except for the last one, where the y-component is out of the limits. This can be explained considering that the inspection phase time is still fixed to a random value, which is not the best for the mission.

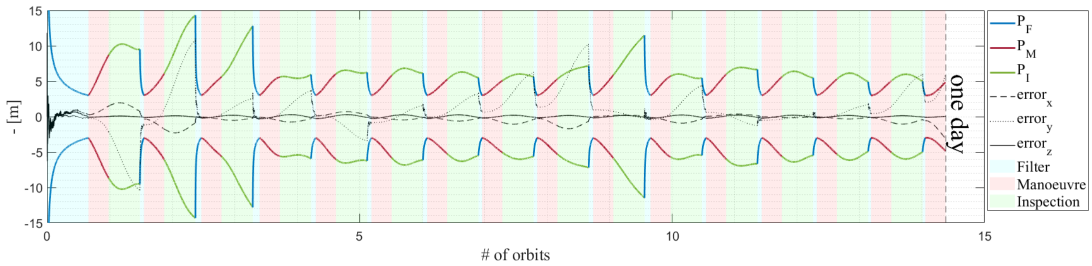

Figure 5.20: NP - Strategy B2: behaviour of the error (zoom)

The Δv values for each of the manoeuvre are listed in Tab. 5.9. All the values are of the order of magnitude of cm/s, as expected from the previous analysis.

Manoeuvre (#)	Δv_x (cm/s)	Δv_y (cm/s)	Δv_z (cm/s)	$\lvert\Delta v\rvert$ (cm/s)
1	$5.5 \cdot 10^{-2}$	$3.4 \cdot 10^{-2}$	$7.3 \cdot 10^{-2}$	$9.7 \cdot 10^{-2}$
2	$1.2 \cdot 10^{0}$	$3.2 \cdot 10^{-1}$	$1.1 \cdot 10^{-2}$	$1.2 \cdot 10^{0}$
3	$1.1 \cdot 10^{0}$	$3.3 \cdot 10^{-1}$	$1.9 \cdot 10^{-2}$	$1.2 \cdot 10^{0}$
4	$2.8 \cdot 10^{-1}$	$7.5 \cdot 10^{-2}$	$2 \cdot 10^{-2}$	$2.9 \cdot 10^{-1}$
5	$3.8 \cdot 10^{-1}$	$1.2 \cdot 10^{-1}$	$1 \cdot 10^{-2}$	$4 \cdot 10^{-1}$
6	$3 \cdot 10^{-1}$	$9.2 \cdot 10^{-2}$	$7.3 \cdot 10^{-3}$	$3.1 \cdot 10^{-1}$
7	$1.7 \cdot 10^{-1}$	$4.8 \cdot 10^{-2}$	$8.5 \cdot 10^{-3}$	$1.8 \cdot 10^{-1}$
8	$2.7 \cdot 10^{-1}$	$7.4 \cdot 10^{-2}$	$1.8 \cdot 10^{-3}$	$2.8 \cdot 10^{-1}$
9	$5 \cdot 10^{-1}$	$1.4 \cdot 10^{-1}$	$2.7 \cdot 10^{-3}$	$5.2 \cdot 10^{-1}$
10	$9.9 \cdot 10^{-1}$	$2.9 \cdot 10^{-1}$	$7.3 \cdot 10^{-3}$	$1 \cdot 10^{0}$
11	$1.1 \cdot 10^{-2}$	$1 \cdot 10^{-2}$	$1.5 \cdot 10^{-2}$	$2.2 \cdot 10^{-2}$
12	$4.3 \cdot 10^{-1}$	$1.3 \cdot 10^{-1}$	$7.2 \cdot 10^{-3}$	$4.5 \cdot 10^{-1}$
13	$9.8 \cdot 10^{-2}$	$3.1 \cdot 10^{-2}$	$6.6 \cdot 10^{-3}$	$1 \cdot 10^{-1}$
14	$3.7 \cdot 10^{-2}$	$9.8 \cdot 10^{-3}$	$1.7 \cdot 10^{-3}$	$3.9 \cdot 10^{-2}$
15	$1.2 \cdot 10^{-1}$	$3 \cdot 10^{-2}$	$2.2 \cdot 10^{-3}$	$1.3 \cdot 10^{-1}$
16	$3.6 \cdot 10^{-1}$	$8.8 \cdot 10^{-2}$	$2.6 \cdot 10^{-3}$	$3.7 \cdot 10^{-1}$

Table 5.9: NP - Strategy B2: Δv values

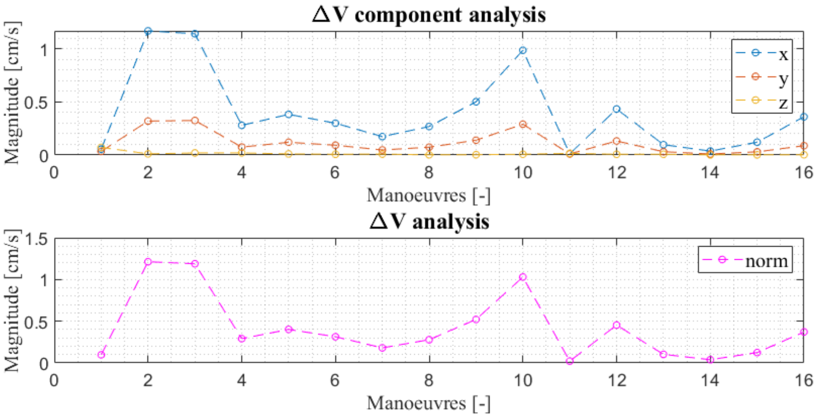

Figure 5.21: NP - Strategy B2: behaviour of Δv

The percentage of the inspection phase time is increased to 52%, as shows Fig. 5.22, thanks to the reduction of the filter phase. The filter phase time values for each cycle are reported in Tab. 5.10. There is a noticeable reduction of time, one order of magnitude lower except for the first fixed cycle. This confirms the advantage of imposing the conditions for the variable filter, described in Sect. 5.1.4

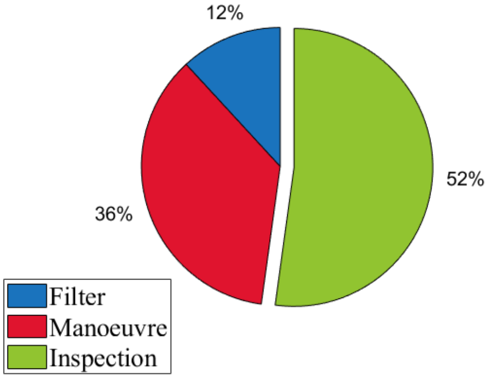

Figure 5.22: NP - Strategy B2: percentage of the phases

Cycle	1	2	3	4	5	6	7	8
Δt_{fil} (s)	3970	390	569	659	447	414	395	350
Cycle	9	10	11	12	13	14	15	16
Δt_{fil} (s)	350	429	575	386	412	347	281	260

Table 5.10: NP - Strategy B2: filter phase times

Best covariance's behaviour

Now, the strategy with the best behaviour of the covariance is presented, and the phase time are listed in Tab. 5.11:

Parameter	Value
$\Delta t_{fil,1}$ (s)	3970
Δt_{fil} (s)	*variable*
Δt_{man} (s)	1744
Δt_{insp} (s)	3003

Table 5.11: NP - Strategy B2: values of time intervals

The behaviour of the covariance is shown in Fig. 5.23. The limits remain under the value of 20 m, which is good as the previous strategy.

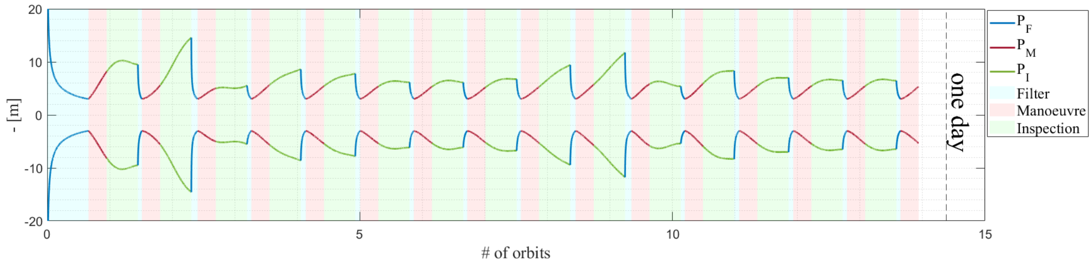

Figure 5.23: NP - Strategy B2: behaviour of the covariance (zoom)

In this case, the error has a better behaviour, leading to a better behaviour also in the inspection phase. In fact, the y-component of the error comes out of the limits only in the inspection phase, while the manoeuvre phase is quite good, as Fig. 5.24 shows.

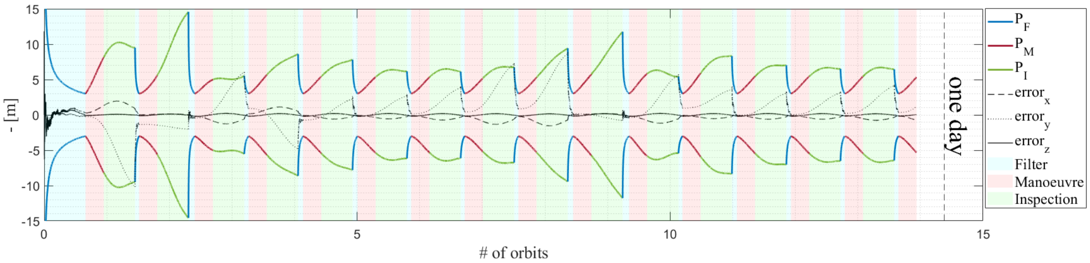

Figure 5.24: NP - Strategy B2: behaviour of the error (zoom)

The values of the Δv values for each of the manoeuvre are reported in Tab. 5.12. Again, all the values stays under the order of magnitude of cm/s, confirming the previous Δv analysis.

Manoeuvre (#)	Δv_x (cm/s)	Δv_y (cm/s)	Δv_z (cm/s)	$\lvert\Delta v\rvert$ (cm/s)
1	$5.8 \cdot 10^{-2}$	$3.9 \cdot 10^{-2}$	$7.4 \cdot 10^{-2}$	$1 \cdot 10^{-1}$
2	$1.2 \cdot 10^{0}$	$4.1 \cdot 10^{-1}$	$1.1 \cdot 10^{-2}$	$1.3 \cdot 10^{0}$
3	$2 \cdot 10^{-1}$	$8.3 \cdot 10^{-2}$	$2.1 \cdot 10^{-2}$	$2.2 \cdot 10^{-1}$
4	$6.8 \cdot 10^{-1}$	$2.7 \cdot 10^{-1}$	$6.7 \cdot 10^{-3}$	$7.3 \cdot 10^{-1}$
5	$5.3 \cdot 10^{-1}$	$2.1 \cdot 10^{-1}$	$1 \cdot 10^{-2}$	$5.7 \cdot 10^{-1}$
6	$2.9 \cdot 10^{-1}$	$1.1 \cdot 10^{-1}$	$9.9 \cdot 10^{-3}$	$3.1 \cdot 10^{-1}$
7	$3.1 \cdot 10^{-1}$	$1.1 \cdot 10^{-1}$	$8.4 \cdot 10^{-3}$	$3.2 \cdot 10^{-1}$
8	$4 \cdot 10^{-1}$	$1.4 \cdot 10^{-1}$	$8.1 \cdot 10^{-3}$	$4.3 \cdot 10^{-1}$
9	$7.6 \cdot 10^{-1}$	$2.8 \cdot 10^{-1}$	$5.8 \cdot 10^{-3}$	$8.1 \cdot 10^{-1}$
10	$1 \cdot 10^{0}$	$3.8 \cdot 10^{-1}$	$9.8 \cdot 10^{-3}$	$1.1 \cdot 10^{0}$
11	$8.3 \cdot 10^{-2}$	$3.9 \cdot 10^{-2}$	$1.4 \cdot 10^{-2}$	$9.3 \cdot 10^{-2}$
12	$6.1 \cdot 10^{-1}$	$2.2 \cdot 10^{-1}$	$8.3 \cdot 10^{-3}$	$6.5 \cdot 10^{-1}$
13	$4.2 \cdot 10^{-1}$	$1.5 \cdot 10^{-1}$	$9.9 \cdot 10^{-3}$	$4.5 \cdot 10^{-1}$
14	$3.6 \cdot 10^{-1}$	$1.3 \cdot 10^{-1}$	$7.5 \cdot 10^{-3}$	$3.8 \cdot 10^{-1}$
15	$3.5 \cdot 10^{-1}$	$1.3 \cdot 10^{-1}$	$6.2 \cdot 10^{-3}$	$3.7 \cdot 10^{-1}$
16	$4.5 \cdot 10^{-1}$	$1.6 \cdot 10^{-1}$	$7.8 \cdot 10^{-3}$	$4.8 \cdot 10^{-1}$

Table 5.12: NP - Strategy B2: Δv values

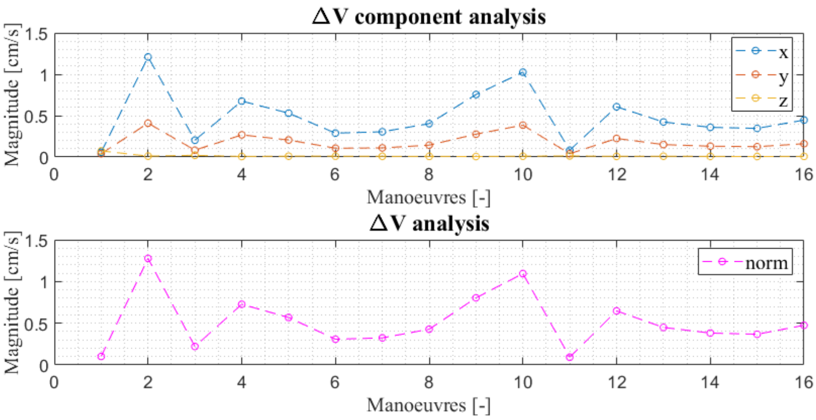

Figure 5.25: NP - Strategy B2: behaviour of Δv

As the time of the manoeuvre is lower, the total time spent for it is lower, leading to an increase of the time for the inspection. The filter phase time, reported in Tab. 5.13, remains quite similar as before, always one order of magnitude lower than the strategy A.

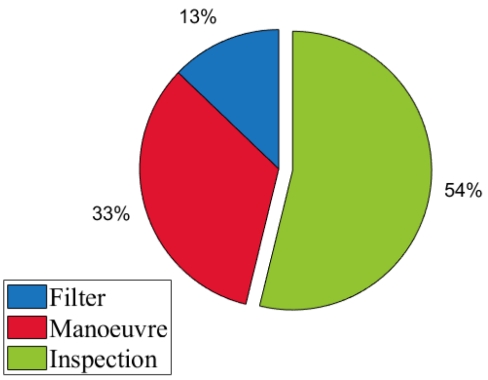

Figure 5.26: NP - Strategy B2: percentage of the phases

Cycle	1	2	3	4	5	6	7	8
Δt_{fil} (s)	3971	383	603	419	484	472	409	384
Cycle	9	10	11	12	13	14	15	16
Δt_{fil} (s)	402	514	612	383	476	447	412	396

Table 5.13: NP - Strategy B2: filter phase times

5.1.8 Manoeuvre analysis

After the strategy B2, the improvements obtained on the manoeuvre phase lead to a new awareness of that phase, arising the curiosity to deepen that aspect. As Sect. 2.4.2 has shown, the updating of the minimization problem could affect the behaviour of the covariance and, at the same time, increase the degree of autonomy of the entire on-board system. To do that, the set of the new minimization problem is based on the addition of new constraints, according to the deputy's parameters and the previous time analysis. Starting from Sect. 5.1.6, the values underlines that some time intervals are better than others for two reasons: the behaviour of the covariance and the fuel consumption. From these, some regions (green ones) have been identified, providing "optimal time of flight" to perform the manoeuvre. Unlike previous strategies, where only one ToF$_M$ can be chosen, it is possible to consider all this time interval and its upper and lower limits will be considered as boundary conditions in the new minimization problem, meanwhile the best ToF$_M$ (minimum Δv), computed in the previous section, will be inserted as initial ToF$_M$ guess of the problem. Regarding the Δv guess, an adequate value has been inserted. The next table summarizes the used values:

Parameter	Value
ToF_{min} (s)	1650
ToF_{max} (s)	2050
$\Delta v_{i,j}$ (cm/s)	10
$\Delta v_{f,j}$ (cm/s)	10
ToF_{guess} (s)	1941
$\Delta v_{i,j,guess}$ (cm/s)	10^{-2}

Table 5.14: NP - Boundary constrains of the minimization problem

where the apex j points each component of the vector considered, meanwhile i and f mean, respectively, initial time and final time.

5.1.9 Strategy C1

This strategy will implement the new minimization problem to compute the best trajectory in the manoeuvre phase and the Tab. 5.15 resumes the values for the various phases used:

Parameter	Value
$\Delta t_{fil,1}$ (s)	3970
Δt_{fil} (s)	*variable*
Δt_{man} (s)	*variable*
Δt_{insp} (s)	3003

Table 5.15: NP - Strategy C1: values of time intervals

The behaviour of the covariance is shown in Fig. 5.27. As it can be seen, the covariance tends to assume an homogeneous behaviour, except for a few peaks that do not represent a huge defect, since they remains under the 40 m. These can be due to the values of the impulse of the manoeuvre, as it will be evident in the Fig. 5.29 and Tab. 5.16.

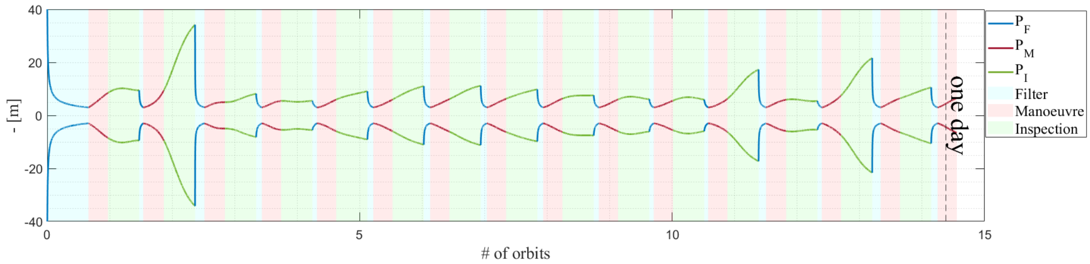

Figure 5.27: NP - Strategy C1: behaviour of the covariance (zoom)

The error is shown in Fig. 5.28 and it has a quite good behaviour, because it stays in the limits, except for the y-component in the first inspection phase of the first cycle. This suggests a further analysis on the inspection phase.

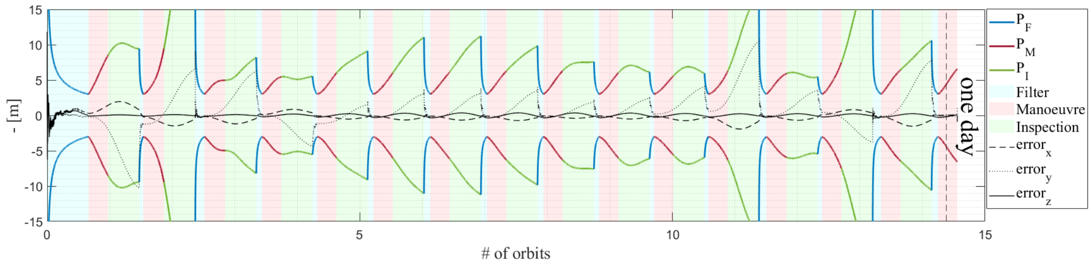

Figure 5.28: NP - Strategy C1: behaviour of the error (zoom)

All the Δv values stays in the order of magnitude of cm/s, as Tab. 5.16 reports.

Manoeuvre (#)	Δv_x (cm/s)	Δv_y (cm/s)	Δv_z (cm/s)	$\lvert\Delta v\rvert$ (cm/s)
1	$4.8 \cdot 10^{-2}$	$1.2 \cdot 10^{-1}$	$4.9 \cdot 10^{-2}$	$1.4 \cdot 10^{-1}$
2	$3.1 \cdot 10^{0}$	$9.1 \cdot 10^{-1}$	$2 \cdot 10^{-1}$	$3.2 \cdot 10^{0}$
3	$5.9 \cdot 10^{-1}$	$2.6 \cdot 10^{-1}$	$8.5 \cdot 10^{-2}$	$6.5 \cdot 10^{-1}$
4	$2.2 \cdot 10^{-1}$	$6.6 \cdot 10^{-2}$	$2.2 \cdot 10^{-2}$	$2.3 \cdot 10^{-1}$
5	$7.2 \cdot 10^{-1}$	$3.1 \cdot 10^{-1}$	$4.4 \cdot 10^{-2}$	$7.9 \cdot 10^{-1}$
6	$8.9 \cdot 10^{-1}$	$4.1 \cdot 10^{-1}$	$7.7 \cdot 10^{-2}$	$9.9 \cdot 10^{-1}$
7	$8.9 \cdot 10^{-2}$	$4.1 \cdot 10^{-1}$	$7.7 \cdot 10^{-2}$	$9.8 \cdot 10^{-1}$
8	$7.8 \cdot 10^{-1}$	$3.2 \cdot 10^{-1}$	$2 \cdot 10^{-2}$	$8.4 \cdot 10^{-1}$
9	$4.6 \cdot 10^{-1}$	$2.2 \cdot 10^{-1}$	$3 \cdot 10^{-2}$	$5.1 \cdot 10^{-1}$
10	$2.8 \cdot 10^{-1}$	$1.2 \cdot 10^{-1}$	$2.6 \cdot 10^{-2}$	$3 \cdot 10^{-1}$
11	$2.3 \cdot 10^{-1}$	$1.8 \cdot 10^{-1}$	$1.9 \cdot 10^{-2}$	$2.9 \cdot 10^{-1}$
12	$1.5 \cdot 10^{0}$	$6.2 \cdot 10^{-1}$	$5 \cdot 10^{-2}$	$1.6 \cdot 10^{0}$
13	$2.9 \cdot 10^{-2}$	$1.4 \cdot 10^{-1}$	$1.7 \cdot 10^{-2}$	$1.5 \cdot 10^{-1}$
14	$1.9 \cdot 10^{-0}$	$8.5 \cdot 10^{-1}$	$4.5 \cdot 10^{-2}$	$2.1 \cdot 10^{0}$
15	$8.3 \cdot 10^{-1}$	$4.3 \cdot 10^{-1}$	$1.2 \cdot 10^{-1}$	$9.5 \cdot 10^{-1}$
16	$6.4 \cdot 10^{-1}$	$3.5 \cdot 10^{-1}$	$6.1 \cdot 10^{-2}$	$7.3 \cdot 10^{-1}$

Table 5.16: NP - Strategy C1: Δv values

As it has already been mentioned, some manoeuvres spend more Δv than others, and this reflects on the behaviour of the covariance. Figure 5.29 proves the idea just expressed.

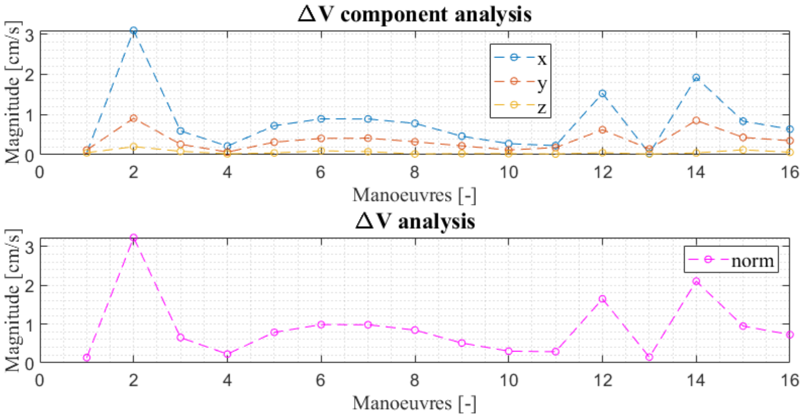

Figure 5.29: NP - Strategy C1: behaviour of Δv

The percentage of the inspection is 52%, which is quite a good value, similar to the previous strategy in Sect. 5.1.7, reported in Fig. 5.30. The time of the phases for each cycle are reported in Tab. 5.17. The overall time dedicated to inspection reaches 12.5 h.

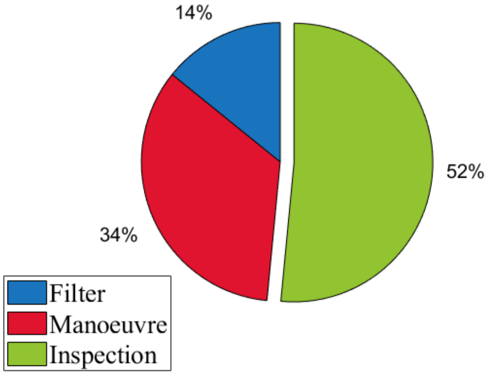

Figure 5.30: NP - Strategy C1: percentage of the phases

Cycle	1	2	3	4	5	6	7	8
Δt_{fil} (s)	3970	387	902	551	437	562	615	587
Δt_{man} (s)	1870	1983	1966	1850	1851	1851	1851	1851
Cycle	9	10	11	12	13	14	15	16
Δt_{fil} (s)	565	490	425	375	705	415	812	618
Δt_{man} (s)	1851	1850	1850	1851	1940	1851	1851	1850

Table 5.17: NP - Strategy C1: phases times

5.1.10 Inspection phase analysis

As it can be noticed from the previous results, sometimes the covariance of the inspection phase grows too much, exceeding the 20-30 m, making the measurement obtained through the filter less precise and increasing the risk to collide with the target. This can be a problem as the initial nominal orbit has been fixed to a determinate distance from the target. In fact, if the radial component of the covariance, in the LVLH frame, is higher than the distance between the target and the deputy, the latter can lie in the KOZ, or worse, a collision may occur. For this reason, a limit on the maximum dimension size for the covariance's growth has been imposed and must be valid at each time instant, independently from the fact that the major contribution of the covariance is given by the radial component. In fact, if from one side the covariance control results relevant to the identification of a probable "zone" (or, in other words, a probable ellipsoid) where the deputy stays, on the other hand the error trend between the values given by the NERM and by the GUT and its control must be taken into account.

To manage the latter detail, again the Sect. 2.5 has been considered. As the graphs of the cited section and Fig. 5.31b show, the behaviour of the error between the linear and nonlinear dynamical models is developed through high peaks and low depression during the time. From this consideration, the first constraint fixed is related to the zone where the inspection phase could stop, to make easy and less expensive the manoeuvre of the next cycle. To do that, the research is started trying to have the possibility to perform the correcting manoeuvre in the area where the error between the NERM and the HCW decreases, so necessarily the inspection phase should be stopped some hundreds of seconds before also to give time for the filter to work well. The area dedicated for the final part of the inspection are, respectively, at 1/3 (about 2000 s) and at 5/6 (about 5000 s) of the nominal orbit, as shown in Fig. 5.31a. Obviously, if one of other constraints is satisfied before this latter, the algorithm will start with a new cycle.

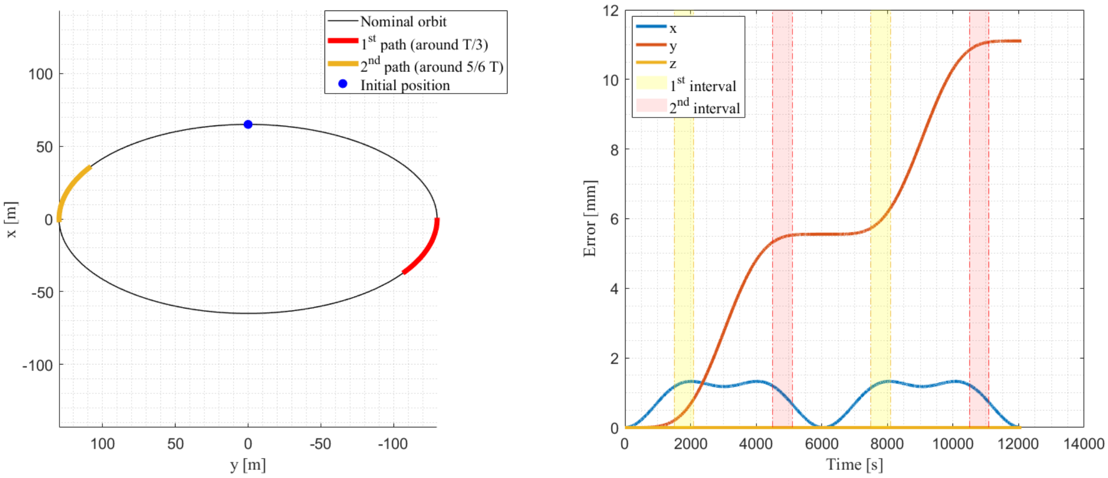

(a) Nominal orbit

(b) HCW-NERM comparison

Figure 5.31: NP - Stopping zones for the inspection phase

The other constraints focus directly on the control of the size of the covariance as function of the determined threshold:

1. the error components between the GUT estimated state and the nominal orbit (propagated by the HCW) shall be necessarily less than the size of the covariance at each time. This process has been chosen to simulate a comparison between

the NERM and the HCW models. In absence of the ”real” trajectory, the GUT estimation substitute them. Moreover, due to the different nature of the NERM and the GUT, the size of the covariance is multiplied by a correcting term that is equal to 0.8, to try to guarantee a certain reliability;

2. the size of the covariance shall be necessarily higher than the estimated position state given by the GUT at each time. In particular, the distance between the target and the deputy is computed by the GUT and this means that the values could not correspond with the ”real” data, as it has already been mentioned in the previous point. In this case, as the introduction of this section underlines, the relative orbit allows to change this threshold based on the position along the path. In particular, to obtain the limit value for the size of the covariance, the distance between the target and the deputy at each time step is divided by 3, in order to have a proportional limit. In this way, the covariance size limit will be always 1/3 of the distance from the target at each time step. This means that, due to the fact that the orbit is elliptical, in the nearest point, the covariance will assume the minimum dimension, while in the farthest point, it will assume the maximum dimension.

5.1.11 Strategy D1

This strategy will be considered as ”autonomous” because all the phases will stop under the imposed conditions, no time has been fixed, and the algorithm is working alone to compute the trajectory, to estimate the deputy's position and to stop the inspection phase when necessary.

Parameter	Value
$\Delta t_{fil,1}$ (s)	3970
Δt_{fil} (s)	*variable*
Δt_{man} (s)	*variable*
Δt_{insp} (s)	*variable*

Table 5.18: NP - Strategy D1: values of time intervals

The behaviour of the covariance is shown in Fig. 5.32. In the first half of the simulation time, the trend does not result homogeneous due to the fixed constraints. After the long inspection phase of the first cycle, the algorithm tries to stabilize the time phases and their respective covariance, satisfying the conditions imposed. For the other half of the simulation, the behaviour returns to be similar to the previous strategy, maintaining an overall cycle time around 6000 s (that corresponds to the period of the nominal orbit).

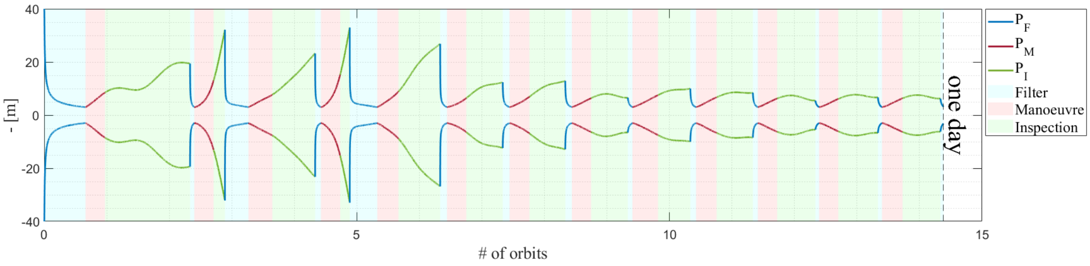

Figure 5.32: NP - Strategy D1: behaviour of the covariance (zoom)

The error is shown in Fig. 5.33. As in the previous strategy, due to selection of time interval where the manoeuvre shall be performed, the error trend is not a reason for problems.

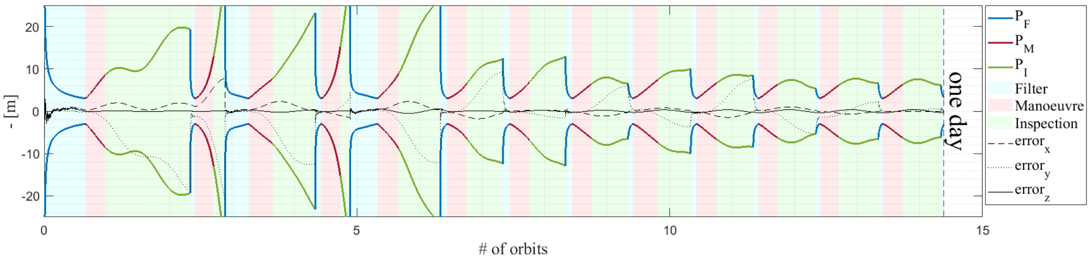

Figure 5.33: NP - Strategy D1: behaviour of the error (zoom)

The cost for the manoeuvres is listed in Tab. 5.19. The values respect the constraints of Δv and, as the Fig. 5.34 shows better the trend of Δv, which tends to decrease during the time, and at the beginning, when the algorithm tries to reach the stability, the manoeuvres have higher cost than the lasts.

Manoeuvre (#)	Δv_x (cm/s)	Δv_y (cm/s)	Δv_z (cm/s)	$\lvert\Delta v\rvert$ (cm/s)
1	$4.8 \cdot 10^{-2}$	$1.2 \cdot 10^{-1}$	$4.9 \cdot 10^{-2}$	$1.4 \cdot 10^{-1}$
2	$5.6 \cdot 10^{0}$	$2 \cdot 10^{0}$	$1 \cdot 10^{-1}$	$6 \cdot 10^{0}$
3	$1.8 \cdot 10^{0}$	$1.2 \cdot 10^{-1}$	$1.3 \cdot 10^{-1}$	$1.8 \cdot 10^{0}$
4	$6.7 \cdot 10^{0}$	$2.5 \cdot 10^{0}$	$1.9 \cdot 10^{-1}$	$7.2 \cdot 10^{0}$
5	$2.2 \cdot 10^{0}$	$5.7 \cdot 10^{-1}$	$5.7 \cdot 10^{-2}$	$2.2 \cdot 10^{0}$
6	$1 \cdot 10^{0}$	$5.2 \cdot 10^{-1}$	$1.2 \cdot 10^{-1}$	$1.2 \cdot 10^{0}$
7	$1.1 \cdot 10^{0}$	$4.6 \cdot 10^{-1}$	$2.4 \cdot 10^{-2}$	$1.2 \cdot 10^{0}$
8	$3.1 \cdot 10^{-1}$	$1.5 \cdot 10^{-1}$	$4.9 \cdot 10^{-2}$	$3.5 \cdot 10^{-1}$
9	$8.4 \cdot 10^{-1}$	$9.8 \cdot 10^{-2}$	$1.1 \cdot 10^{-2}$	$8.4 \cdot 10^{-1}$
10	$5.4 \cdot 10^{-1}$	$2.4 \cdot 10^{-1}$	$2.2 \cdot 10^{-2}$	$6 \cdot 10^{-1}$
11	$1.4 \cdot 10^{-2}$	$5.7 \cdot 10^{-2}$	$4.1 \cdot 10^{-2}$	$7.2 \cdot 10^{-2}$
12	$4.3 \cdot 10^{-1}$	$1.5 \cdot 10^{-1}$	$1 \cdot 10^{-2}$	$4.6 \cdot 10^{-1}$
13	$2.8 \cdot 10^{-1}$	$1.1 \cdot 10^{-1}$	$4.5 \cdot 10^{-2}$	$3 \cdot 10^{-1}$

Table 5.19: NP - Strategy D1: Δv values

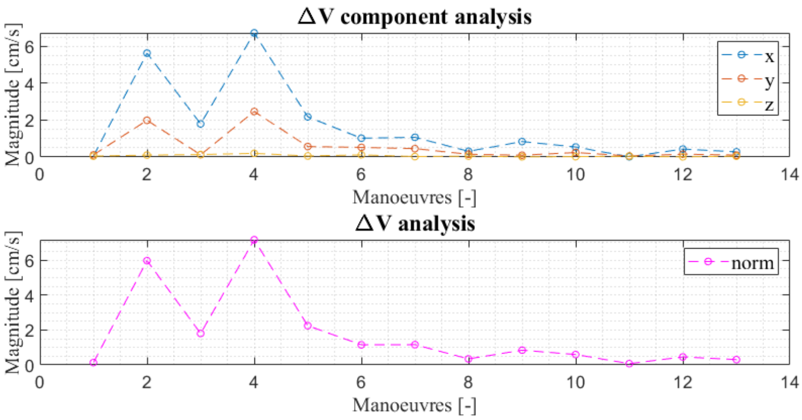

Figure 5.34: NP - Strategy D1: behaviour of Δv

The percentage of the inspection in still good, at a value of 53%, around 11.9 h, while the filter phase lasts 3.86 h and the manoeuvre phase 6.57 h.

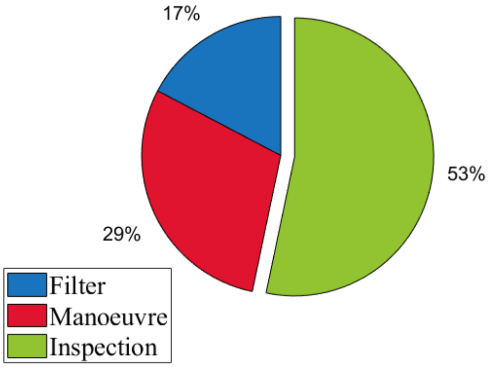

Figure 5.35: NP - Strategy D1: percentage of the phases

Table 5.20 presents the time duration of each phase. Unlike the previous strategy in Sect. 5.1.9, the Δt_{insp} varies and, in the most of the cases, it is longer than the value of 3003 s, imposed at the beginning of the analysis.

Cycle	1	2	3	4	5	6	7	8
Δt_{fil} (s)	3971	405	2258	549	2643	654	657	635
Δt_{man} (s)	1870	1855	2299	1856	2037	1851	1906	1850
Δt_{insp} (s)	8174	1090	4107	921	4008	3502	3444	3522
Cycle	9	10	11	12	13			
Δt_{fil} (s)	449	551	479	353	301			
Δt_{man} (s)	2452	1974	1851	1850				
Δt_{insp} (s)	3106	3482	3677	3804				

Table 5.20: NP - Strategy D1: phase times

5.1.12 Strategy D2

Let's take a step back. Considering the strategy B2, there is a clear increment of the inspection phase due to the reduction of the manoeuvring time, so an obvious question arises: how about vary the inspection phase to see what happen?
This new strategy borns from this idea and both the strategy B2 will be analyzed, varying the inspection phase imposing the conditions explained in Sect. 5.1.10 in order to see if a further increase in the total inspection time can be achieved.

Minimum Δv_{tot}

The phase time use are listed in Tab. 5.21.

Parameter	Value
$\Delta t_{fil,1}$ (s)	3970
Δt_{fil} (s)	*variable*
Δt_{man} (s)	1941
Δt_{insp} (s)	*variable*

Table 5.21: NP - Strategy D2: values of time intervals

The behaviour of the covariance is shown in Fig. 5.36. As it can be noticed, the behaviour is similar to the strategy D1, where on the second half of the simulation, there is a kind of pattern that stabilize the cycle to last one orbit period.

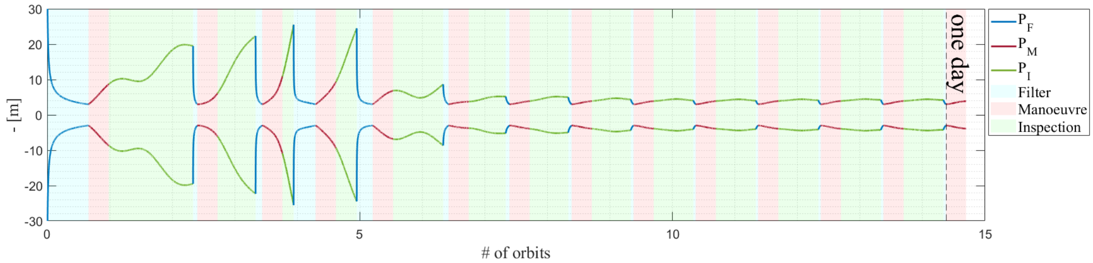

Figure 5.36: NP - Strategy D2: behaviour of the covariance (zoom)

The error is shown in Fig. 5.37. In the second cycle the y-component of the error goes out of the limits, which cause an inaccuracy in the estimation of the position of the deputy.

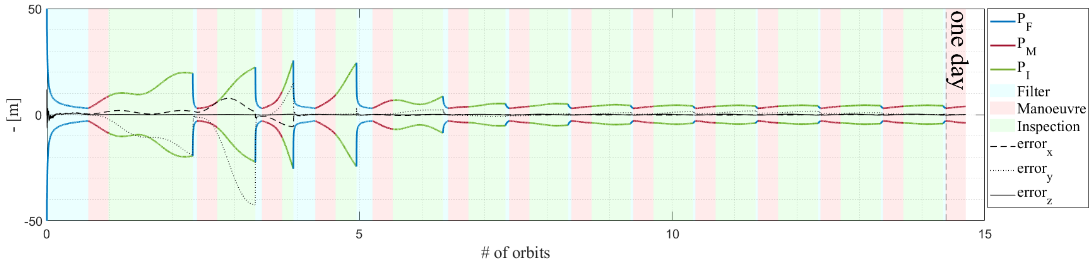

Figure 5.37: NP - Strategy D2: behaviour of the error (zoom)

The cost for the manoeuvres is listed in Tab. 5.22. As expected, the higher values are the first ones, then, the values set to lower magnitude.

Manoeuvre (#)	Δv_x (cm/s)	Δv_y (cm/s)	Δv_z (cm/s)	$\lvert\Delta v\rvert$ (cm/s)
1	$5.5 \cdot 10^{-2}$	$3.4 \cdot 10^{-2}$	$7.3 \cdot 10^{-2}$	$9.7 \cdot 10^{-2}$
2	$1.9 \cdot 10^{0}$	$5.4 \cdot 10^{-1}$	$1.5 \cdot 10^{-2}$	$2 \cdot 10^{0}$
3	$4.5 \cdot 10^{0}$	$1.3 \cdot 10^{0}$	$2 \cdot 10^{-2}$	$4.7 \cdot 10^{0}$
4	$2.9 \cdot 10^{0}$	$9 \cdot 10^{-1}$	$2.9 \cdot 10^{-2}$	$3.1 \cdot 10^{0}$
5	$3.3 \cdot 10^{-2}$	$4.7 \cdot 10^{-3}$	$1.4 \cdot 10^{-2}$	$3.6 \cdot 10^{-2}$
6	$2.7 \cdot 10^{-1}$	$9.4 \cdot 10^{-2}$	$3.4 \cdot 10^{-2}$	$2.9 \cdot 10^{-1}$
7	$4.2 \cdot 10^{-2}$	$1.4 \cdot 10^{-2}$	$9.8 \cdot 10^{-3}$	$4.5 \cdot 10^{-2}$
8	$3.2 \cdot 10^{-2}$	$9.1 \cdot 10^{-3}$	$3.2 \cdot 10^{-3}$	$3.3 \cdot 10^{-2}$
9	$7.1 \cdot 10^{-2}$	$2 \cdot 10^{-2}$	$2.1 \cdot 10^{-3}$	$7.4 \cdot 10^{-2}$
10	$8.7 \cdot 10^{-2}$	$2.5 \cdot 10^{-2}$	$1.2 \cdot 10^{-3}$	$9.1 \cdot 10^{-2}$
11	$1.1 \cdot 10^{-1}$	$3.1 \cdot 10^{-2}$	$1.2 \cdot 10^{-3}$	$1.1 \cdot 10^{-1}$
12	$1.1 \cdot 10^{-1}$	$3.2 \cdot 10^{-2}$	$1.2 \cdot 10^{-3}$	$1.1 \cdot 10^{-1}$
13	$6.1 \cdot 10^{-2}$	$1.9 \cdot 10^{-2}$	$1.3 \cdot 10^{-3}$	$6.4 \cdot 10^{-2}$
14	$1.9 \cdot 10^{-2}$	$5.6 \cdot 10^{-3}$	$9.8 \cdot 10^{-4}$	$2 \cdot 10^{-2}$

Table 5.22: NP - Strategy D2: Δv values

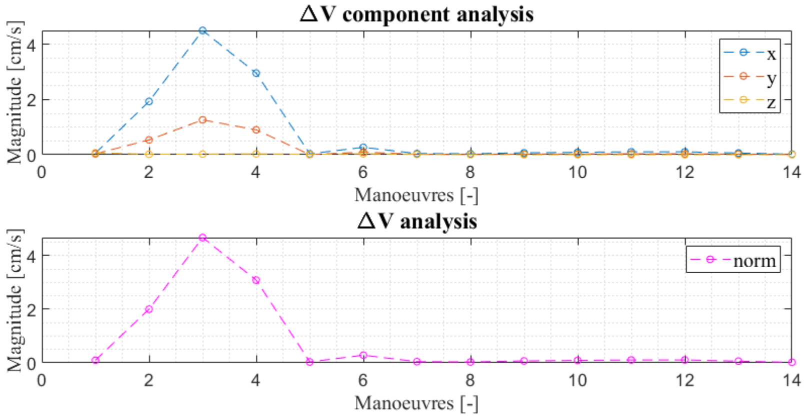

Figure 5.38: NP - Strategy D2: behaviour of Δv

The percentage of the inspection is increased from 52% to 57%, as expected before.

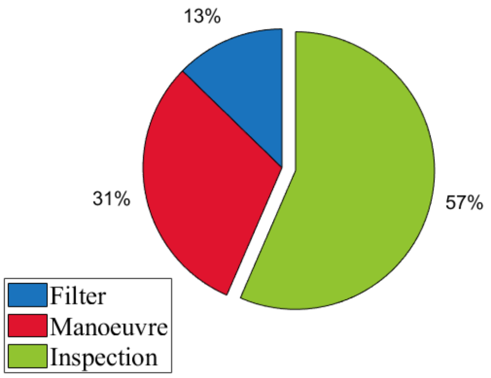

Figure 5.39: NP - Strategy D2: percentage of the phases

Cycle	1	2	3	4	5	6	7	8	9	10	11	12	13	14
Δt_{fil} (s)	3971	405	633	2112	1535	509	356	319	258	223	214	224	233	225
Δt_{insp} (s)	8103	3661	1080	2011	4827	3557	3710	3747	3808	3843	3852	3842	3833	

Table 5.23: NP - Strategy D2: phase times

Best covariance's behaviour

The phase time used are listed in Tab. 5.24.

Parameter	Value
$\Delta t_{fil,1}$ (s)	3970
Δt_{fil} (s)	*variable*
Δt_{man} (s)	1744
Δt_{insp} (s)	*variable*

Table 5.24: NP - Strategy D2: values of time intervals

The behaviour of the covariance is shown in Fig. 5.40. Again, there is a kind of stabilization towards a pattern that lead to set the time of the cycle equal to one orbit period.

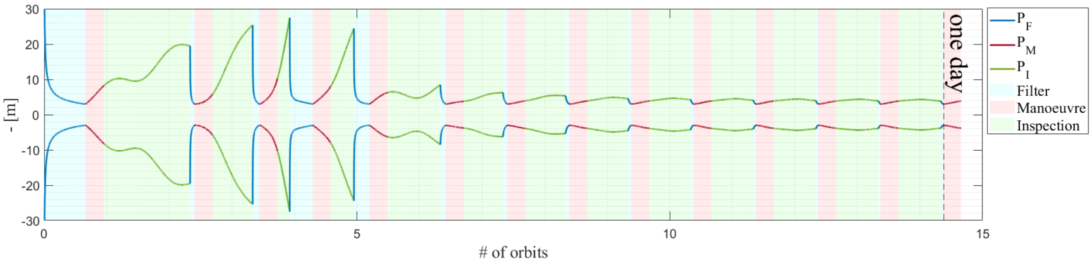

Figure 5.40: NP - Strategy D2: behaviour of the covariance (zoom)

The error is shown in Fig. 5.41. Also in this case, in the second cycle, the y-component goes out the limits and this is due to the long inspection time in the first cycle, which cause a successive higher manoeuvre.

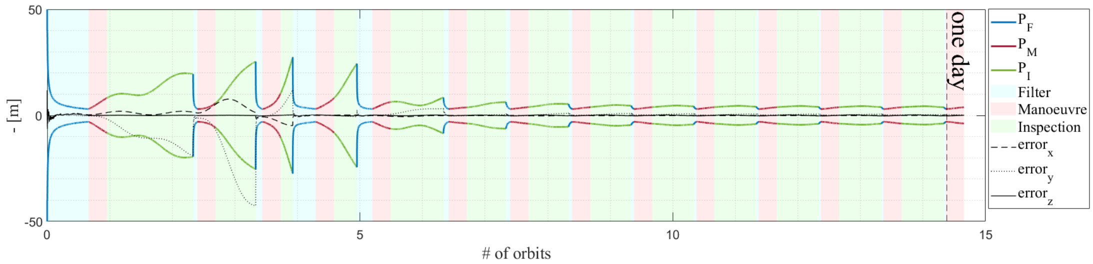

Figure 5.41: NP - Strategy D2: behaviour of the error (zoom)

The cost for the manoeuvre is listed in Tab. 5.25. The higher values are the first ones, as expected from the behaviour of the covariance.

Manoeuvre (#)	Δv_x (cm/s)	Δv_y (cm/s)	Δv_z (cm/s)	$\|\Delta v\|$ (cm/s)
1	$5.8 \cdot 10^{-2}$	$4 \cdot 10^{-2}$	$7.4 \cdot 10^{-2}$	$1 \cdot 10^{-1}$
2	$2.2 \cdot 10^{0}$	$7.7 \cdot 10^{-1}$	$1.3 \cdot 10^{-2}$	$2.3 \cdot 10^{0}$
3	$4.9 \cdot 10^{0}$	$1.8 \cdot 10^{0}$	$1.8 \cdot 10^{-2}$	$5.3 \cdot 10^{0}$
4	$2.9 \cdot 10^{0}$	$1.1 \cdot 10^{0}$	$4.4 \cdot 10^{-2}$	$3.1 \cdot 10^{0}$
5	$1 \cdot 10^{-1}$	$4.5 \cdot 10^{-2}$	$1.3 \cdot 10^{-2}$	$1.2 \cdot 10^{-1}$
6	$4 \cdot 10^{-1}$	$1.7 \cdot 10^{-1}$	$3.1 \cdot 10^{-2}$	$4.4 \cdot 10^{-1}$
7	$6.4 \cdot 10^{-2}$	$2.1 \cdot 10^{-2}$	$8.5 \cdot 10^{-3}$	$6.8 \cdot 10^{-2}$
8	$9.2 \cdot 10^{-2}$	$3.4 \cdot 10^{-2}$	$1.3 \cdot 10^{-3}$	$9.8 \cdot 10^{-2}$
9	$7.5 \cdot 10^{-2}$	$2.8 \cdot 10^{-2}$	$1.1 \cdot 10^{-3}$	$8 \cdot 10^{-2}$
10	$6.9 \cdot 10^{-2}$	$2.5 \cdot 10^{-2}$	$1.8 \cdot 10^{-3}$	$7.3 \cdot 10^{-2}$
11	$5.7 \cdot 10^{-2}$	$2.1 \cdot 10^{-2}$	$1.2 \cdot 10^{-3}$	$6.1 \cdot 10^{-2}$
12	$5.4 \cdot 10^{-2}$	$2 \cdot 10^{-2}$	$1.5 \cdot 10^{-3}$	$5.8 \cdot 10^{-2}$
13	$3.5 \cdot 10^{-2}$	$1.4 \cdot 10^{-2}$	$1.8 \cdot 10^{-3}$	$3.8 \cdot 10^{-2}$
14	$4.4 \cdot 10^{-3}$	$2.6 \cdot 10^{-3}$	$4.8 \cdot 10^{-3}$	$7 \cdot 10^{-3}$

Table 5.25: NP - Strategy D2: Δv values

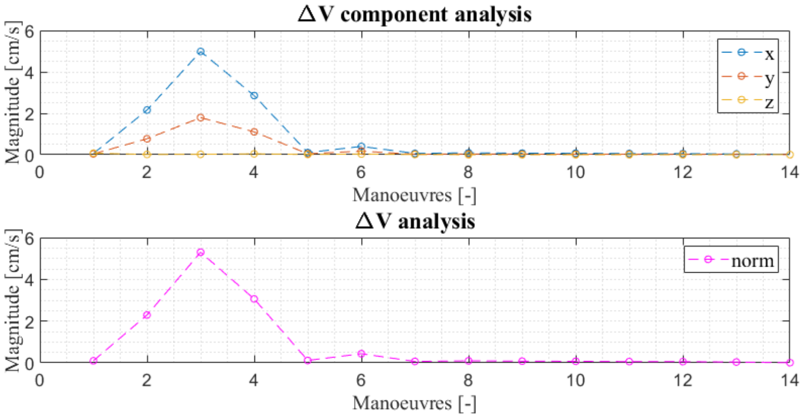

Figure 5.42: NP - Strategy D2: behaviour of Δv

The percentage of the inspection is increased from 54% to 59%. Again, there is an increment in the total inspection time, as expected, leading to the higher value obtained so far.

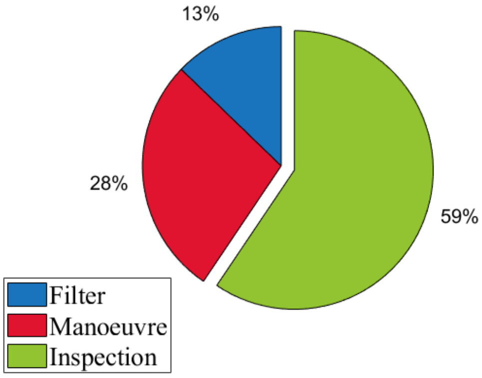

Figure 5.43: NP - Strategy D2: percentage of the phases

Cycle	1	2	3	4	5	6	7	8
Δt_{filt} (s)	3971	405	632	2200	1479	499	407	344
Δt_{insp} (s)	8300	3858	1183	2218	5077	3764	3856	3919
Cycle	9	10	11	12	13	14		
Δt_{filt} (s)	282	246	223	207	194	181		
Δt_{insp} (s)	3981	4017	4040	4056	4069			

Table 5.26: NP - Strategy D2: phase times

5.1.13 Resume

In conclusion, a comparison between the total inspection time and the total cost in terms of Δv has been made for each of the strategy. Fig. 5.44 shows the results. The total region has been divided into 4 quadrants:

1. *top left*: high cost and low inspection time (red region);
2. *bottom left*: low cost but low inspection time (yellow region);
3. *top right*: high inspection time but high cost (yellow region);
4. *bottom right*: low cost and high inspection time (green region).

In order to maximize the inspection time and reduce the cost of the mission to the minimum, the green region is the one with the better strategies. In addition, the color of the marker indicates the quality of the algorithm, in terms of the behaviour of the covariance and the associated error:

- **red**: the covariance's dimensions increase too much, with a risk of collision with the target;

- **blue**: the error goes out of the covariance limits, leading to an incorrect estimation of the position of the satellite;
- **green**: good behaviour of the covariance and the error.

Considering the strategies in the green region, shown in Fig. 5.45, the blue ones, D2$_{dv}$ and D2$_{cov}$, are the best in terms of inspection time, but the behaviour of the error leads to discard these two strategies. Then, among the green ones, B2$_{dv}$, B2$_{cov}$, C1 and D1, shown in Fig. 5.45, the first three have a similar inspection time and cost, while the D1 has a little lower inspection time and a little higher cost. Another aspect to consider is also the degree of autonomy: in fact, the strategy D1 can be considered fully autonomous and, since the cost and the inspection time are similar to the ones with lower degree of autonomy, this can be considered the best strategy.

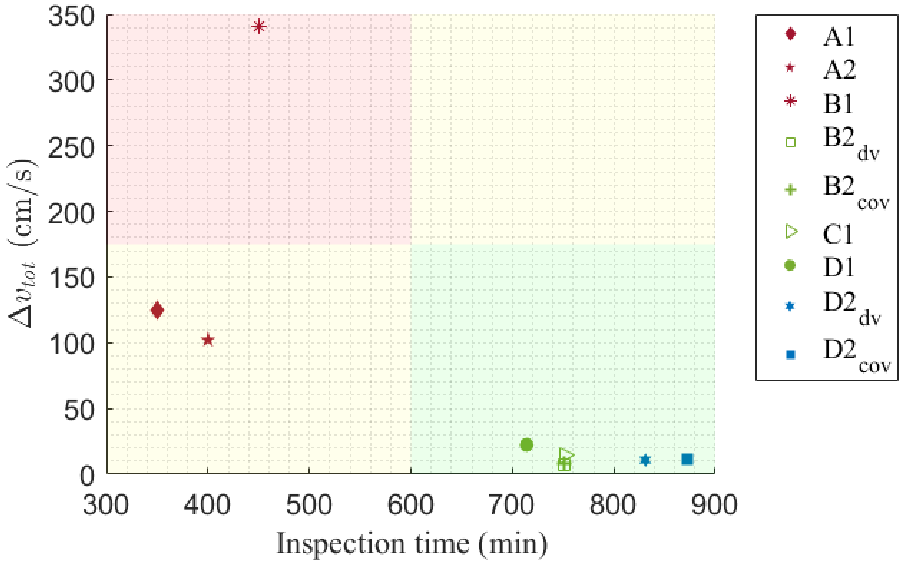

Figure 5.44: NP - Comparison of the different strategies

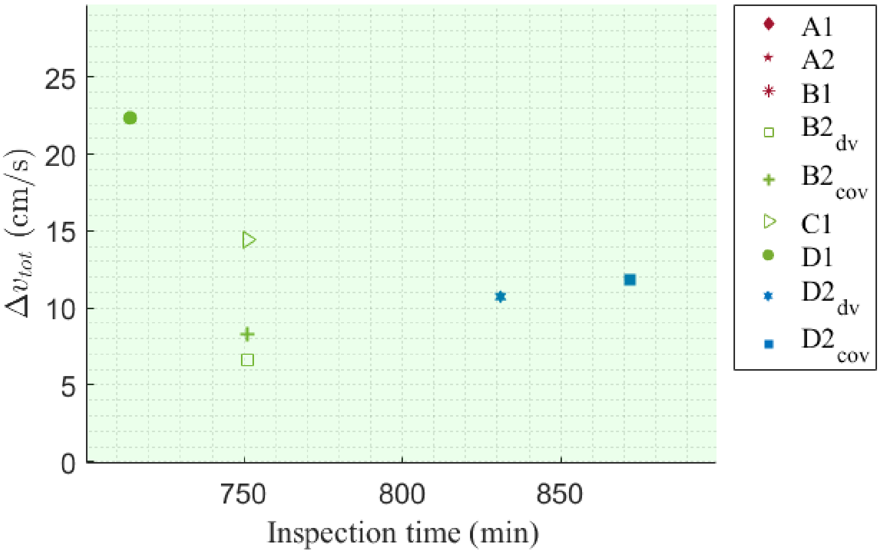

Figure 5.45: NP - Comparison of the different strategies (zoom)

5.1.14 Visibility analysis

In the following paragraph, the green strategies in the green region marked in Fig. 5.45 are analyzed. In particular, a further step to simulate a real scenario is made: since Envisat is a tumbling spacecraft, the measurement model has been updated following the steps shown in Sect. 3.3, to have a tumbling target. Then, the visibility, in the sense of what face is seen and for how many seconds, has been analyzed. The results for each strategy are shown below, while the initial conditions are reported in Tab. 4.3.

Strategy B2 - Minimum Δv_{tot}

Fig. 5.46 reports for how much time in seconds each face is seen by the deputy, assuming that the camera is always pointed towards the center of mass of the target. As it can be seen, there is an increase in the faces 1, 3, 6 and a decrease in the faces 2, 4, 5, passing from a fixed target configuration to a tumbling target configuration. This suggests that in the fixed target case, the inspection phase has a sort of repetitiveness. In particular, the inspection can occur almost always on the part of the nominal orbit from which the faces 2, 4, 5 are visible. Also, in the case of tumbling target, the distribution of the visible faces is more sparse than in the case of fixed target, as shown in Fig. 5.47. In particular, there is a higher visibility during each inspection phase, while for the case of fixed target, there is the possibility that one or more of the faces are not visible during some phases.

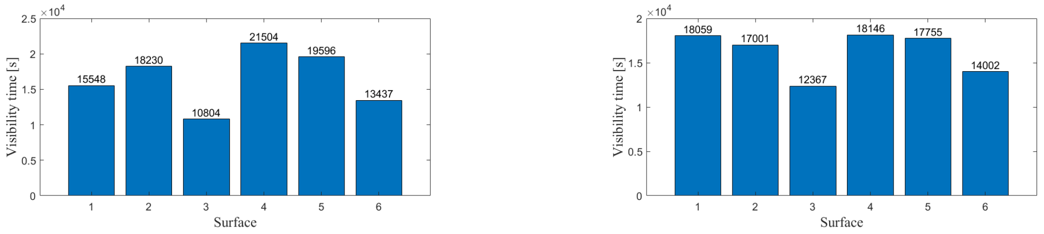

(a) Fixed target (b) Tumbling target

Figure 5.46: NP - Strategy B2: visibility time for each of the face

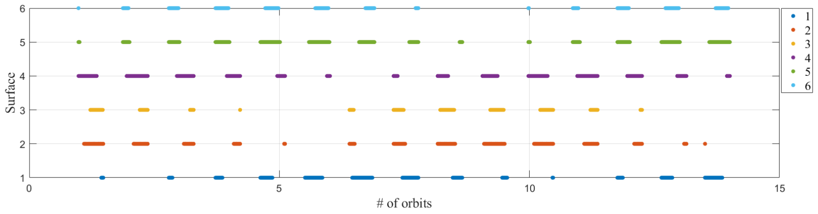

(a) Fixed target

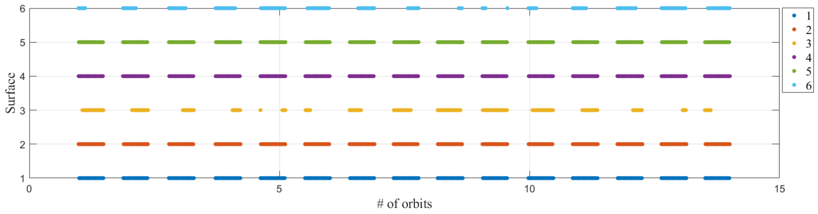

(b) Tumbling target

Figure 5.47: NP - Strategy B2: visibility in time for each of the face

Strategy B2 - Best covariance's behaviour

Also for this strategy, the results are similar. There is an increase of visibility of faces 1, 3, 6, in the case of tumbling target. This can be due to the fact that the strategy is similar, the only thing that changes is the time of flight spent for the manoeuvre. Again, the distribution of the visibility of the faces is more sparse in the tumbling case, guaranteeing that every faces is acquired by the camera at every inspection phase.

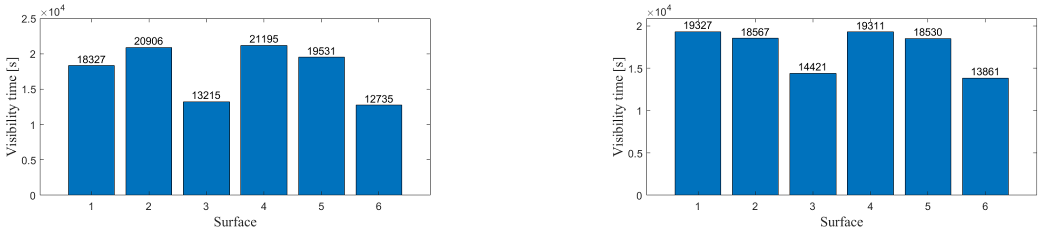

(a) Fixed target (b) Tumbling target

Figure 5.48: NP - Strategy B2: visibility time for each of the face

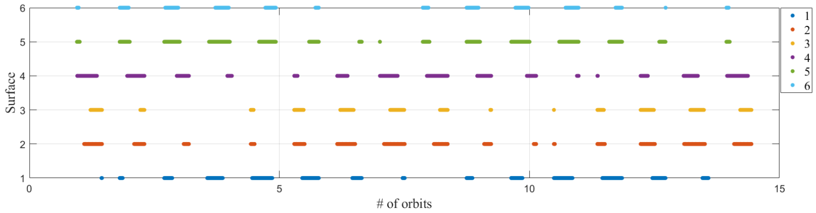

(a) Fixed target

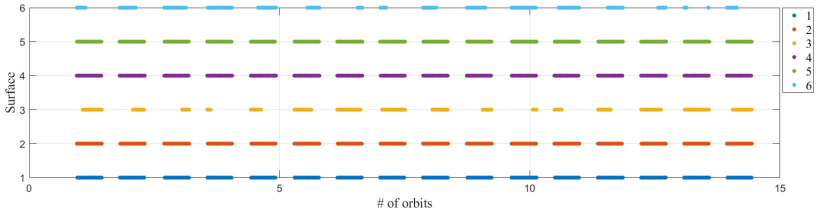

(b) Tumbling target

Figure 5.49: NP - Strategy B2: visibility in time for each of the face

Strategy C1

This strategy presents the variation of the filter and the manoeuvre phases. This means that the inspection will be performed in different parts of the nominal orbit, leading to a more sparse distribution of the visibility time. As it can be seen in Fig. 5.50, unfortunately, the distribution is not as sparse as expected, maybe because the strategy assumes a kind of pattern, in which the phases last a similar time, leading again to a repetition of inspection phase along the same part of the orbit. Again, the tumbling case guarantees a better visibility time for each inspection phase.

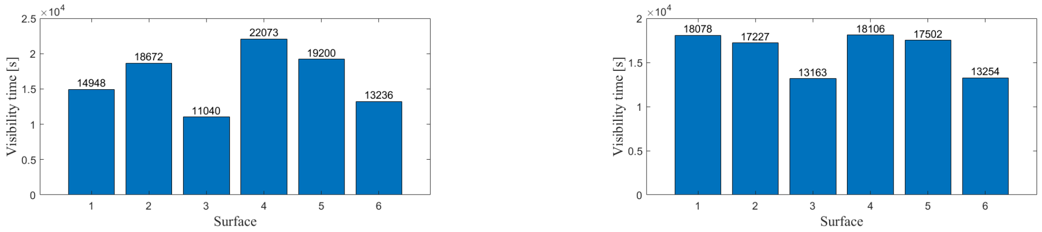

(a) Fixed target (b) Tumbling target

Figure 5.50: NP - Strategy C1: visibility time for each of the face

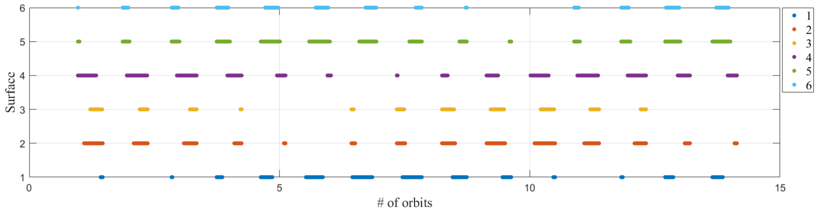

(a) Fixed target

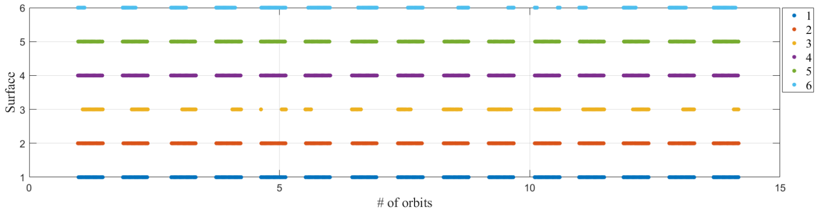

(b) Tumbling target

Figure 5.51: NP - Strategy C1: visibility in time for each of the face

Strategy D1

The autonomous strategy presents a very low visibility for the faces 3, compared to the other ones, one order of magnitude lower in the fixed target configuration. Since the nominal orbit is planar, this suggests that the face 3 is in an unfavourable position, given by the initial conditions. In Fig. 5.52, the visibility time is reported and it can be noticed that the absolute value for some faces is higher in the fixed target configuration, but the tumbling target configuration offers a better distribution of the face visibility at each inspection phase, as Fig. 5.53 shows.

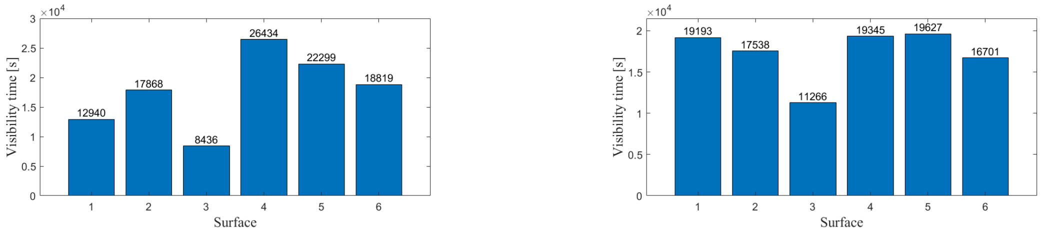

(a) Fixed target (b) Tumbling target

Figure 5.52: NP - Strategy D1: visibility time for each of the face

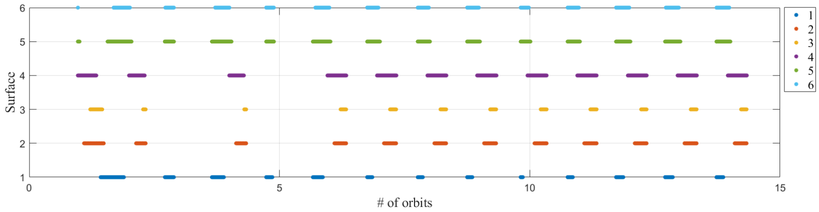

(a) Fixed target

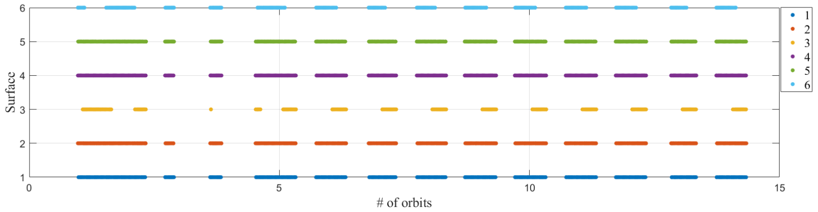

(b) Tumbling target

Figure 5.53: NP - Strategy D1: visibility in time for each of the face

A final analysis has been carried out: for all the strategies presented before, with the fixed and tumbling target configurations, the visibility time of each of the faces with respect to the inspection time, in this case 12 hours of inspection, has been reported in Fig. 5.54. As it can be seen, for all the tumbling target cases, there is a more homogeneous increment for each of the faces, while in the fixed target case, the increment is more irregular, leading to a more sparse visibility time of the faces after 12 hours of inspection. Among the strategies with a tumbling target configurations, all of them reaches a maximum of 5 hours of visibility for at least one face, after 12 hours of inspection, in a one day mission and a minimum of at least 3 hours for every face, except for the strategy D1.

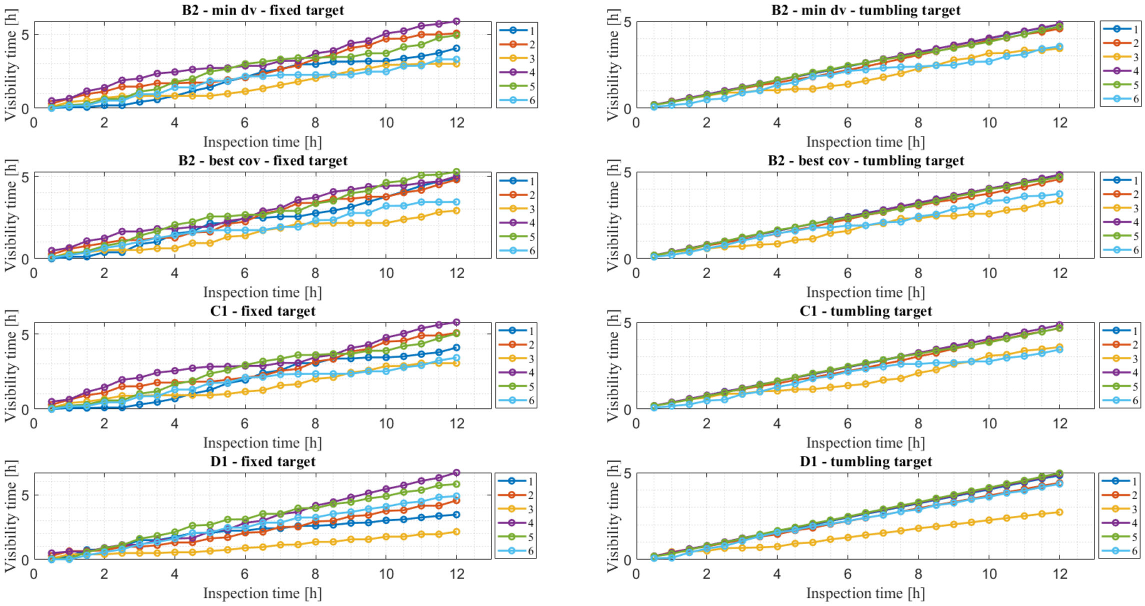

Figure 5.54: NP - Visibility time vs inspection time for each of the strategy

5.2 Perturbed case

In this chapter, the results of the simulation with the external dynamics represented by the perturbed NERM and the on-board dynamics represented by the HCW are exposed.

5.2.1 Strategy A1

Following the steps of Sect. 5.1.1, this first strategy considers all the phases with a fixed time, adding the perturbation term due to J2. The specific time for each phases are listed in Tab. 5.27.

Parameter	Value
Δt_{fil}	6007 s
Δt_{man}	3003 s
Δt_{insp}	3003 s

Table 5.27: P - Strategy A1: values of time intervals

Taking into account Fig. 5.55, it can be noticed that the trend of the covariance computed is quite good: except for the inspection phase of the first cycle, the graph develops in a regular way, and it does not suggest the presence of expensive manoeuvres.

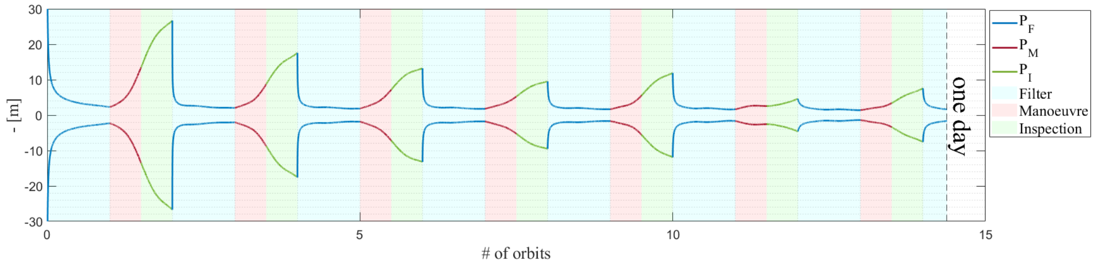

Figure 5.55: P - Strategy A1: behaviour of the covariance (zoom)

On the other hand, the behaviour of the error components in Fig. 5.56 is not the best among those exposed previously. Specifically, the y-component error is the most relevant term, due to the "shifting effect" given by nonlinear and, mostly, perturbation terms. This effect grows along the simulation time, together with the other error components.

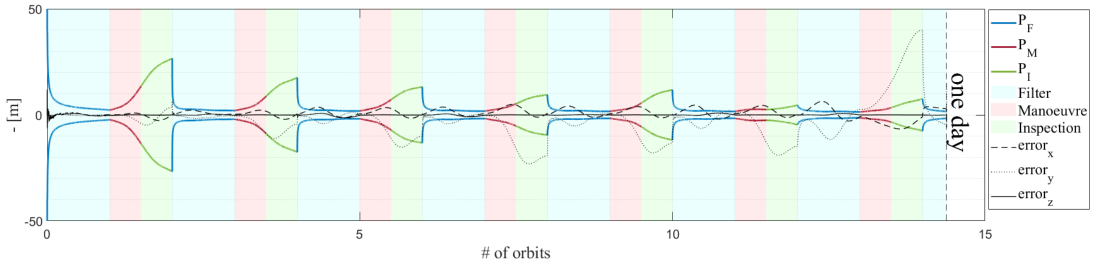

Figure 5.56: P - Strategy A1: behaviour of the error (zoom)

Regarding the fuel consumption, the cost of each manoeuvre, shown in Tab. 5.28, could be considered higher than the unperturbed strategies but, unlike those, the Δv limits related to each burn (that will be imposed also in the perturbed case) would be already satisfied.

Manoeuvre (#)	Δv_x (cm/s)	Δv_y (cm/s)	Δv_z (cm/s)	$\lvert\Delta v\rvert$ (cm/s)
1	$6.8 \cdot 10^{-1}$	$2 \cdot 10^{-1}$	$2.4 \cdot 10^{0}$	$2.5 \cdot 10^{0}$
2	$1.4 \cdot 10^{0}$	$7 \cdot 10^{-2}$	$9.7 \cdot 10^{-1}$	$1.7 \cdot 10^{0}$
3	$5 \cdot 10^{-1}$	$8.7 \cdot 10^{-2}$	$1 \cdot 10^{0}$	$1.2 \cdot 10^{0}$
4	$7.5 \cdot 10^{-2}$	$1.9 \cdot 10^{-1}$	$8 \cdot 10^{-1}$	$8.1 \cdot 10^{-1}$
5	$1 \cdot 10^{0}$	$1.6 \cdot 10^{-1}$	$4.1 \cdot 10^{-1}$	$1.1 \cdot 10^{0}$
6	$3.4 \cdot 10^{-1}$	$1.3 \cdot 10^{-1}$	$1.1 \cdot 10^{-1}$	$3.8 \cdot 10^{-1}$
7	$7.6 \cdot 10^{-1}$	$1.3 \cdot 10^{-1}$	$7 \cdot 10^{-2}$	$7.8 \cdot 10^{-1}$

Table 5.28: P - Strategy A1: Δv values

This phenomenon could be associated to the periodic pattern of the cycle: performing the manoeuvre in the same point along the relative orbit and adopting specific dynamical models, the deputy will be distant enough to perform a similar burn every cycle, as Fig. 5.57 shows.

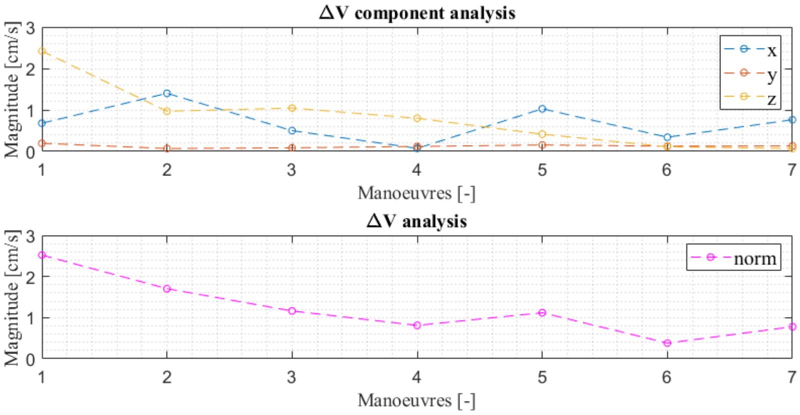

Figure 5.57: P - Strategy A1: behaviour of Δv

Finally, the Fig. 5.58 confirm the time partition imposed at the beginning of the strategy.

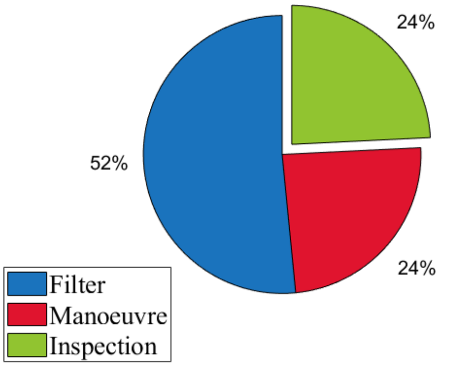

Figure 5.58: P - Strategy A1: percentage of the phases

5.2.2 Filter Analysis 1/2

The same analysis presented in Sect. 5.1.2 has been performed using the perturbed model and the results are shown in Fig. 5.59. In this case, after one orbit, the covariance reaches a value slightly higher than in the unperturbed case, due to the different nature of the external dynamics. In addition, the error needs more time to stabilize and reach an asymptote. Again, the value of time delay is the same for each of the sample. The last value of time delay selected for which the error is contained in the band is 3967 s, three second lower than the unperturbed case, which corresponds to a dimension of the covariance of 3 m, the same value found in the unperturbed case. This time has been set for the filter phase in the next strategy.

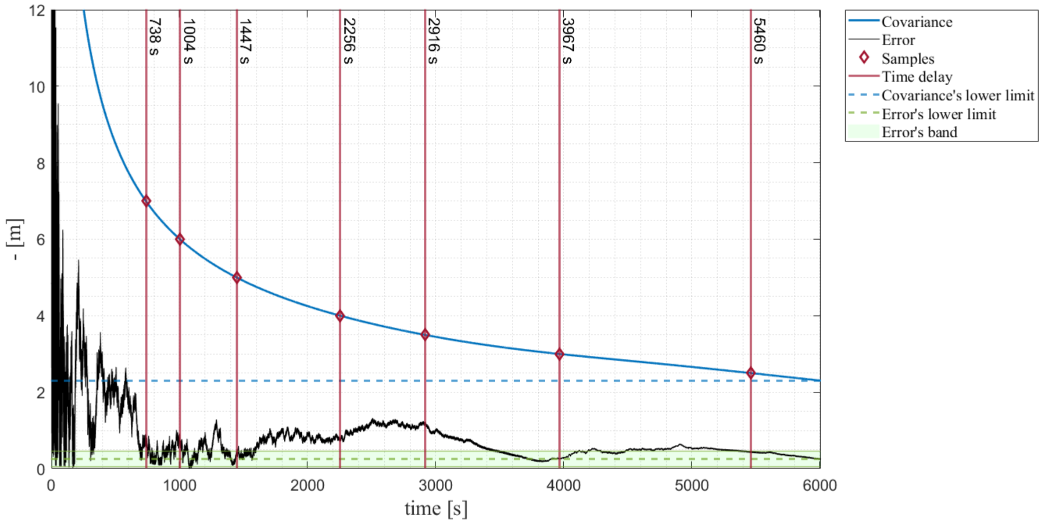

Figure 5.59: P - Delay time for each sample

5.2.3 Strategy A2

For this strategy, the time of the phases used are reported in Tab. 5.29:

Parameter	Value
Δt_{fil}	3967 s
Δt_{man}	3003 s
Δt_{insp}	3003 s

Table 5.29: P - Strategy A2: values of time intervals

Starting from the covariance discussion, as it can be seen in Fig. 5.60, it has a worse development, reaching higher peaks with respect to the previous strategy. This can be a sign that, despite a decrease in the filter time, the concept of the strategy does not contribute in an efficient way to the improvement of the algorithm.

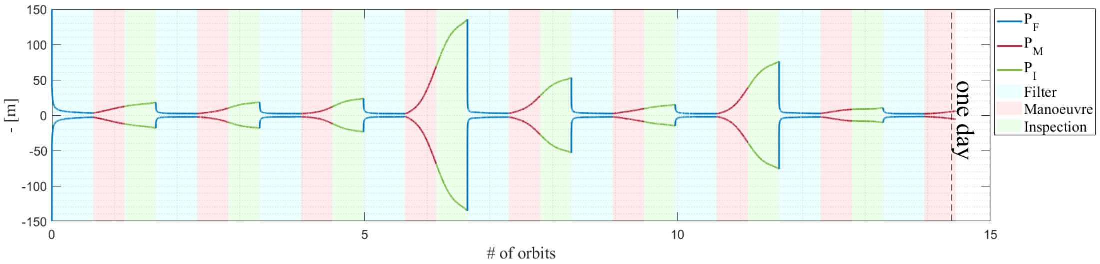

Figure 5.60: P - Strategy A2: behaviour of the covariance

Regarding the error, the y-component grows until it exits the covariance, while x and z-components remains in the limits imposed, as shown in Fig. 5.61

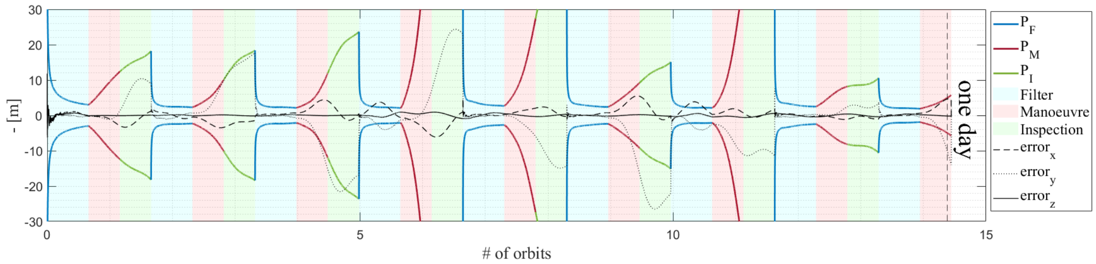

Figure 5.61: P - Strategy A2: behaviour of the error (zoom)

Instead, the cost of the burns starts to be interesting. As it can be seen in Tab. 5.30, both the x and z-components provide high contributions in terms of Δv. This can be explained through the changing of the dynamical model for the external simulation environment. In fact, as Figs. 2.5 and 2.6b show, after one orbital period, while the y-component error tends to decrease, the others increase. This is why the main Δv contributions are given by x and z coordinates.

Manoeuvre (#)	Δv_x (cm/s)	Δv_y (cm/s)	Δv_z (cm/s)	$\|\Delta v\|$ (cm/s)
1	$6.3 \cdot 10^{-1}$	$1.1 \cdot 10^{-1}$	$1.3 \cdot 10^{0}$	$1.4 \cdot 10^{0}$
2	$1.2 \cdot 10^{0}$	$5.3 \cdot 10^{-2}$	$1.1 \cdot 10^{0}$	$1.7 \cdot 10^{0}$
3	$2.1 \cdot 10^{0}$	$3.6 \cdot 10^{-3}$	$8.6 \cdot 10^{-1}$	$2.3 \cdot 10^{0}$
4	$1.2 \cdot 10^{0}$	$7.9 \cdot 10^{-2}$	$1.3 \cdot 10^{1}$	$1.3 \cdot 10^{1}$
5	$3 \cdot 10^{0}$	$1.8 \cdot 10^{-1}$	$4.1 \cdot 10^{0}$	$5.1 \cdot 10^{0}$
6	$1.3 \cdot 10^{0}$	$1.7 \cdot 10^{-1}$	$4.6 \cdot 10^{-1}$	$1.4 \cdot 10^{0}$
7	$1.6 \cdot 10^{0}$	$1 \cdot 10^{-1}$	$7.2 \cdot 10^{0}$	$7.3 \cdot 10^{0}$
8	$5.8 \cdot 10^{-1}$	$2.7 \cdot 10^{-2}$	$3.7 \cdot 10^{-1}$	$6.9 \cdot 10^{-1}$
9	$5 \cdot 10^{-1}$	$7.4 \cdot 10^{-2}$	$6.4 \cdot 10^{-1}$	$8.1 \cdot 10^{-1}$

Table 5.30: P - Strategy A2: Δv values

The Fig. 5.62 underlines the importance of the z-component of the Δv in this new simulation environment.

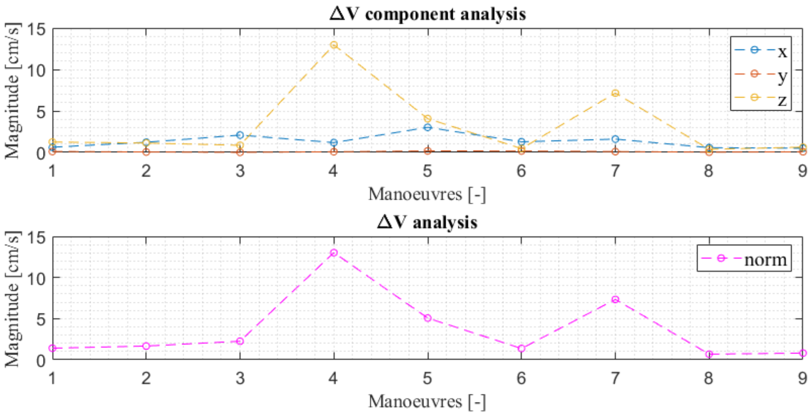

Figure 5.62: P - Strategy A2: behaviour of the Δv

As expected, the inspection phase time increases by inserting the new filter time, that is lower than the previous one.

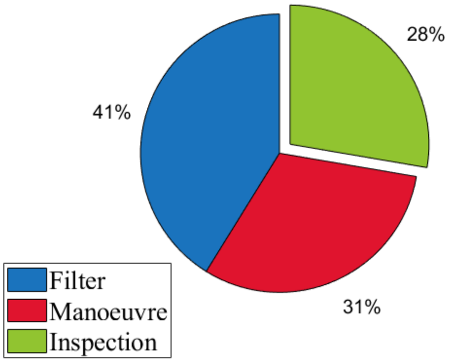

Figure 5.63: P - Strategy A2: percentage of the phases

5.2.4 Filter Analysis 2/2

Now, the conditions presented in Sect. 5.1.4 will introduce, as reported below:

- *minimum phase time*: for the first cycle, the minimum value of time for the convergence of the filter is 3967 s, found in Sect. 5.2.2;
- *error between UKF and nominal orbit*: when the deputy's estimated state from the UKF is way too far from the nominal trajectory given by the HCW, the filter phase will be stopped and a station keeping manoeuvre will be performed to re-position the deputy on the nominal orbit. Also in this case, an error of 5 m has been chosen;
- *maximum size of the covariance*: the covariance size has been limited to 3 m, which is the condition for the convergence of the filter considered in the previous filter analysis of the Sect. 5.2.2;
- *divergence control*: the mean coming from the UKF must be contained inside the associated covariance. In this way, any diverging behaviour of the filter can be suppressed.

5.2.5 Strategy B1

This strategy will use a variable filter, which will stop according to the conditions imposed in Sect. 5.2.4, while the manoeuvre and the inspection phase times will remain fixed, as listed in Tab. 5.31:

Parameter	Value
$\Delta t_{fil,1}$ (s)	3967
Δt_{fil} (s)	*variable*
Δt_{man} (s)	3003
Δt_{insp} (s)	3003

Table 5.31: P - Strategy B1: values of time intervals

The trend in Fig. 5.64 assumes high peaks, that lead to obtain a bad behaviour of covariance.

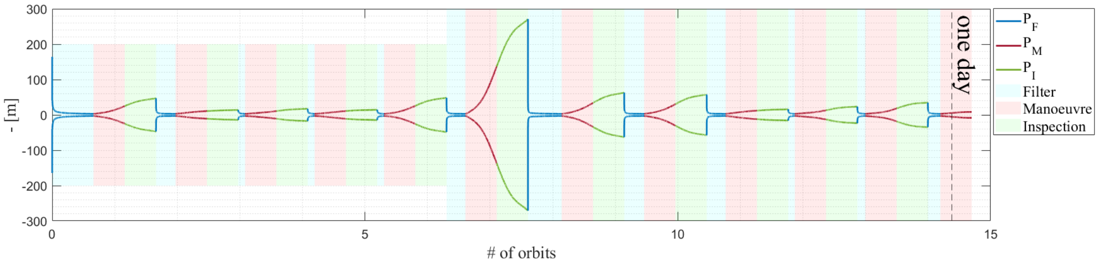

Figure 5.64: P - Strategy B1: behaviour of the covariance

In Fig. 5.65, the errors do not improve, and in the inspection phases the y-component sometimes exits from the covariance limit profile.

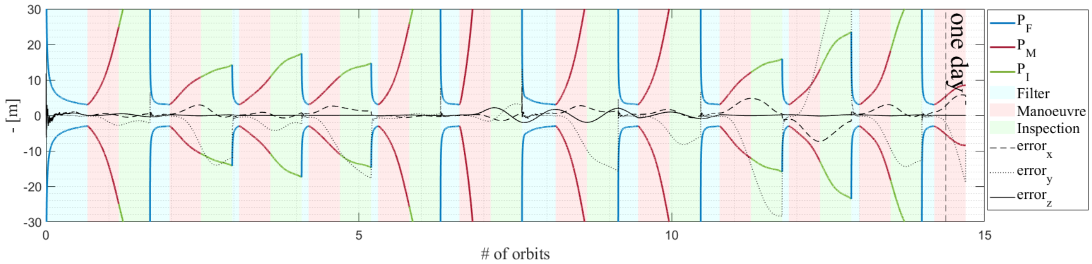

Figure 5.65: P - Strategy B1: behaviour of the error (zoom)

The behaviour of the covariance is affected by the cost of the manoeuvres, where, in this case, they request more Δv than in other strategies, exceeding the upper limit, as Tab. 5.32 and Fig. 5.66 underline. Except for the 6^{th} manoeuvre, the trend of Δv of each burn results linear and regular.

Manoeuvre (#)	Δv_x (cm/s)	Δv_y (cm/s)	Δv_z (cm/s)	$\|\Delta v\|$ (cm/s)
1	$1.1 \cdot 10^{0}$	$9.2 \cdot 10^{-2}$	$4.3 \cdot 10^{0}$	$4.4 \cdot 10^{0}$
2	$3.2 \cdot 10^{-1}$	$1.2 \cdot 10^{-1}$	$9.9 \cdot 10^{-1}$	$1.1 \cdot 10^{0}$
3	$1.3 \cdot 10^{-1}$	$6.6 \cdot 10^{-2}$	$1.5 \cdot 10^{0}$	$1.5 \cdot 10^{0}$
4	$6.8 \cdot 10^{-1}$	$1 \cdot 10^{-1}$	$9.8 \cdot 10^{-1}$	$1.2 \cdot 10^{0}$
5	$8.2 \cdot 10^{-1}$	$9.8 \cdot 10^{-2}$	$4.5 \cdot 10^{0}$	$4.6 \cdot 10^{0}$
6	$7.9 \cdot 10^{-2}$	$3 \cdot 10^{-2}$	$2.6 \cdot 10^{1}$	$2.6 \cdot 10^{1}$
7	$4.5 \cdot 10^{-1}$	$1 \cdot 10^{-1}$	$5.8 \cdot 10^{0}$	$5.8 \cdot 10^{0}$
8	$1 \cdot 10^{0}$	$9.9 \cdot 10^{-2}$	$5.3 \cdot 10^{0}$	$5.4 \cdot 10^{0}$
9	$6.1 \cdot 10^{-1}$	$8.7 \cdot 10^{-2}$	$9.8 \cdot 10^{-1}$	$1.2 \cdot 10^{0}$
10	$1.9 \cdot 10^{0}$	$2.1 \cdot 10^{-1}$	$9.6 \cdot 10^{-1}$	$2.2 \cdot 10^{0}$
11	$3.1 \cdot 10^{0}$	$1.9 \cdot 10^{-1}$	$1.1 \cdot 10^{-1}$	$3.1 \cdot 10^{0}$
12	$5.6 \cdot 10^{-2}$	$1.2 \cdot 10^{-1}$	$3.4 \cdot 10^{-1}$	$3.7 \cdot 10^{-1}$

Table 5.32: P - Strategy B1: Δv values

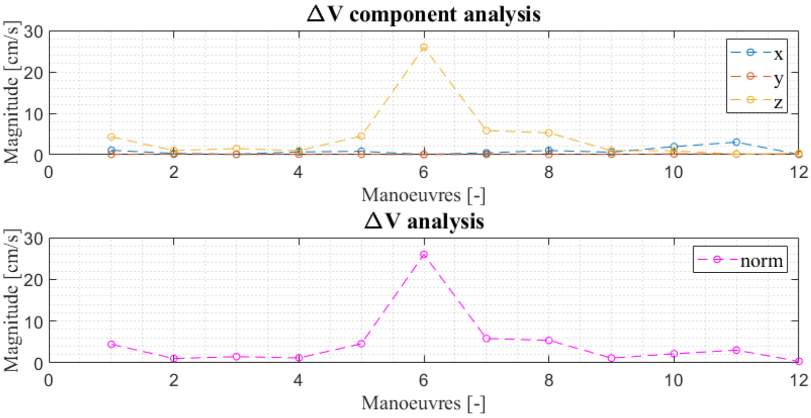

Figure 5.66: P - Strategy B1: behaviour of the Δv

Regarding the total phase time, the inspection earns a lot of time, passing from 28% to 37%, shown in Fig. 5.67. The filter phase time varies a lot during the simulation, as reported in Tab. 5.33.

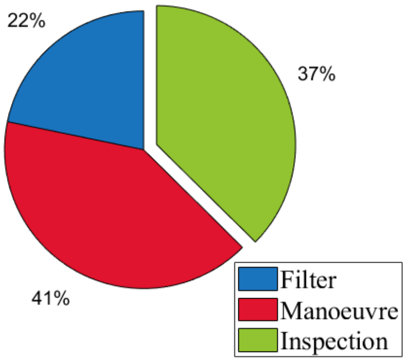

Figure 5.67: P - Strategy B1: percentage of the phases

Cycle	1	2	3	4	5	6	7	8
Δt_{fil} (s)	3968	1881	664	670	654	1809	3236	1912
Cycle	9	10	11	12				
Δt_{fil} (s)	1818	633	767	1194				

Table 5.33: P - Strategy B1: filter phase times

5.2.6 ΔV Analysis

As it can been seen also in the unperturbed case described in Sect. 5.1.6, starting from the results of Fig. 4.4, the Δv analysis has been performed.
To understand better the density of the data in the Sect. 4.4, also here an interpolating function (20^{th} order) has been extrapolated. Then, the median has been evaluated and this value has been considered to be the center value of the interval that will be analyzed afterwards. First of all, the size of the interval is chosen in such a way to include the 99% of the data closed to the median. From here, through observation of the distribution of data, as soon as the time range is widened to the 99.9%, as it can be seen from Fig. 5.68, the interval comprehends ToF$_M$ till 2145 s, which is lower than the previous time of half orbit period. Unlike the Fig. 5.15, the interval of 99.9% can be chosen, due to the fact that this one satisfies the request to reduce the ToF$_M$.

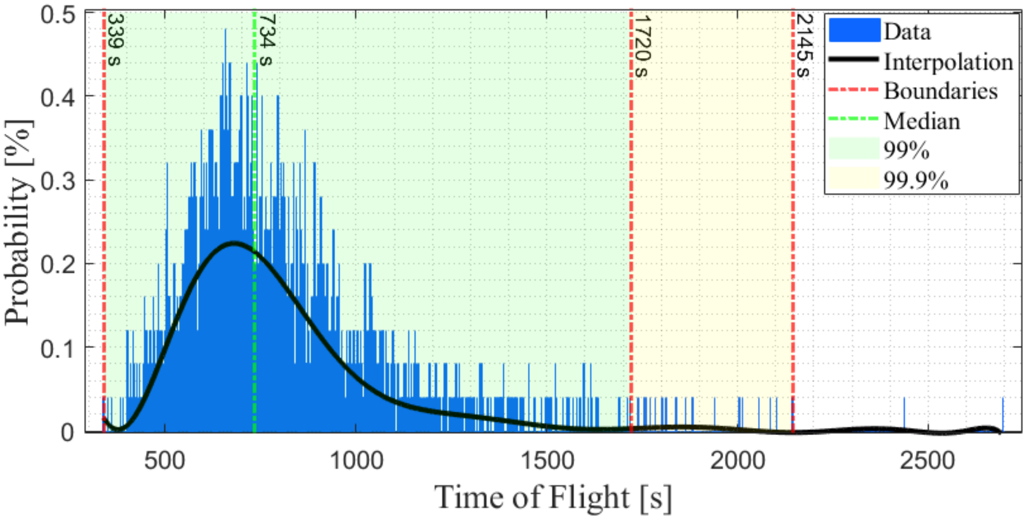

Figure 5.68: P - Density probability of ToF$_M$ extracted from Sect. 4.4

So, lower and upper boundary are, respectively, 339 s and 2145 s, avoiding about 20% of the time considered at the beginning of the analysis, with a median of 734 s. Now, this interval has been divided into 10 values of ToF$_M$ (boundary values included) and these are used in the simulation algorithm. Using the different times, the corresponding total Δv of the mission (over one day) obtained is shown in Fig. 5.69. Each of the cases has been analyzed to guarantee the satisfaction of the maximum Δv_{tot} and the maximum Δv for every single manoeuvre. As the graph shows, the trend tends to stabilize towards increasing ToF$_M$. Starting from this consideration, also in the perturbed case, the results have been customized imposing some upper limits. The red region indicates the values of

Δv_{tot} which are too high compared with the others ($> 80\ cm/s$, where the behaviour of the covariance is also not good), while the green regions indicate the interval that will be further analyzed. Unlike the Fig. 5.16, another zone has been identified and colored in yellow, and it is characterized by the dissatisfaction of the threshold imposed on each Δv component. This area can be considered less severe than the red region, because the Δv_{tot} is comparable with the green region, but in some manoeuvre the components overlap the fixed upper limit.

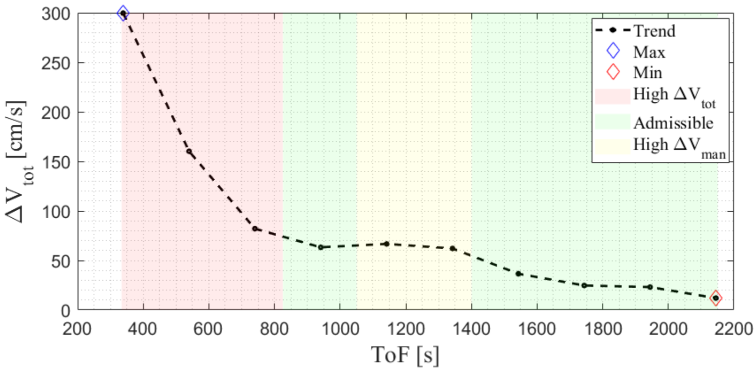

Figure 5.69: P - Δv_{tot} for the 10 values of ToF$_M$ studied

The graphs has 2 green regions, so, they will be analyzed one at a time. The first one has a time interval, that starts from 820 s and reach 1050 s. Divided again into 5 values, the upper values has been excluded to highlight the minimum values. Also here, the yellow regions are present due to high Δv for some manoeuvres.

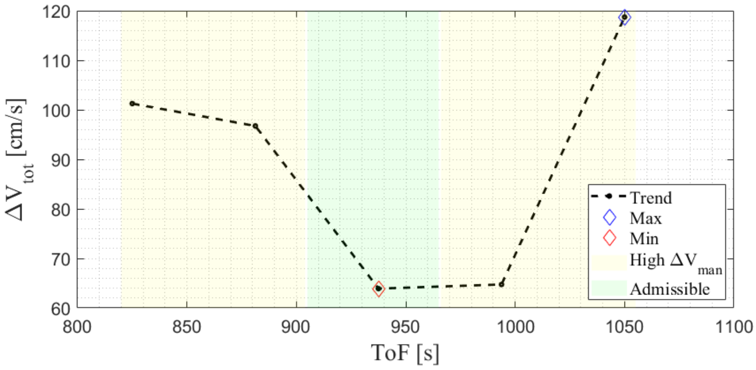

Figure 5.70: P - Δv_{tot} for the 5 values of the first interval studied

Instead, in the second green region, a higher ToF$_M$ interval is highlighted, and the trend of Δv_{tot} decreases at increasing of ToF$_M$. Starting from 1390 s to 2150 s, the area has been divided again into 15 values and, once again, only minimum values that satisfy the conditions have been considered.

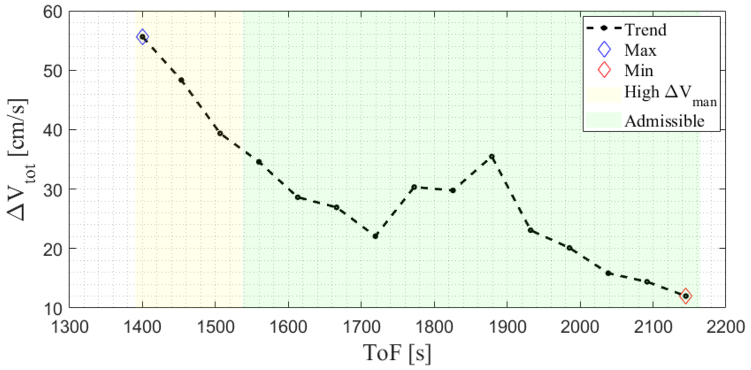

Figure 5.71: P - Δv_{tot} for the 15 values of the second interval studied

From Fig. 5.70 and Fig. 5.71, two ToF$_M$ values have been selected for the next simulations: the one with the minimum Δv_{tot} in the second interval (2145 s) and the one with the minimum Δv_{tot} in the first interval and the best covariance behaviour (938 s) among the values of the green regions.

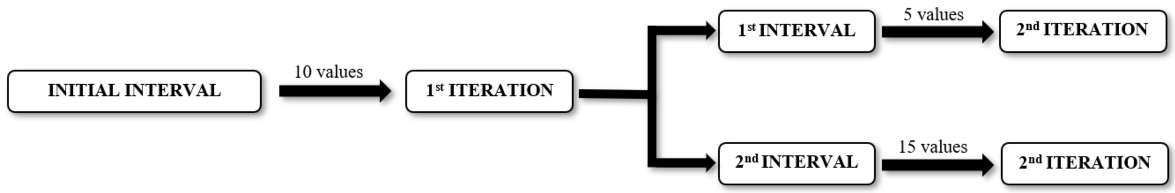

Figure 5.72: P - Δv analysis approach

5.2.7 Strategy B2

Minimum Δv - first interval

The time used in the simulation are listed in Tab. 5.34:

Parameter	Value
$\Delta t_{fil,1}$ (s)	3967
Δt_{fil} (s)	*variable*
Δt_{man} (s)	938
Δt_{insp} (s)	3003

Table 5.34: P - Strategy B2: values of time intervals

In this case, the trend of the covariance is better with respect to the previous one, remaining most of the time in a good range, not exceeding 60 m.

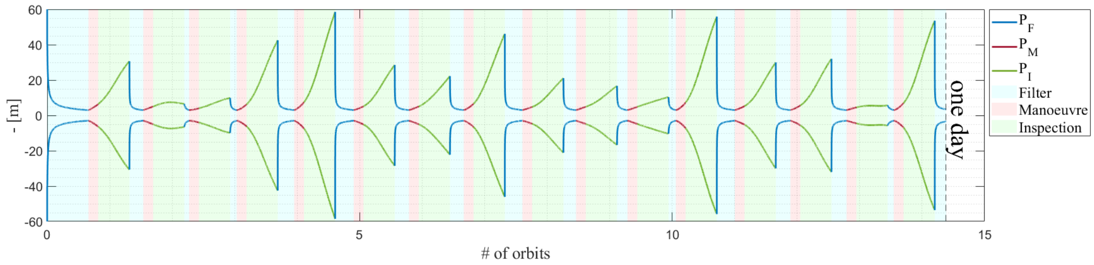

Figure 5.73: P - Strategy B2: behaviour of the covariance

Except for some peaks (due to y-component), the error behaviour in Fig. 5.74 is quite good and some improvements are obtained.

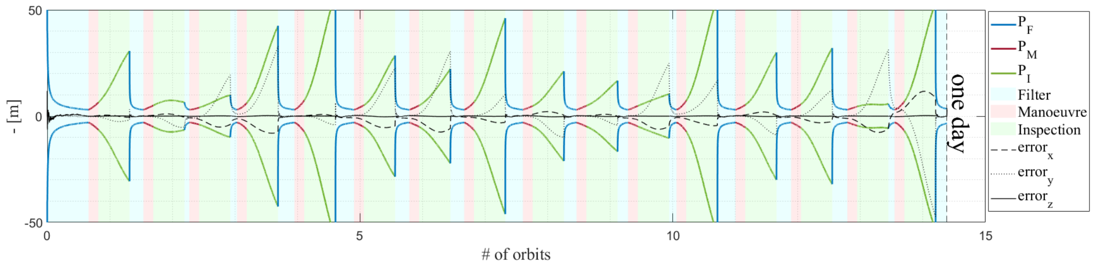

Figure 5.74: P - Strategy B2: behaviour of the error (zoom)

As expected, the cost of the manoeuvres in this strategy remains contained by the choice of ToF$_M$, under 10 cm/s.

Manoeuvre (#)	Δv_x (cm/s)	Δv_y (cm/s)	Δv_z (cm/s)	$\lvert\Delta v\rvert$ (cm/s)
1	$2.7 \cdot 10^{0}$	$2.7 \cdot 10^{0}$	$8.1 \cdot 10^{-2}$	$3.8 \cdot 10^{0}$
2	$3.4 \cdot 10^{-1}$	$2.7 \cdot 10^{-1}$	$1.5 \cdot 10^{-2}$	$4.3 \cdot 10^{-1}$
3	$7.6 \cdot 10^{-1}$	$6.8 \cdot 10^{-1}$	$2.2 \cdot 10^{-2}$	$1 \cdot 10^{0}$
4	$4.2 \cdot 10^{0}$	$4.1 \cdot 10^{0}$	$4.1 \cdot 10^{-2}$	$5.9 \cdot 10^{0}$
5	$6 \cdot 10^{0}$	$5.6 \cdot 10^{0}$	$5.1 \cdot 10^{-2}$	$8.2 \cdot 10^{0}$
6	$2.8 \cdot 10^{0}$	$2.7 \cdot 10^{0}$	$8.8 \cdot 10^{-2}$	$3.9 \cdot 10^{0}$
7	$2.5 \cdot 10^{0}$	$2.4 \cdot 10^{0}$	$1.3 \cdot 10^{-2}$	$3.5 \cdot 10^{0}$
8	$4.9 \cdot 10^{0}$	$4.8 \cdot 10^{0}$	$1.2 \cdot 10^{-2}$	$6.9 \cdot 10^{0}$
9	$2.2 \cdot 10^{0}$	$2.1 \cdot 10^{0}$	$5.8 \cdot 10^{-2}$	$3 \cdot 10^{0}$
10	$1.7 \cdot 10^{0}$	$1.5 \cdot 10^{0}$	$1.3 \cdot 10^{-2}$	$2.3 \cdot 10^{0}$
11	$8.7 \cdot 10^{-1}$	$7.3 \cdot 10^{-1}$	$1.2 \cdot 10^{-2}$	$1.1 \cdot 10^{0}$
12	$5.5 \cdot 10^{0}$	$5.3 \cdot 10^{0}$	$1.8 \cdot 10^{-2}$	$7.6 \cdot 10^{0}$
13	$2.9 \cdot 10^{0}$	$2.7 \cdot 10^{0}$	$8 \cdot 10^{-2}$	$4 \cdot 10^{0}$
14	$3.2 \cdot 10^{0}$	$3.1 \cdot 10^{0}$	$1.5 \cdot 10^{-2}$	$4.5 \cdot 10^{0}$
15	$5 \cdot 10^{-1}$	$3.5 \cdot 10^{-1}$	$1.7 \cdot 10^{-2}$	$6.1 \cdot 10^{-1}$
16	$5.2 \cdot 10^{0}$	$5 \cdot 10^{0}$	$3.6 \cdot 10^{-2}$	$7.2 \cdot 10^{0}$

Table 5.35: P - Strategy B2: Δv values

Each Δv component satisfies the limit condition of 10 cm/s, and the z-component returned to have the smallest contribution of them.

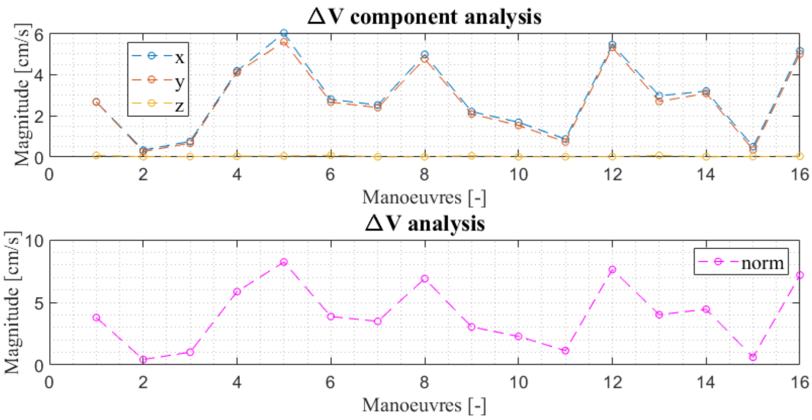

Figure 5.75: P - Strategy B2: behaviour of Δv

From Fig. 5.10, the inspection time makes a big leap forward, achieving 55% of the entire simulation, as Fig. 5.76 shows. The choice to select a small ToF_M had a big contribution to the maximization of the inspection time. Also, the variable filter stays under the first fixed time, reducing the total time, as shown in Tab. 5.36.

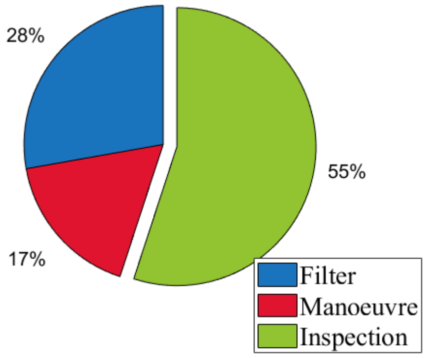

Figure 5.76: P - Strategy B2: percentage of the phases

Cycle	1	2	3	4	5	6	7	8
Δt_{fil} (s)	3968	1329	464	640	1575	1785	1365	1328
Cycle	9	10	11	12	13	14	15	16
Δt_{fil} (s)	1695	1211	1008	699	1729	1408	1452	1096

Table 5.36: P - Strategy B2: filter phase times

Minimum Δv - second interval

On the other hand, selecting the second time of flight from the analysis, as reported in Tab. 5.37, the results are the following.

Parameter	Value
$\Delta t_{fil,1}$ (s)	3967
Δt_{fil} (s)	*variable*
Δt_{man} (s)	938
Δt_{insp} (s)	3003

Table 5.37: P - Strategy B2: values of time intervals

The covariance assumes values even smaller, staying under 30 m, half the value of the previous case.

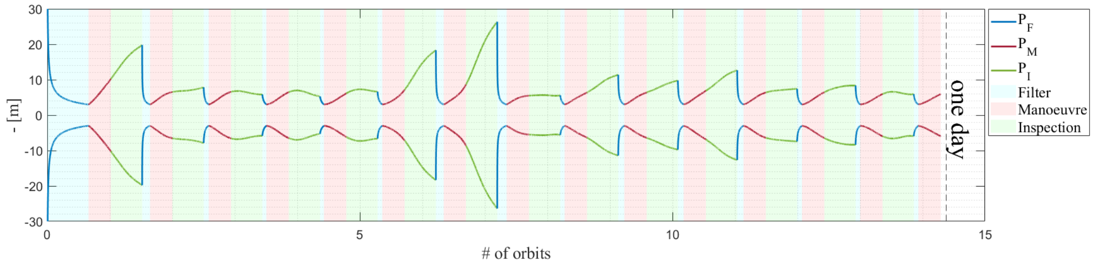

Figure 5.77: P - Strategy B2: behaviour of the covariance

In Fig. 5.78, the error exiting from the limits is still too evident.

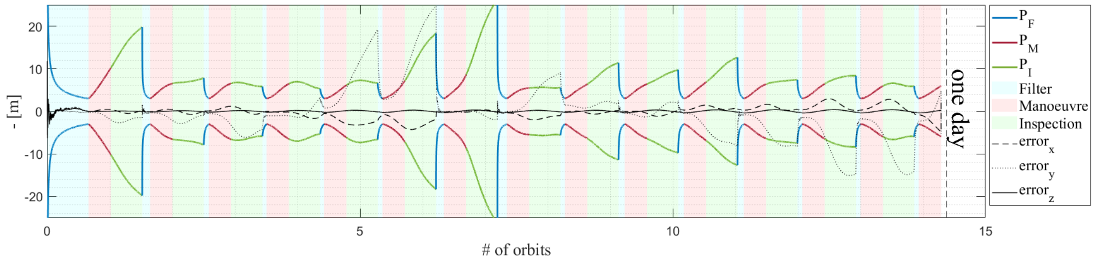

Figure 5.78: P - Strategy B2: behaviour of the error (zoom)

In according to the new ToF_M, the Δv decreases, making this strategy one of the less expensive, as Tab. 5.38 and Fig. 5.79 report.

Manoeuvre (#)	Δv_x (cm/s)	Δv_y (cm/s)	Δv_z (cm/s)	$\lvert\Delta v\rvert$ (cm/s)
1	$1.6 \cdot 10^{0}$	$4.8 \cdot 10^{-1}$	$6.9 \cdot 10^{-2}$	$1.7 \cdot 10^{0}$
2	$4.9 \cdot 10^{-1}$	$1.4 \cdot 10^{-1}$	$2.1 \cdot 10^{-2}$	$5.2 \cdot 10^{-1}$
3	$2.3 \cdot 10^{-1}$	$6 \cdot 10^{-2}$	$1.4 \cdot 10^{-2}$	$2.4 \cdot 10^{-1}$
4	$2 \cdot 10^{-1}$	$5 \cdot 10^{-2}$	$1.3 \cdot 10^{-2}$	$2.1 \cdot 10^{-1}$
5	$4.1 \cdot 10^{-1}$	$9 \cdot 10^{-2}$	$1.6 \cdot 10^{-2}$	$4.2 \cdot 10^{-1}$
6	$1.7 \cdot 10^{0}$	$3.8 \cdot 10^{-1}$	$1.3 \cdot 10^{-2}$	$1.7 \cdot 10^{0}$
7	$2.5 \cdot 10^{0}$	$5.7 \cdot 10^{-1}$	$9.6 \cdot 10^{-3}$	$2.6 \cdot 10^{0}$
8	$3.8 \cdot 10^{-2}$	$7.5 \cdot 10^{-2}$	$1 \cdot 10^{-2}$	$8.5 \cdot 10^{-2}$
9	$9.8 \cdot 10^{-1}$	$2.9 \cdot 10^{-1}$	$5.8 \cdot 10^{-3}$	$1 \cdot 10^{0}$
10	$7.2 \cdot 10^{-1}$	$2.2 \cdot 10^{-1}$	$2.1 \cdot 10^{-2}$	$7.5 \cdot 10^{-1}$
11	$1 \cdot 10^{0}$	$2.9 \cdot 10^{-1}$	$1.4 \cdot 10^{-2}$	$1.1 \cdot 10^{0}$
12	$3.1 \cdot 10^{-1}$	$1.3 \cdot 10^{-1}$	$1.7 \cdot 10^{-2}$	$3.3 \cdot 10^{-1}$
13	$4.3 \cdot 10^{-1}$	$1.2 \cdot 10^{-1}$	$1 \cdot 10^{-2}$	$4.4 \cdot 10^{-1}$
14	$3.2 \cdot 10^{-1}$	$4.4 \cdot 10^{-2}$	$6.3 \cdot 10^{-3}$	$3.2 \cdot 10^{-1}$
15	$5.8 \cdot 10^{-1}$	$2 \cdot 10^{-1}$	$6.4 \cdot 10^{-3}$	$6.2 \cdot 10^{-1}$

Table 5.38: P - Strategy B2: Δv values

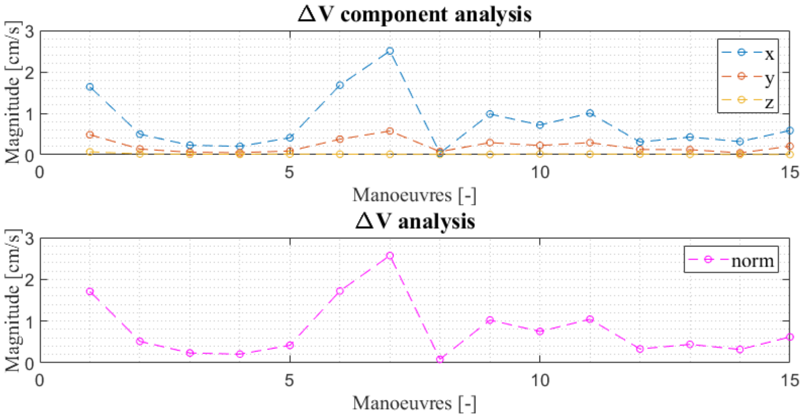

Figure 5.79: P - Strategy B2: behaviour of the Δv

Overall the strategy gains inspection time, but not as much as the previous strategy, due to the bigger ToF$_M$.

Cycle	1	2	3	4	5	6	7	8
Δt_{fil} (s)	3967	762	489	393	382	456	747	904
Cycle	9	10	11	12	13	14	15	
Δt_{fil} (s)	423	583	552	605	472	443	443	

Table 5.39: P - Strategy B2: filter phase times

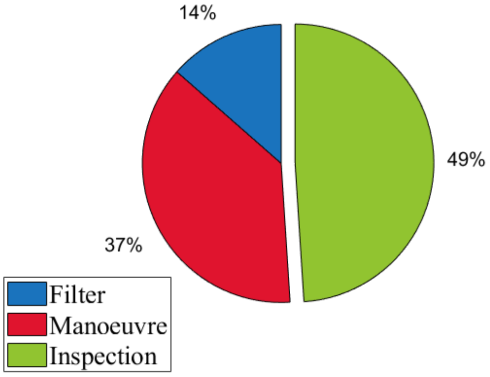

Figure 5.80: P - Strategy B2: percentage of the phases

5.2.8 Manoeuvre Analysis

Again, following the same steps of the Sect. 5.1.8, the new minimization problem is introduced, selecting the boundary from the previous Δv analysis, as reported in Tab. 5.40. The interval has been chosen including the yellow region to include both the green interval and the guess for the TOF_M has been selected from the first green interval because it is the lowest value.

Parameter	Value
ToF_{min} (s)	820
ToF_{max} (s)	2150
$\Delta v_{i,j}$ (cm/s)	10
$\Delta v_{f,j}$ (cm/s)	10
ToF_{guess} (s)	983
$\Delta v_{i,j,guess}$ (cm/s)	10^{-2}

Table 5.40: P - Boundary constrains of the minimization problem

where the apex j points each component of the vector considered, meanwhile i and f mean, respectively, initial and final time.

5.2.9 Strategy C1

This strategy will implement the new minimization problem, in order to vary the manoeuvre time.

Parameter	Value
$\Delta t_{fil,1}$ (s)	3967
Δt_{fil} (s)	*variable*
Δt_{man} (s)	*variable*
Δt_{insp} (s)	3003

Table 5.41: P - Strategy C1: values of time intervals

Similar to the previous strategy, the trend of the covariance shown in Fig. 5.81 seems good, despite some high values that remains under 50 m.

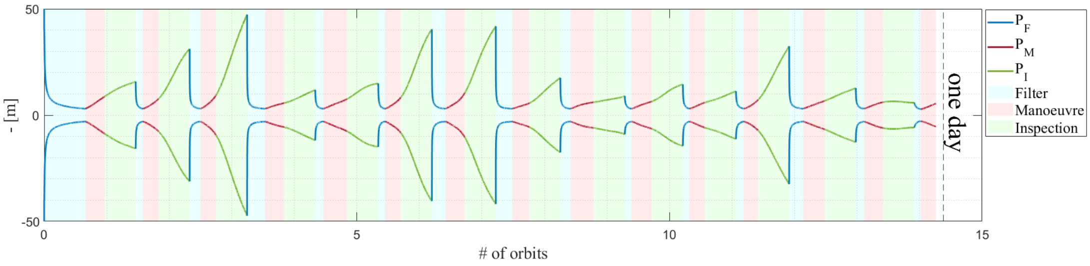

Figure 5.81: P - Strategy C1: behaviour of the covariance

The error is affected by the usual effect on y-component, leading to the behaviour shown in Fig. 5.82.

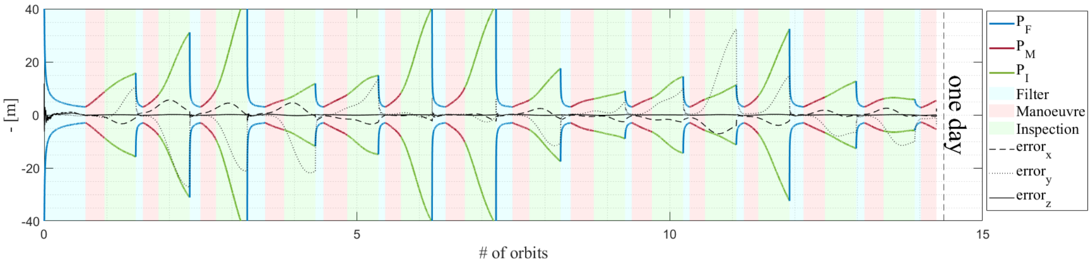

Figure 5.82: P - Strategy C1: behaviour of the error

From the behaviour of the covariance, the manoeuvres does not seem too much expensive, and this is proven by Tab. 5.42. All the values remain in the upper limit of 10 cm/s.

Manoeuvre (#)	Δv_x (cm/s)	Δv_y (cm/s)	Δv_z (cm/s)	$\lvert\Delta v\rvert$ (cm/s)
1	$1.3 \cdot 10^0$	$5.6 \cdot 10^{-1}$	$7.5 \cdot 10^{-2}$	$1.4 \cdot 10^0$
2	$2.8 \cdot 10^0$	$1.4 \cdot 10^0$	$1.9 \cdot 10^{-2}$	$3.1 \cdot 10^0$
3	$4.9 \cdot 10^0$	$2.5 \cdot 10^0$	$2.3 \cdot 10^{-2}$	$5.5 \cdot 10^0$
4	$1.1 \cdot 10^0$	$4.2 \cdot 10^{-1}$	$9.3 \cdot 10^{-2}$	$1.2 \cdot 10^0$
5	$1.1 \cdot 10^0$	$2.7 \cdot 10^{-1}$	$9.1 \cdot 10^{-3}$	$1.2 \cdot 10^0$
6	$3.7 \cdot 10^0$	$1.9 \cdot 10^0$	$6.2 \cdot 10^{-2}$	$4.1 \cdot 10^0$
7	$4.1 \cdot 10^0$	$1.5 \cdot 10^0$	$1.2 \cdot 10^{-1}$	$4.4 \cdot 10^0$
8	$1.7 \cdot 10^0$	$8.4 \cdot 10^{-1}$	$6.5 \cdot 10^{-2}$	$1.9 \cdot 10^0$
9	$8.1 \cdot 10^{-1}$	$2.2 \cdot 10^{-1}$	$1.5 \cdot 10^{-1}$	$8.5 \cdot 10^{-1}$
10	$1.2 \cdot 10^0$	$3.1 \cdot 10^{-1}$	$8.7 \cdot 10^{-2}$	$1.2 \cdot 10^0$
11	$1 \cdot 10^0$	$4.7 \cdot 10^{-1}$	$2.8 \cdot 10^{-2}$	$1.1 \cdot 10^0$
12	$3.4 \cdot 10^0$	$2.1 \cdot 10^0$	$4.6 \cdot 10^{-2}$	$4 \cdot 10^0$
13	$1.2 \cdot 10^0$	$4.8 \cdot 10^{-1}$	$3.6 \cdot 10^{-2}$	$1.3 \cdot 10^0$
14	$3 \cdot 10^{-1}$	$9.7 \cdot 10^{-2}$	$6.1 \cdot 10^{-2}$	$3.2 \cdot 10^{-1}$
15	$3.8 \cdot 10^{-1}$	$2.4 \cdot 10^{-1}$	$1.4 \cdot 10^{-2}$	$4.5 \cdot 10^{-1}$

Table 5.42: P - Strategy C1: Δv values

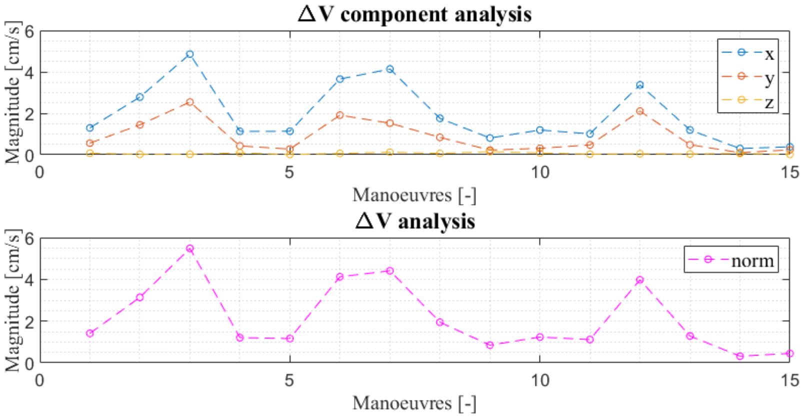

Figure 5.83: P - Strategy C1: behaviour of Δv

Unfortunately, the inspection time did not gain further advantages with respect to the previous strategy. This similar result is obtained also in the unperturbed case, where, also there, the strategies B seem better than the autonomous one.

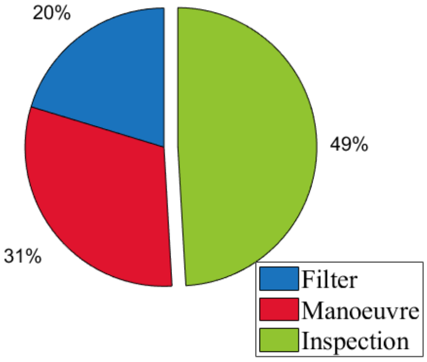

Figure 5.84: P - Strategy C1: percentage of the phases

Finally, as soon as the behaviour of the covariance tends to be smaller and stable, the filter phase time decreases, while for the manoeuvres it can be seen a constant trend in Tab. 5.43.

Cycle	1	2	3	4	5	6	7	8
Δt_{fil} (s)	3968	683	1031	1712	779	649	1288	1581
Δt_{man} (s)	1826	1494	1490	1826	2272	1500	1847	1613
Cycle	9	10	11	12	13	14	15	
Δt_{fil} (s)	975	652	614	730	1344	791	601	
Δt_{man} (s)	2210	1928	1482	1378	2051	1825	1482	

Table 5.43: P - Strategy C1: phase times

5.2.10 Inspection phase analysis

For what concern the inspection phase, the same conditions of Sect. 5.1.10 has been introduced to vary the inspection phase. In fact, from the validation of the models in Sect. 2.5, the same bands of the unperturbed case has been kept, as shown in Fig. 5.85. The bands indicates the stopping zones of the inspection phase, in order to make a favourable manoeuvre when the error is lower. In particular, the bands are positioned before a depression of the x-component error, while the y-component is more difficult to control. Again, the area dedicated for the final part of the inspection are, respectively, at 1/3 (about 2000 s) and at 5/6 (about 5000 s) of the nominal orbit.

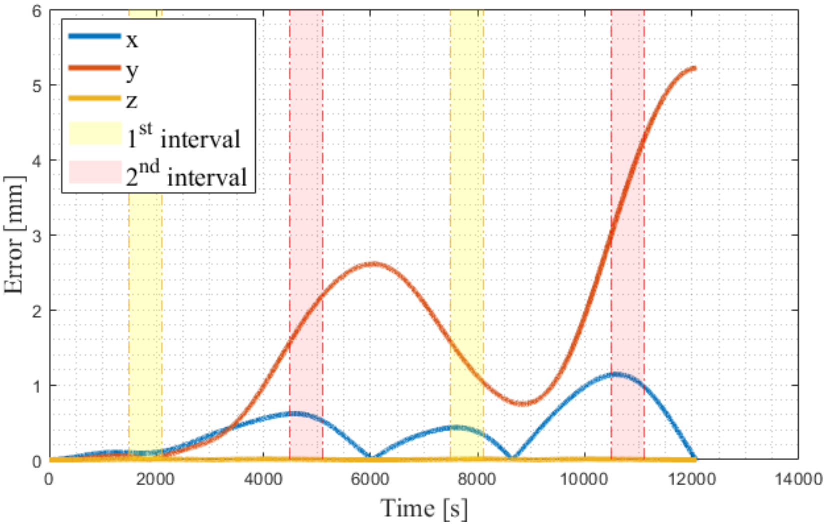

Figure 5.85: P - HCW-NERM$_{J_2}$ comparison

5.2.11 Strategy D1

In this strategy, that is defined as "autonomous" due to the addition of the condition imposed in Sect. 5.2.10, the values of time used are shown in Tab. 5.44.

Parameter	Value
$\Delta t_{fil,1}$ (s)	3967
Δt_{fil} (s)	*variable*
Δt_{man} (s)	*variable*
Δt_{insp} (s)	*variable*

Table 5.44: P - Strategy D1: values of time intervals

It can be seen that the behaviour of the covariance is quite good. At the beginning of Fig. 5.86, the algorithm tries to find a stability, that is obtained only in the second half of the simulation.

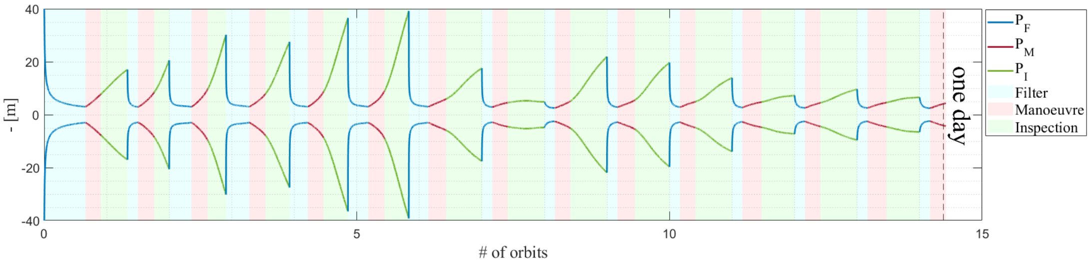

Figure 5.86: P - Strategy D1: behaviour of the covariance

Unfortunately, Fig. 5.87 shows that y-component does not reenter in the covariance limit, but this strategy can be defined as the best one in terms of the covariance and error behaviours.

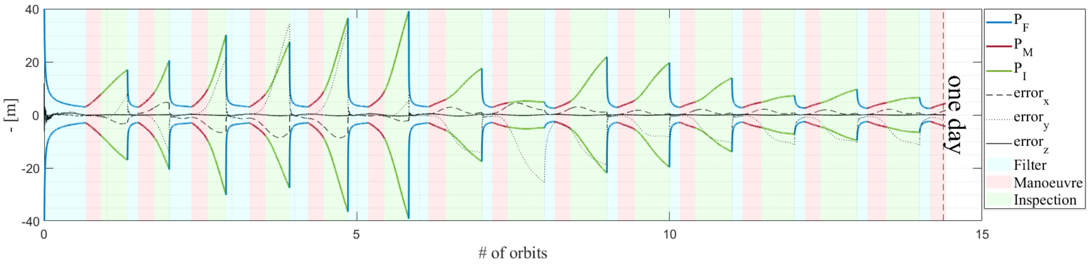

Figure 5.87: P - Strategy D1: behaviour of the error

The absence of peaks in Fig. 5.86 means that every manoeuvres satisfies the Δv boundaries imposed as proved by Tab. 5.45 and Fig. 5.88. Also, the higher values are in the first half of the simulation as expected.

Manoeuvre (#)	Δv_x (cm/s)	Δv_y (cm/s)	Δv_z (cm/s)	$\|\Delta v\|$ (cm/s)
1	$1.6 \cdot 10^0$	$9.4 \cdot 10^{-1}$	$7.6 \cdot 10^{-2}$	$1.8 \cdot 10^0$
2	$2.9 \cdot 10^0$	$1.4 \cdot 10^0$	$2.4 \cdot 10^{-2}$	$3.3 \cdot 10^0$
3	$4.2 \cdot 10^0$	$1.9 \cdot 10^0$	$1.7 \cdot 10^{-2}$	$4.6 \cdot 10^0$
4	$3.4 \cdot 10^0$	$1.6 \cdot 10^0$	$3.5 \cdot 10^{-2}$	$3.7 \cdot 10^0$
5	$4.5 \cdot 10^0$	$2.2 \cdot 10^0$	$3.7 \cdot 10^{-2}$	$5 \cdot 10^0$
6	$4.7 \cdot 10^0$	$1.9 \cdot 10^0$	$1.4 \cdot 10^{-1}$	$5.1 \cdot 10^0$
7	$1.5 \cdot 10^0$	$5.7 \cdot 10^{-1}$	$7.3 \cdot 10^{-2}$	$1.6 \cdot 10^0$
8	$8.3 \cdot 10^{-2}$	$5.3 \cdot 10^{-2}$	$9.9 \cdot 10^{-2}$	$1.4 \cdot 10^{-1}$
9	$2 \cdot 10^0$	$1 \cdot 10^0$	$3.7 \cdot 10^{-2}$	$2.3 \cdot 10^0$
10	$1.8 \cdot 10^0$	$6.4 \cdot 10^{-1}$	$4.1 \cdot 10^{-2}$	$1.9 \cdot 10^0$
11	$1.2 \cdot 10^0$	$6.1 \cdot 10^{-1}$	$7.2 \cdot 10^{-2}$	$1.3 \cdot 10^0$
12	$5.5 \cdot 10^{-1}$	$1.6 \cdot 10^{-1}$	$2.6 \cdot 10^{-2}$	$5.7 \cdot 10^{-1}$
13	$7.9 \cdot 10^{-1}$	$3.8 \cdot 10^{-1}$	$8.3 \cdot 10^{-3}$	$8.8 \cdot 10^{-1}$
14	$4.7 \cdot 10^{-1}$	$1.8 \cdot 10^{-1}$	$5.6 \cdot 10^{-2}$	$5.1 \cdot 10^{-1}$
15	$3.5 \cdot 10^{-1}$	$2.6 \cdot 10^{-1}$	$1.1 \cdot 10^{-1}$	$4.5 \cdot 10^{-1}$

Table 5.45: P - Strategy D1: Δv values

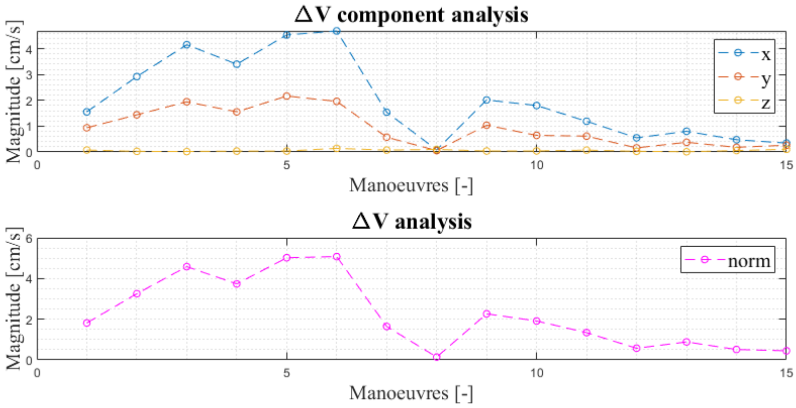

Figure 5.88: P - Strategy D1: behaviour of Δv

Unlike the unperturbed case, Fig. 5.89 shows that the inspection phase time cannot compete against the strategy B2, which remains at 46% of the total simulation time.

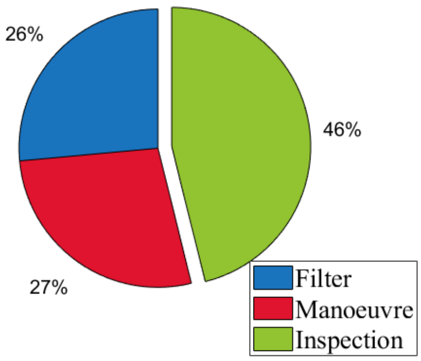

Figure 5.89: P - Strategy D1: percentage of the phases

As it happens in other strategies, the second half of simulation time tends to follow a cycle with duration equal to one orbit time. For this reasons, the time of the phases result little variable, as Tab. 5.46 shows.

Cycle	1	2	3	4	5	6	7	8
Δt_{fil} (s)	3968	1001	2141	2234	1752	1943	1873	1001
Δt_{man} (s)	1485	1568	1558	1552	1510	1572	1706	1481
Δt_{insp} (s)	2555	1436	1759	2319	2346	2330	3440	3525
Cycle	9	10	11	12	13	14	15	
Δt_{fil} (s)	997	1003	1005	999	1004	996	1005	
Δt_{man} (s)	1484	1693	1482	1826	1482	1826	1515	
Δt_{insp} (s)	3522	3313	3524	3180	3524	3180		

Table 5.46: P - Strategy D1: phase times

5.2.12 Strategy D2

Let's take a step back again. As in Sect. 5.1.12, the strategy B2 is modified introducing the conditions explained in Sect. 5.2.10 to make variable the inspection phase time. Both of the values of ToF_M used in the strategy B2 will be analyzed to understand if this choice can give advantages with respect to the autonomous case.

Minimum Δv_{tot} - first interval

Selecting the ToF_M of Sect. 5.2.7, as reported in Tab. 5.47, the results are the following.

Parameter	Value
$\Delta t_{fil,1}$ (s)	3967
Δt_{fil} (s)	*variable*
Δt_{man} (s)	938
Δt_{insp} (s)	*variable*

Table 5.47: P - Strategy D2: values of time intervals

In Fig. 5.90, it can be noticed that this strategy mission cannot be chosen and performed. At the beginning, the algorithm offers some inspection phases, but during the simulation this phase is deleted. This phenomenon is due mainly to the expensive manoeuvres, that lead to remove any inspection phases from the 6^{th} cycle, where Δt_{insp} does not exist, because the stopping conditions result already satisfied from the first time instant of the phase.

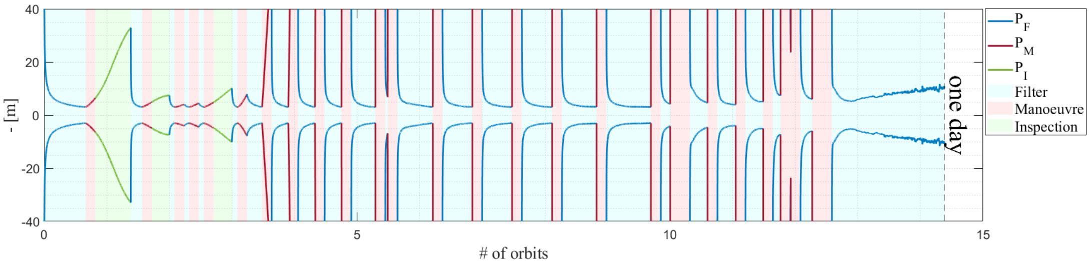

Figure 5.90: P - Strategy D2: behaviour of the covariance

Briefly, Fig. 5.91 reports also that the trend of Δv grows to reach unfeasible values, passing from the order of cm/s to thousands of km/s.

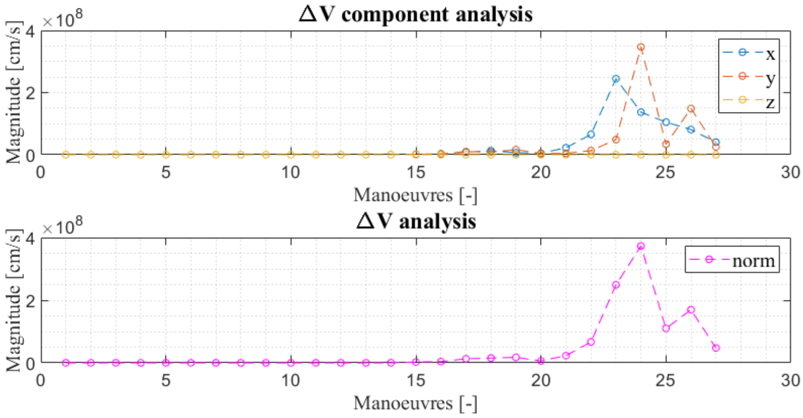

Figure 5.91: P - Strategy D2: behaviour of the Δv

Accordingly, this strategy must be discard and will not be exposed in the strategy comparison in Sect. 5.2.13.

Minimum Δv_{tot} - second interval

Unfortunately, changing the ToF$_M$ as in Sect. 5.2.7, reported in Tab. 5.48, the behaviour of the covariance in Fig. 5.92 does not provide good results, similar to the previous case. In fact, also here, the reasons of this "explosion" is due to the cost of manoeuvres, that tends to increase during the simulation time.

Parameter	Value
$\Delta t_{fil,1}$ (s)	3967
Δt_{fil} (s)	*variable*
Δt_{man} (s)	2145
Δt_{insp} (s)	*variable*

Table 5.48: P - Strategy D2: values of time intervals

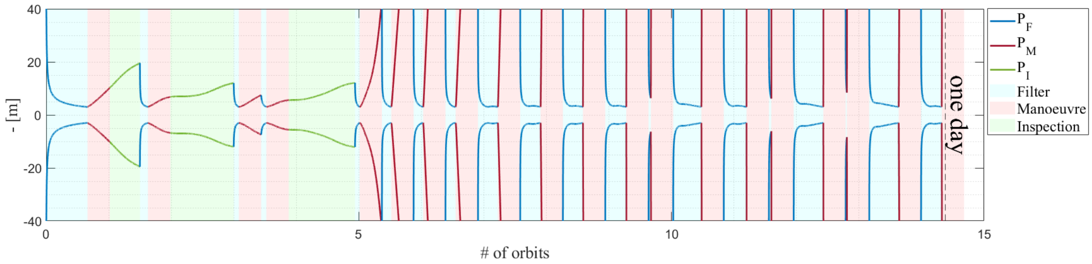

Figure 5.92: P - Strategy D2: behaviour of the covariance

Again, in Fig. 5.93, the behaviour of the Δv is characterized by good values (as it can be seen also in the above plot) at the beginning until the 5^{th} cycle, where the algorithm does not offer more feasible manoeuvres, reaching orders of tens of m/s.

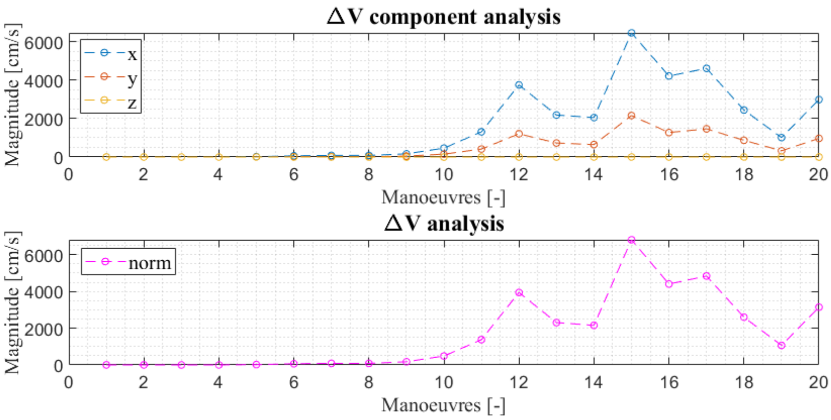

Figure 5.93: P - Strategy D2: behaviour of the Δv

In conclusion, also this strategy is discarded and will not be considered in the final results section.

5.2.13 Resume

At the end of the presentation of the perturbed strategies, a comparison between the total inspection time and the total cost in terms of Δv has been made for each of them. Figure 5.94 shows the result. The total region has been divided into 4 quadrants, as in Sect. 5.1.13, and the color of the marker indicates the quality of the algorithm, in terms of the behaviour of the covariance and the associated error.
Considering the right side of the graph, the blue one laying in the upper area, $B2_{1st}$ is the best in terms of inspection time, but the behaviour of the error and the high total cost lead to discard it. Then, in the green region, $B2_{2nd}$ and C1 are better than D1, because they spend Δv_{tot} with a similar inspection time, but they have the same problem of $B2_{1st}$. So, D1 could be defined as the unique strategy that satisfies all parameters defined in Sect. 4.2. Another aspect to consider is also the degree of autonomy: in fact, the strategy D1 can be considered fully autonomous and, since the cost and the inspection time are similar to the ones with lower degree of autonomy, this can be considered the best strategy.

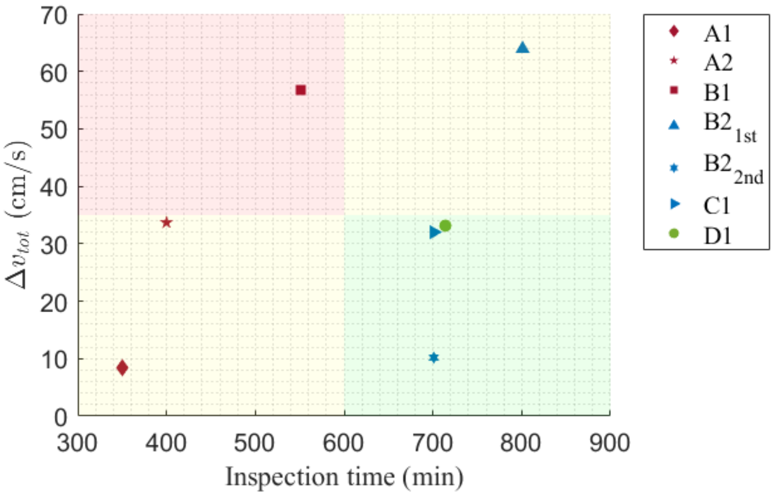

Figure 5.94: P - Comparison of the different strategies

5.2.14 Visibility analysis

Following the idea of Sect. 5.1.14, the green strategies in the green region marked before should be analyzed, but, due to the problem about the error between GUT estimation and the NERM state, not all of them will be taken into account. Specifically, the strategy C1 has been discarded. Now, Envisat will be considered as a tumbling object, so the measurement model has been updated following the steps shown in Sect. 3.3. Then, the visibility, in the sense of what face is seen and for how many seconds, has been analyzed. The results for both strategies are shown below, while the initial conditions are reported in Sect. 4.3.

Strategy B2 - Minimum Δv_{tot} - second interval

Figure 5.95 reports for how much time in seconds each face is seen by the deputy, assuming that the camera is always pointed towards the center of mass of the target. With respect to Fig. 5.95a, the Fig. 5.95b shows an increasing in the faces 2 and 3, and a decreasing in the other faces. In particular, the inspection of the fixed target may occur almost always on the part of the nominal orbit from which the faces 1, 4, 5 are visible. Also, in the case of tumbling target, the distribution of the visible faces is more sparse than in the case of fixed target. Specifically, there is an higher visibility during each inspection phase, while for the case of fixed target, there is the possibility that one or more of the faces are not visible during some phases.

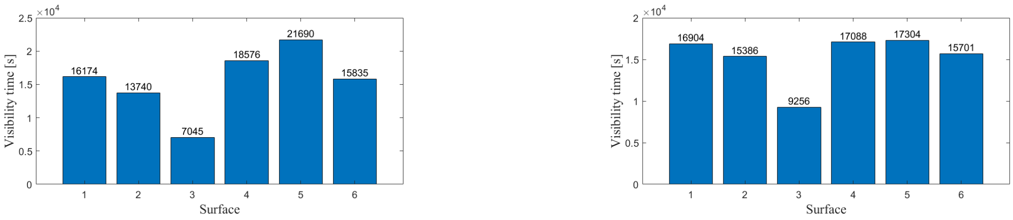

(a) Fixed target

(b) Tumbling target

Figure 5.95: P - Strategy B2: visibility time for each of the face

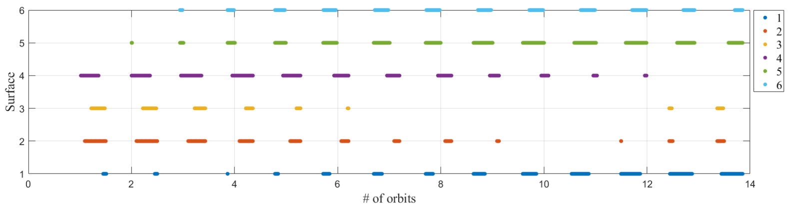

(a) Fixed target

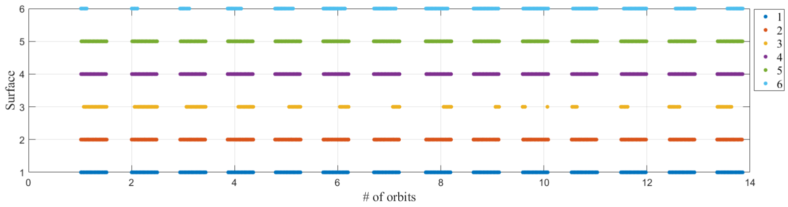

(b) Tumbling target

Figure 5.96: P - Strategy B2: visibility in time for each of the face

Strategy D1

Instead, for this strategy, the distribution of the visible faces results irregular as Fig. 5.97a shows, where faces 2, 3, 4 are characterized by a poor visibility, while faces 1, 5 and 6 obtain good results. Passing from a fixed target configuration to a tumbling target configuration, the trend changes, improving the situation of the overall visibility, but maintaining the irregular behaviour.
As shown in Fig. 5.98, in the fixed case, only some faces have the possibility to be inspected with some regularity, while for the case of tumbling target, Fig. 5.98b shows a sort of continuity until almost the end of the simulation.

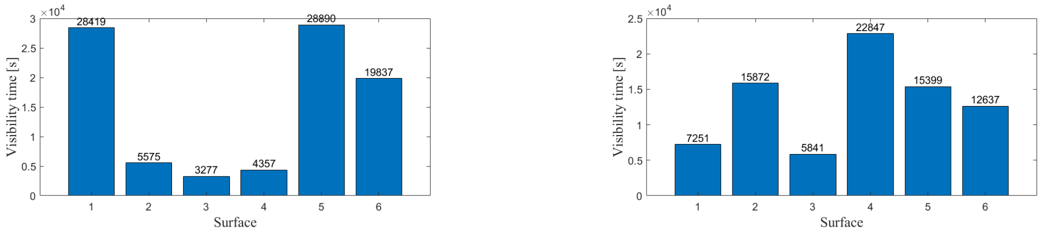

(a) Fixed target (b) Tumbling target

Figure 5.97: P - Strategy D1: visibility time for each of the face

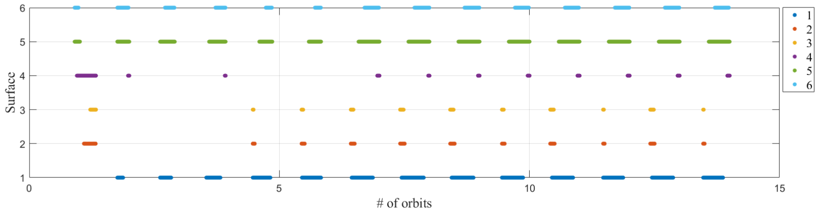

(a) Fixed target

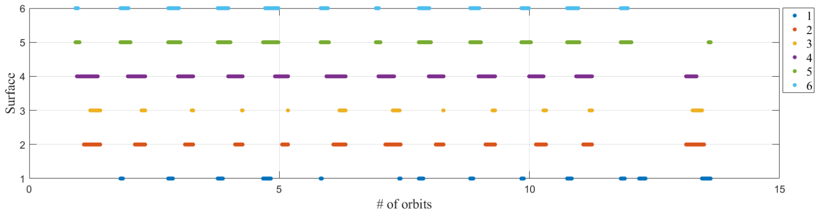

(b) Tumbling target

Figure 5.98: P - Strategy D1: visibility in time for each of the face

In conclusion, as presented in Sect. 5.1.14, a final analysis on the visibility time of each faces during the 10.5 hours of inspection has been carried out. As it can be seen, in the strategy B2, there is an improvement on the overall visibility in the tumbling configuration, reaching a minimum of 2.4 hours for each of the faces, instead of 1.8 hours for the fixed configuration. On the contrary, for the strategy D1, there is not a big difference and some faces cannot be inspected for too long (almost an hour) in a one day mission.

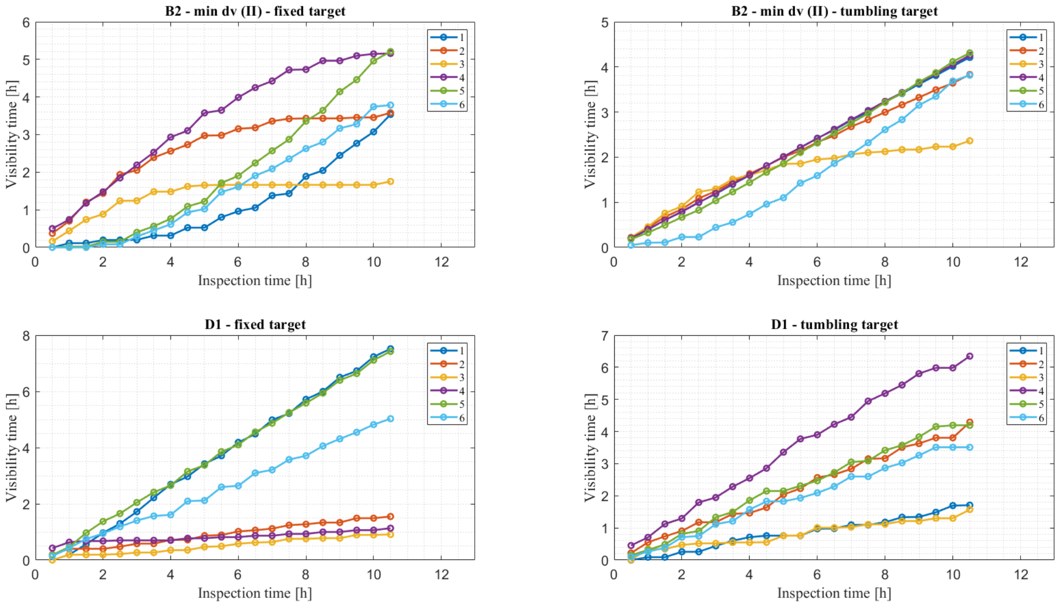

Figure 5.99: P - Visibility time vs inspection time for each of the strategy

Chapter 6

Inclined Football Orbit Mission

6.1 Strategy E

In this chapter, following the analysis about the planning of the inspection mission on a single nominal orbit, the focus moves on an alternative idea. Taking into account the theory of *inclined football orbit*, described in Sect. 2.3.2, the aim is to generate a strategy changing the nominal orbit in such a way to increase the quality of the inspection mission, avoiding to increase the Δv_{tot} and the size of the initial nominal orbit (adopting in the other strategies) as much as possible. In respect of the previous chapter, the adoption of this kind of relative orbit should bring benefits, for the possibility to move more also along the 3^{rd} axis $\hat{h}$, rarely considered until now. Specifically, this coordinate is managed by α, while β indicates the highest and lowest of the orbit. Varying this parameter around $\hat{h}$, the distance between the target and the two points remains constant. This aspect cohabits with its disadvantage: the reduction of the size of the orbit.

6.1.1 Size of the relative orbit

As it has already mentioned, if one of the goals is to maintain or try to stay near the reference orbit, a method to exploit these angles shall be found. To do that, the 3^{rd} coordinate of this kinematic model, ρ, can be used to understand the behaviour of the combination between the angles.

For this treatment and the objective of the inspection mission, considering also the simulation environment described before, an analysis can be applied to search the best inclined orbits. To do that, define a range of ρ, α and β, as follow:

- $\rho = 65 \leftrightarrow 95$ m
- α = -90° $\leftrightarrow$ 90°
- β = 0° $\leftrightarrow$ 180°

A constraint is selected: the inclined orbits shall not enter in a sphere (of radius 50 m) with the target in the center. This need is dictated by the size of the covariance and its growth during the simulation time, and no orbit should be so close to the KOZ.

Figure 6.1 shows all the feasible and unfeasible combinations of α and β with a defined ρ. As expected, some combinations of inclined orbits cannot be applied, because they do not satisfy the constraint. Especially, for ρ equal to 65 m (initial parameter assumed also in the previous strategies) not so many combinations can be adopted. Also for this reason, the choice to consider others ρ is relevant. In fact, when the latter coordinate increases, the number of combination improves, extending both ranges of α and β. Anyway, for the upper limit assumed for ρ, the central region of all graphs remains unfeasible, and the only way to fill it (so, to make valid also those combinations) is to get a ρ larger than

200 m. This is connected to the effect of the β: since this value will be equal to 90°, the relative orbit will be characterized by a major and minor axis that are the half of their respective in the case of $\beta = 0$.

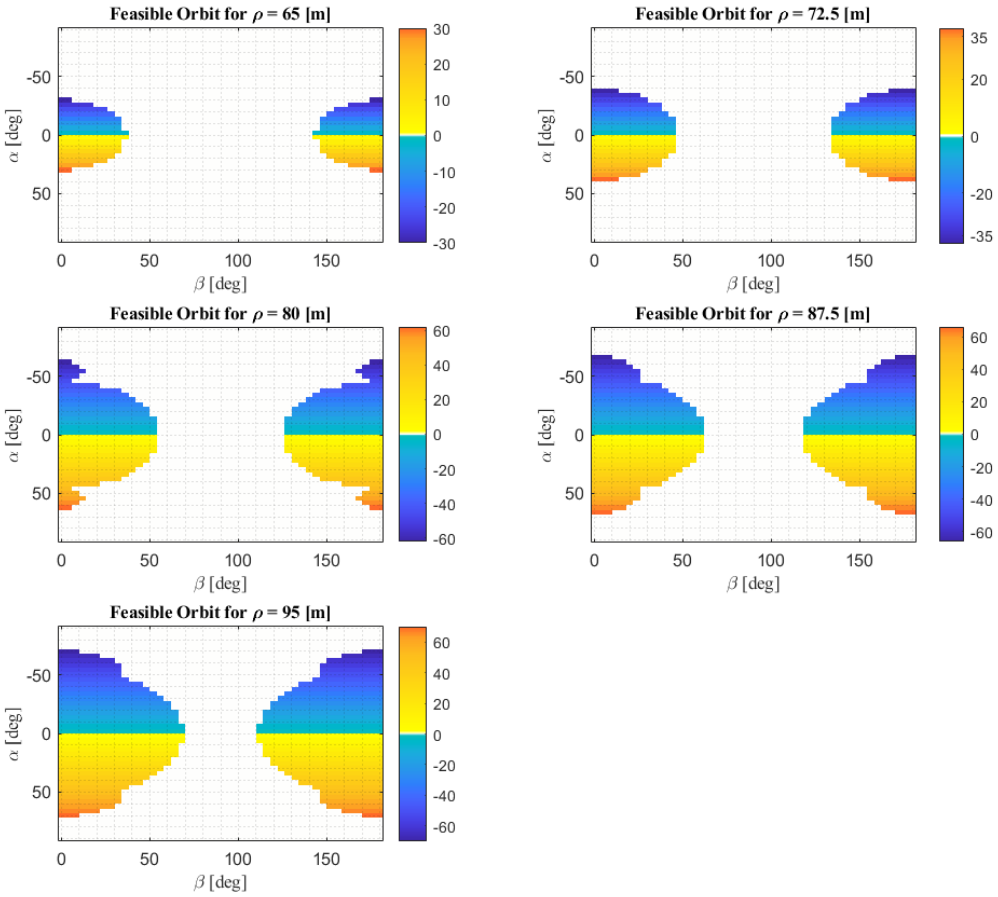

Figure 6.1: Orbit size analysis

From these results, the last detail to define before running the simulation is related to the choice of the orbit in the simulation itself.

6.1.2 Selection of the inclined orbit

Due to the fact that this strategy focuses on the inspection phase, this thesis proposes to change the three coordinates of the new kinematic model based on the quality of the inspection, specially related to the partition of the visibility on each target's face. Two parameters have been identified for this scope:

- Percentage of inspection time spent to inspect only a face during the phase (also called $f_{\%,1}$);
- Percentage's ratio between the most visible face and the least corresponding one (also called f_{ratio});

The first parameter could be affected by the distance. Due to the absence of the knowledge of the target's attitude, only ρ has been considered to correct this issue, and based on the amplitude of the percentage, ρ can be varied also for some meters, in order to improve the FoV of the camera and allow the visibility of the target.

The second parameter is connected more to the angles. Always based on the level of the percentage, a combination of α and β can be applied to try remedy some shortcomings given by the last inspection phases. In this thesis, if the selection of possible variations of α and β for each cycle has been defined arbitrary and some values have been assumed, on the other hand these assumed values must be compared to the boundary constraints due to the necessity of the inclined orbit to stay at a certain distance from the KOZ. So, from Sect. 6.1.1, upper and lower bounds have been selected for each ρ layer. Briefly, the Fig. 6.2 resumes the methodology chosen and implemented in the algorithm. Starting from f_{ratio}, 2 proposals of values of α and β are generated. These are only additive terms, that will be added to the α_0 and β_0 already existing, generating α_f and β_f, respectively. Then, following the choice of ρ by the f_{ratio} (and the resulting selection of limits of α_c and β_c), the α_f and β_f shall satisfy the constraint. If not, the sign of the additive terms shall be switched.

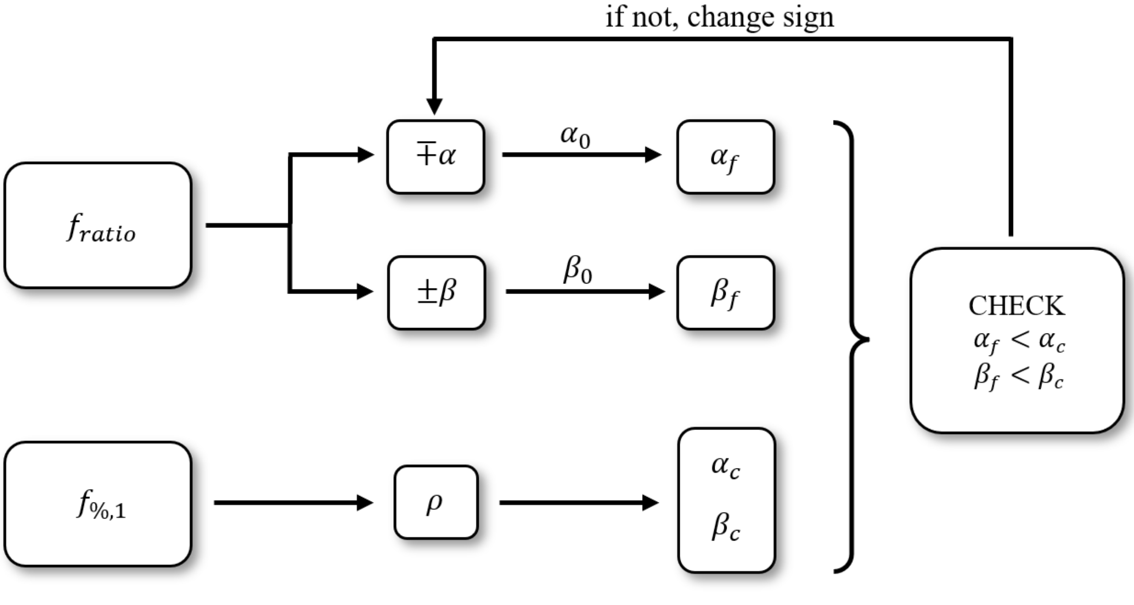

Figure 6.2: Algorithm scheme

After the selection of these parameters, the manoeuvre can be performed as described in Sect. 5.1.8, but instead of reaching the initial nominal orbit again, a change of this will be done. Following this explanation, some arbitrary values and limits have been assumed, in according to the experience and the previous analysis in Sect. 6.1.1, and listed in Tab. 6.1.

$f_{\%,1}$ boundaries	
$f_{\%,1}$	ρ [m]
> 45	+ 5
25 - 45	+ 3
15 - 25	+ 0
< 15	ρ - 3

(a) Percentage limits of $f_{\%,1}$ condition

$f_{\%,1}$ boundaries		
ρ [m]	α [deg]	β [deg]
< 70	27	30
70 - 75	33	35
75 - 80	39	42
80 - 85	43	48
85 - 90	50	55
90 - 95	55	60

(b) α & β limits as function of ρ

f_{ratio} boundaries [%]		
f_{ratio}	α [deg]	β [deg]
< 10	∓ 13	± 9
10 - 30	∓ 8	± 7
30 - 60	∓ 6	± 4
> 60	∓ 0	± 2

(c) Percentage limits of f_{ratio} condition

Table 6.1: Conditions of selection of inclined football orbit

In general, there are other two conditions to highlight:

- after a manoeuvre where α and β change, the deputy shall stay on the new inclined orbit at least for two cycle. It means that the next burn has the purpose to bring again the satellite in the same nominal orbit;
- after three manoeuvres where the magnitude of α and β increase, a change of sign is imposed for the next three manoeuvres. This is useful to avoid exceeding the boundary constraints of angles and to reduce ρ;

Obviously, the increasing or decreasing of ρ leads to increasing or decreasing of Δv, respectively.
Following, this part will be inserted into the autonomous algorithm to be tested in an unperturbed environment. Unlike the Sect. 5.1.11, the part related to the stopping zones, described in Sect. 5.31, has been neglected, maintaining the other conditions for the inspection phase.

6.1.3 Results

Fixed configuration

The algorithm has been tested only in unperturbed case. First of all, considering Tabs. 4.4 and 4.2, the results are defined for target's fixed configuration. Now follow a possible solution of this new update of algorithm.
The behaviour of the covariance is affected by the inspection phase conditions imposed in Sect. 5.1.10 and, as expected, it has a good trend. As it can be noticed just seeing, the green zones incremented their length. The same can be said for the error, that respect the covariance boundaries in the most of the simulation time. In the Fig. 6.3, the comparison between the real trajectory and the path seen by the deputy is present, providing that, from the initial relative orbit, the satellite achieves points outside the classical nominal orbit, adopting inclined orbit generated by the combination of $f_{\%,1}$ and f_{ratio}.

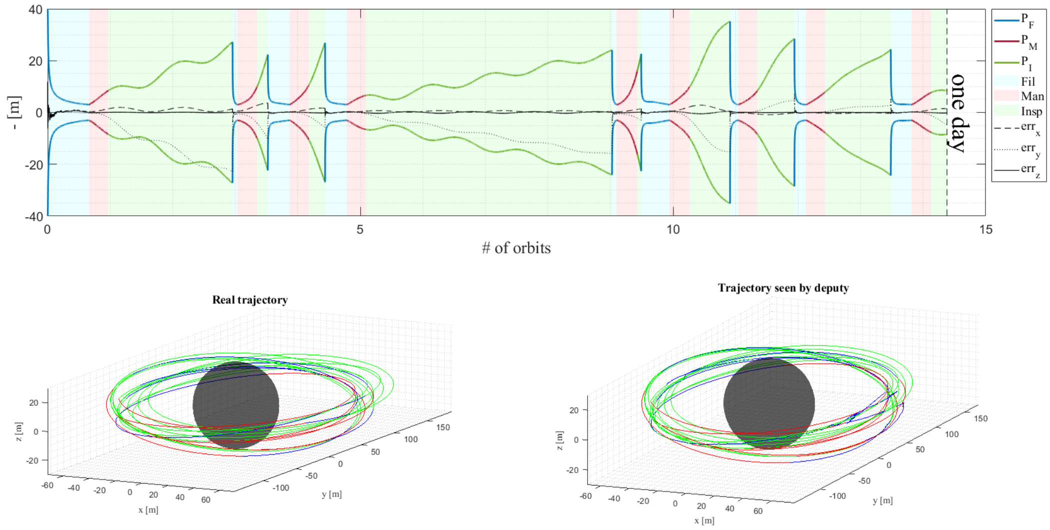

Figure 6.3: NP - Strategy E1: behaviour of the covariance and orbit representation

The Δv for each manoeuvre remains in the limits imposed, despite the changes of plane. This can be motivated by the choice to adopt relative orbits not too much distant between them. In respect of the single orbit, z-component increases its importance, due to the variation of α.

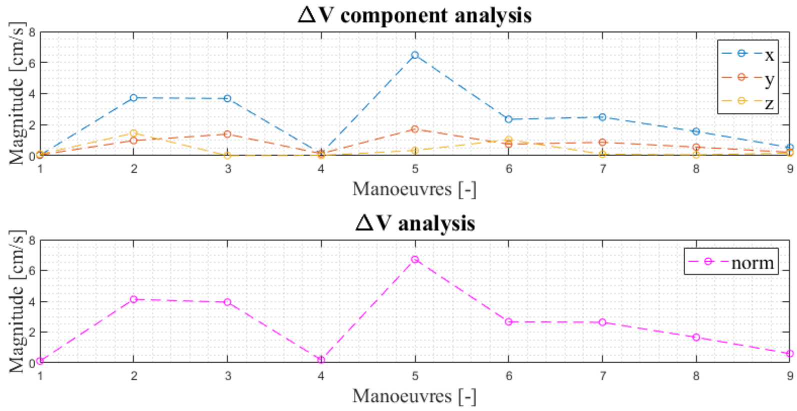

Figure 6.4: NP - Strategy E1: behaviour of the Δv

As expected, the inspection phase obtains more importance than the single orbit cases, gaining 11% from good covariance strategies at least and some percentage from Sect. 5.1.12.

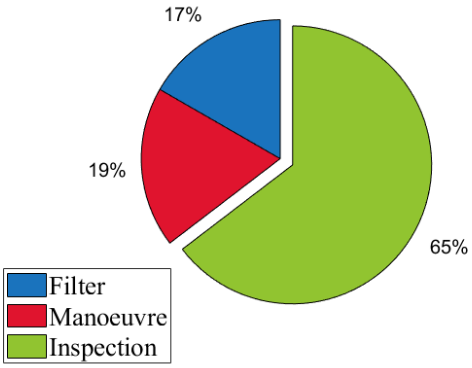

Figure 6.5: NP - Strategy E1: percentage of the phases

Instead, the result of the quality of inspection, in Figs. 6.6 and 6.7 is less expected, and from a certain point of view, the values can improve adjusting the values assumed in Tabs. 6.1. In particular, some of the visibility of the faces is affected by the initial condition of the fixed target imposed. This can be seen from the very different values of visibility time for the faces 3 and 6 with respect to the others. Concerning the previous strategies, the improvement is not quite evident, as also them are affected by how the target is positioned, leading to the increment of the visibility time for some specific faces.

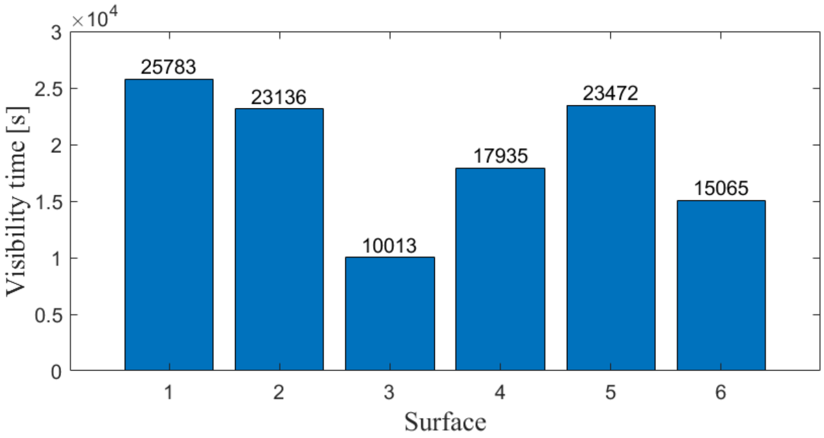

Figure 6.6: NP - Strategy E1: visibility of each of the faces

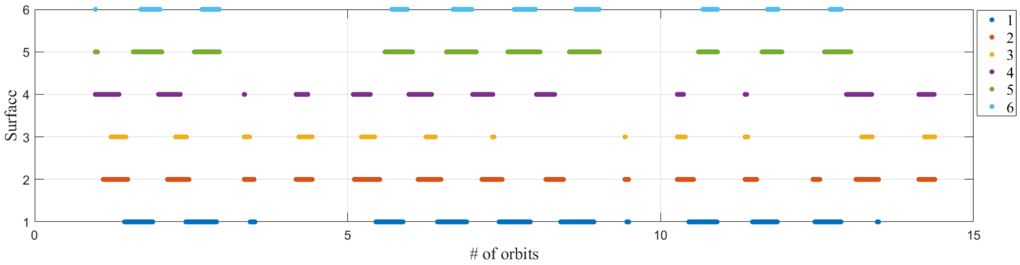

Figure 6.7: NP - Strategy E1: visibility in time of each of the faces

Tumbling configuration

In this study case, the algorithm has been tested adopting also the tumbling conditions, contained in Tabs. 4.4 and 4.3. One of the solution will be shown below.
The trend of behaviour is quite similar to the previous strategy in the Fig. 6.3, and the error satisfies their constraints. Moreover, in this strategy, the inclination of the relative orbit do not increase too much, due to the target's attitude that allows to see all the faces independently from the point of the orbit. So, for this reason, the inspection coefficients described before give values that do not force the satellite to increase inclination.

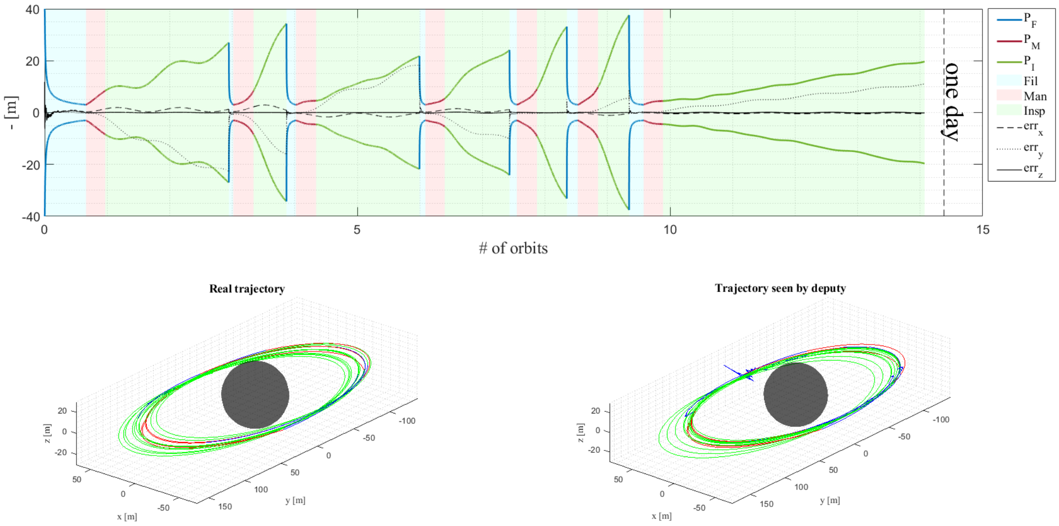

Figure 6.8: NP - Strategy E2: behaviour of the covariance and orbit representation

Also the Fig. 6.9 shows that the magnitude of the burns is good and satisfies the boundary constraints. Unlike Fig. 6.4, Δv is smaller, due to the fact that this strategy does not need to increase too much the inclination.

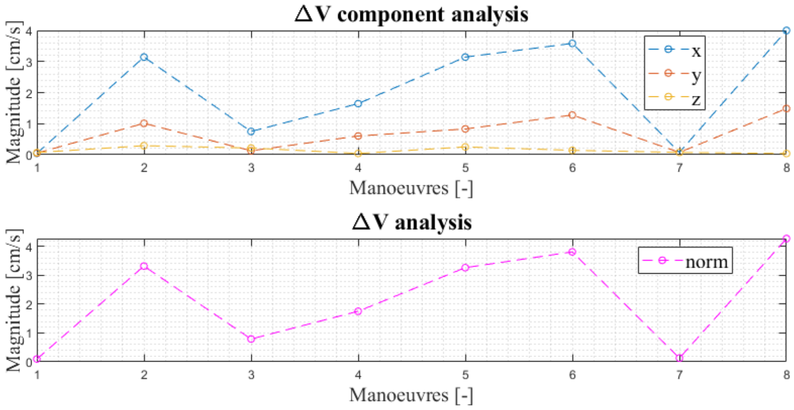

Figure 6.9: NP - Strategy E2: behaviour of the Δv

The inspection time, as shown in the Fig. 6.10, increase, obtaining more 10% of time with respect to the Fig. 6.5 and more 20% to the others strategies.

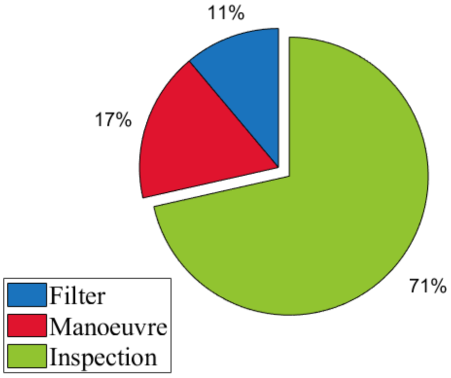

Figure 6.10: NP - Strategy E2: percentage of the phases

The Figs. 6.11 and 6.12 shows the inspection performances in the entire simulation time. At increasing of inspection time corresponds a major number of visibility for each faces, but on the other hand, the proportion between the most face seen and the least one changes based on the algorithm solution. In this case, the results are aligned with the previous strategies described in Sect. 5.1.14. Maybe, as already mentioned, the choice of Tabs. 6.1 is fundamental and deserve a further analysis.

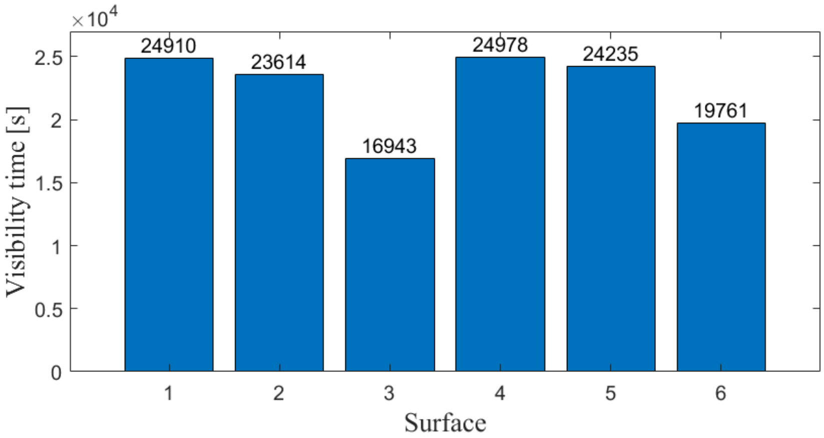

Figure 6.11: NP - Strategy E2: visibility of each of the faces

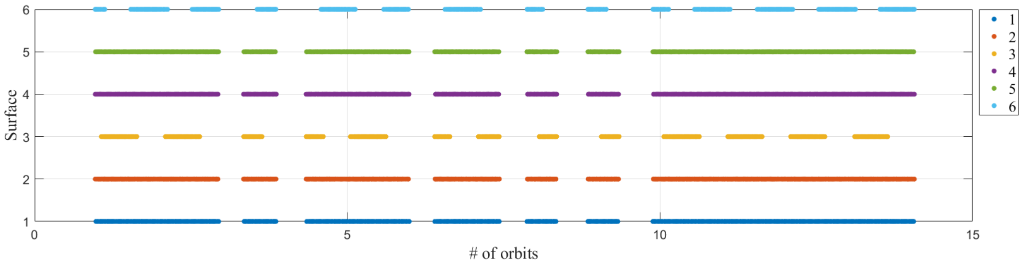

Figure 6.12: NP - Strategy E2: visibility in time of each of the faces

Chapter 7

Validation on Raspberry Pi

This chapter is dedicated to the analysis of the capabilities and limitations of the application of the algorithm in a real world scenarios. Especially, this part has the aim to describe the behaviour of the algorithm with a processor in the loop analysis, that provides an estimation of the expected computational time per filter iteration obtained with a limited resources system such as a Raspberry Pi 4 Single Board Computer (SBC). The analysis can be considered equal for both the unperturbed and perturbed case because the on-board dynamics does not change and the external dynamical model propagation does not entry in this analysis, due to the fact that its unique purpose is to simulate the real environment.

7.1 Computational cost for each phase

The filter, the manoeuvre and the inspection phases are executed five times on a Raspberry Pi 4 platform, equipped with 4GB of RAM, 64GB MicroSD acting both as storage and OS drive. This SBC runs on a quad-core ARM Cortex-A72 processor at up to 1.5GHz. This latter feature, enables the optimization of the compilation of the entire algorithm code for faster execution, allowing a significant code speedup. The use of this SBC also allowed to perform a sensitivity analysis to observe the degradation of performance for lower clock speeds. In particular, it was possible to directly analyze the range of frequencies of 600 - 1500 MHz. It is important to mention that, as expected, the computational time of each mission iteration, composed of filter, manoeuvre and inspection, was mostly occupied by the filter, which accounts for more than 99% of the computational time. The results of this analysis are reported in the Figs. 7.1 and 7.2. Specifically, the manoeuvre phase has been divided in two parts: the first one (top right of Fig. 7.1) shows the time behaviour of the algorithm part where the manoeuvre is computed and it occupies the smallest amount of time during the mission simulation, while the second one (bottom left) points the computational time of the GUT during the manoeuvre phase (bottom right). This latter plot has the same order of the GUT computed during the inspection phase. Finally, the graphs about UKF (top left) and total time in Fig. 7.2 are quite similar, due to the amount of time spent by the filter, as already mentioned.

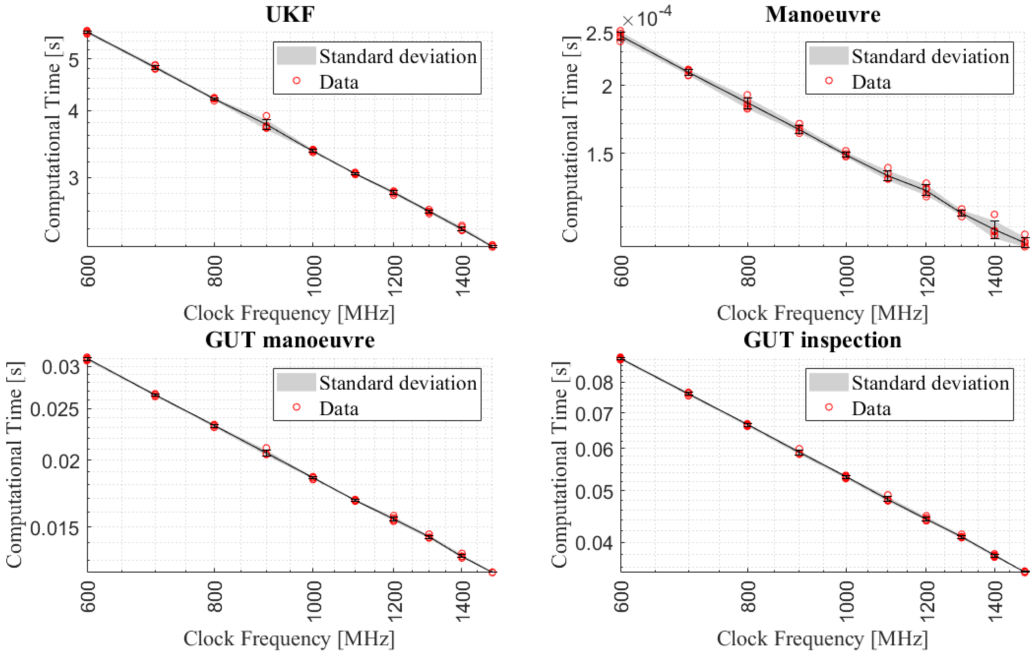

Figure 7.1: Computational time for each of the phases

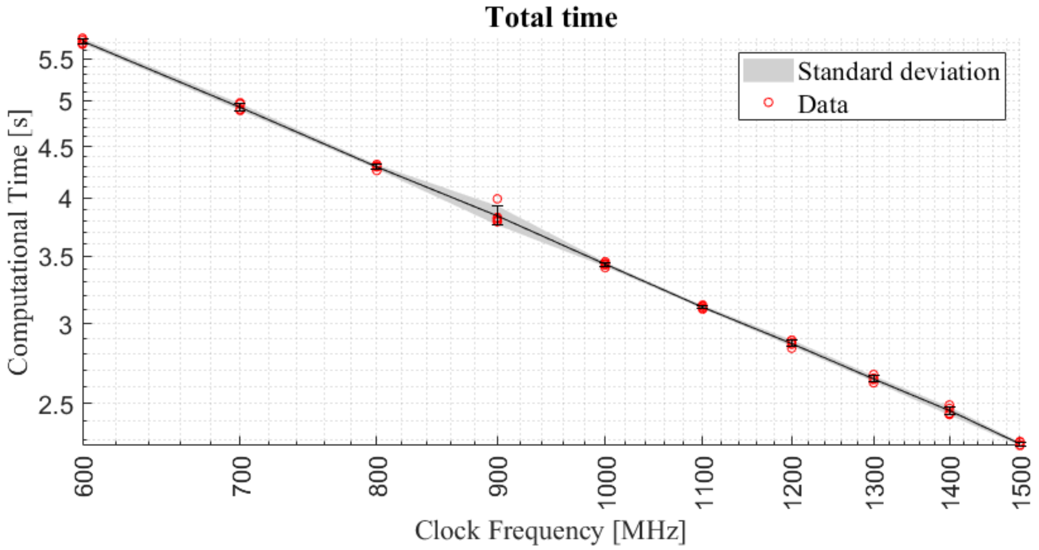

Figure 7.2: Total computational time

7.2 Computational cost for the UKF

For the filter phase, a further analysis has been done, and in particular considers the update and prediction steps. The data are split into percentiles of time spent on the 3970 iterations, that corresponds to the time assumed for the first cycle of the mission.
As the graph in Fig. 7.3 shows, the trend of the percentiles is not linear and there are some peaks at certain clock frequencies affected by a huge distribution of the data points. In fact, in these cases, the gaps between the percentiles tends to increase, while in the lower ones they maintain the same distances. Moreover, in the best case scenario of a

1.5 GHz clock speed, a measurement frequency of 857.63 Hz (that corresponds to take a measurement every 0.0012 seconds) would be enough to guarantee convergence of 90% of the iterations. On the other hand, if it is necessary to guarantee convergence in 100% of the iterations, this sampling frequency needs to be lowered to 551.57 Hz (a measurement every 0.0018 seconds). By adding the computational time for other on board applications, it is reasonable to assume a maximum measurement frequency of 0.0013 Hz (average value of overall available data set), that is 772 measurement every 1 seconds.

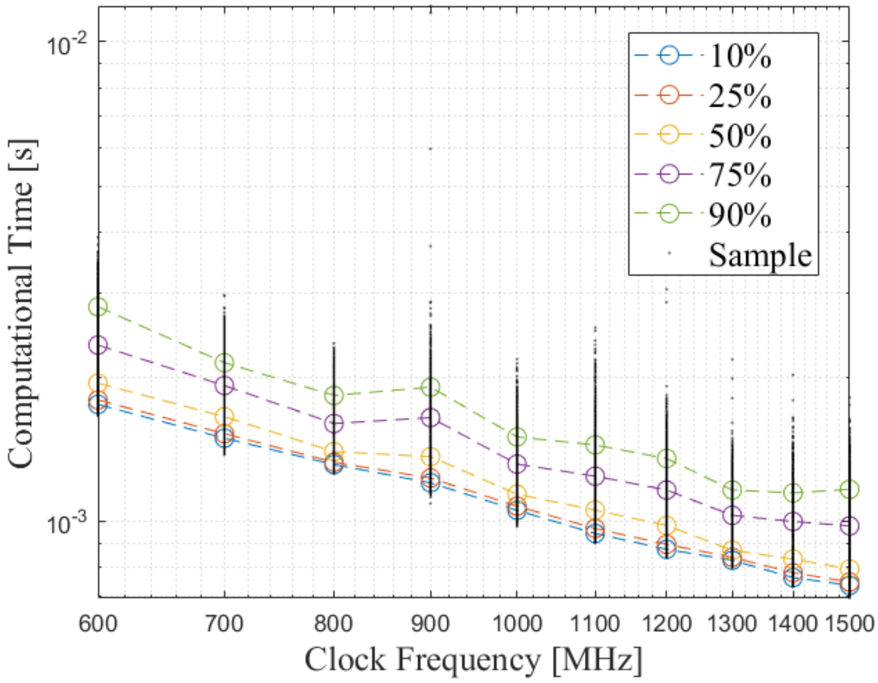

Figure 7.3: Computational time of the filter on 3970 iterations

Chapter 8

Conclusions

This treatment proposes different applications of a guidance and navigation systems algorithm to guarantee an efficient inspection mission. After the analysis of the proposed strategies, concerning both unperturbed and perturbed environments, but also both fixed and tumbling configurations, the results show the growth of the algorithm and how it reacts to external (simulation environment) and internal (both on-board computer and imposed conditions) solicitations. Summing up, the algorithm achieves a complete robustness and stability in the unperturbed case, and it can be expanded with further analyses to future works. On the contrary, in the perturbed case, the obtained results are not as robust. Specifically, in the most the strategies, the estimated states given by GUT do not follow the real trajectory, causing a divergence of the error, exceeding the limit of the covariance, which should contained it. Also, as it can be seen from strategy D2 in Sect. 5.2.12, the algorithm cannot perform as in the previous studied cases, leading to a complete lack of functionality. Instead, the proposal of adopting of inclined football orbit turned out to be an alternative solution to increment the quality of the inspection performances, although this approach is only an overview that could be deepened.

Nevertheless, this can be defined as a baseline of successive researches.
Surely, more improvements can be earned, considering the limitations of this thesis. First of all, together with the guidance and the navigation systems, the control systems of the deputy satellite can be implemented to enrich the ConOps. In fact, the previous strategies neglects the necessary time for the attitude control expected right before the manoeuvre phase, to direction the thrusters, and before the inspection phase, to align the camera towards the target.

Regarding the camera, a further modeling of the sensors can be developed, adding also other parameters as the resolution, also taking into account the existing technology. Moreover, considerations about the illumination conditions of the target and the background which affect the sensors should be examined to augment the reality of the simulation.

Looking to the future, which is going towards the miniaturization of the systems and the structure of the overall satellites, introducing CubeSats and Nanosatellites to perform the proximity operations, the propulsion system will become easier and less complex and will lose the capability to conduct impulsive burns, so it is relevant to study the behaviour of the continuous manoeuvres, as [21] presents.

According to the actual debris situation around the Earth, described also in the Sect. 1, this kind of mission performed in the LEO region may be applied also to an unknown and uncooperative RSO, introducing an other measurement model, which is able to reconstruct the shape of the target autonomously.

Another aspect to consider, in order to increase the degree of autonomy of the satellite, consists into connecting the inspection performances with the planning of the ConOps, acting on the manoeuvre and filter phases. This detail has been introduced in the chapter 6, trying to merge together the kinematic model and a few inspection parameters. Moreover, taking a cue from trajectory planning models as the model predictive control, another interesting prospective about the prediction of the future states of the deputy can be adopted.

Finally, as it can be noticed, the different behaviour of the unperturbed and perturbed models is represented by the HCW difficulty to emulate the perturbed NERM version. As countless graphs and the Sect. 2.5 show, another dynamical model can be used on the on-board computer, like the one presented in [2].

Bibliography

[1] *Assessment of Onboard DA State Estimation for Spacecraft Relative Navigation.* Project Summary, IPL-PTE/LF/as/517.2016. ESA, 2016.

[2] X. Cao B. Wu G. Xu. “Relative Dynamics and Control for Satellite Formation: Accommodating J2 Perturbation”. In: *Journal of Aerospace Engineering* 29, No. 4 (Jan. 2016). DOI: `10.1061/(ASCE)AS.1943-5525.0000600.`.

[3] C.A. McLaughlin C. Sabol R. Burns. “Satellite Formation Flying Design and Evolution”. In: *JOURNAL OF SPACECRAFT AND ROCKETS* 38, No. 2 (Mar. 2001). DOI: `https://arc.aiaa.org/doi/pdf/10.2514/2.3681`.

[4] W. H. Clohessy and R. S. Wiltshire. “Terminal Guidance System for Satellite Rendezvous”. In: *Journal of the Aerospace Sciences* 27, No. 9 (1960), pp. 653–658. DOI: `https://doi.org/10.2514/8.8704`.

[5] B. Dachwald. “Optimization of very-low-thrust trajectories using evolutionary neurocontrol”. In: *Acta Astronautica* 57 (2005), pp. 175–185. DOI: `10.1016/j.actaastro.2005.03.004`.

[6] J.C. Berges F. Capolupo T. Simeon. “Heuristic Guidance Techniques for the Exploration of Small Celestial Bodies”. In: *IFAC* 50, No. 1 (July 2017). DOI: `10.1016/j.ifacol.2017.08.1401`.

[7] P. Labourdette F. Capolupo. “Receding-Horizon Trajectory Planning Algorithm for Passively Safe On-Orbit Inspection Missions”. In: *JOURNAL OF GUIDANCE, CONTROL, AND DYNAMICS* 42, No. 5 (May 2019). DOI: `10.2514/1.G003736`.

[8] N. Faraco. “Instance segmentation for features recognition on non-cooperative resident space objects”. MA thesis. Politecnico di Milano, 2020. URL: `https://www.politesi.polimi.it/handle/10589/167418`.

[9] D. Wang G. Xu. “Nonlinear Dynamic Equations of Satellite Relative Motion around an Oblate Earth”. In: *JOURNAL OF GUIDANCE, CONTROL, AND DYNAMICS* 31, No. 5 (Sept. 2008). DOI: `https://arc.aiaa.org/doi/10.2514/1.33616`.

[10] E.G. Collins G.D. Francis. “Sampling-Based Trajectory Generation for Autonomous Spacecraft Rendezvous and Docking”. In: *AIAA GNC Conference* (Aug. 2013). DOI: `10.2514/6.2013-4549`.

[11] C.R. Gates. *A Simplified Model of Midcourse Maneuver Execution Errors.* Technical Report 32-504. Jet Propulsion Laboratory with California Institute of Technology, Oct. 1963. URL: `https://archive.org/details/N64_13278/page/n1/mode/2up`.

[12] J.S. Ginn. “Spacecraft Formation Flight: Analysis of the perturbed J2 - Modified Hill-Clohessy-Wiltshire Equations”. MA thesis. University of Texas, Mar. 2006. URL: `https://rc.library.uta.edu/uta-ir/handle/10106/354?show=full`.

[13] J. L. Junkins H. Schaub. *Analytical Mechanics of Space Systems.* 2nd edition. AIAA Education Series. American Institute of Aeronautics and Astronautics, 2009, pp. 673–679. URL: `https://arc.aiaa.org/doi/book/10.2514/4.867231`.

[14] D.J. Dana-Bashian H.B.Hablani M.L. Tapper. "Guidance and Relative Navigation for Autonomous Rendezvous in a Circular Orbit". In: *JOURNAL OF GUIDANCE, CONTROL, AND DYNAMICS* 25, No. 3 (May 2002). URL: `https://doi.org/10.2514/2.4916`.

[15] D.M. Henderson. *Euler Angles, Quaternions, and Transformation Matrices.* Technical Report. NASA, July 1977. URL: `https://ntrs.nasa.gov/citations/19770024290`.

[16] S.D'Amico J. Sullivan S. Grimberg. "Comprehensive Survey and Assessment of Spacecraft Relative Motion Dynamics Models". In: *JOURNAL OF GUIDANCE, CONTROL, AND DYNAMICS* 40, No. 8 (Aug. 2017), pp. 1837–1859. DOI: `10.2514/1.G002309`.

[17] G.D. Mahler J.A. Starek E. Schmerling. "Real-Time, Propellant-Optimized Spacecraft Motion Planning under Clohessy-Wiltshire-Hill Dynamics". In: *IEEE Aerospace Conference* (Mar. 2016). URL: `https://ieeexplore.ieee.org/document/7500704`.

[18] G.E. Chamitoff J.F. Shi S. Ulrich. "Trajectory Optimization for Proximity Operations Around Tumbling Geometrical Constraints via Legendre Polynomials". In: *AIAA SPACE Forum* (Sept. 2016). DOI: `10.2514/6.2016-5270`.

[19] J.A. Kechichian. "Motion in General Elliptic Orbit with Respect to a Dragging and Precessing Coordinate Frame". In: *Journal of the Astronautical Sciences* 46, No. 1 (Jan. 1998), pp. 25–45. URL: `https://link.springer.com/article/10.1007/BF03546191`.

[20] C. Novara M. Pagonea M. Boggio. "A Sparse Nonlinear Model Predictive Control for Autonomous Space Missions". In: *71st International Astronautical Congress* (Oct. 2020). URL: `https://iris.polito.it/retrieve/e384c432-ae33-d4b2-e053-9f05fe0a1d67/A%5C%20Sparse%5C%20Nonlinear%5C%%2020Model%5C%20Predictive%5C%20Control%5C%20for%5C%20Autonomous%5C%20Space%5C%20Missions.pdf`.

[21] M. Maestrini. "Satellite Inspection of Unknown Resident Space Objects". PhD thesis. Politecnico di Milano, Feb. 2022. URL: `https://www.politesi.polimi.it/handle/10589/183016`.

[22] C. Rouff. *Autonomy in Future Space Missions.* AAAI Technical Report WS-02-03. Mar. 2002. URL: `https://s3vi.ndc.nasa.gov/ssri-kb/static/resources/WS02-03-010.pdf`.

[23] P. Di Lizia S. Servadio F. Cavenago and M. Massari. "Nonlinear Prediction in Marker-Based Spacecraft Pose Estimation with Polynomial Transition Maps". In: *JOURNAL OF SPACECRAFT AND ROCKETS* 59, No. 2 (Mar. 2022). DOI: `https://doi.org/10.2514/1.A35068`.

[24] V.J. Modi S.R. Marandi. "A Preferred Coordinate System and the Associated Orientation Representation in Attitude Dynamics". In: *Acta Astronautica* 15, No. 11 (1987), pp. 833–843. DOI: `10.1016/0094-5765(87)90038-5`.

[25] T. P. Wahl. "Autonomous guidance strategy for spacecraft formations and reconfiguration maneuvers". PhD thesis. Feb. 2017. URL: `https://engineering.purdue.edu/people/kathleen.howell.1/Publications/Dissertations/2017_Wahl.pdf`.

[26] D. C. Woffinden. "On-Orbit Satellite Inspection: Navigation and ΔV Analysis". MA thesis. Massachusetts Institute of Technology, Sept. 2004. URL: `https://dspace.mit.edu/handle/1721.1/28862`.

[27] D. C. Woffinden. "Angles-Only Navigation for Autonomous Orbital Rendezvous". PhD thesis. Massachusetts Institute of Technology, Dec. 2008. DOI: `https://doi.org/10.26076/15dc-267c`.